

The background of the entire page is a microscopic view of a foam structure. It shows a complex network of interconnected, thin, brownish-gold lines forming a porous, cellular lattice. The lighting is dramatic, with a bright, circular highlight in the center, creating a sense of depth and highlighting the intricate geometry of the foam's walls.

**Foams for Enhanced Oil Recovery: Exergy Analysis
to Assess Feasibility and Surfactant Screening for
Practical Steam Foam Applications**

Alberto Casquera García

Foams for Enhanced Oil Recovery: Exergy Analysis to Assess Feasibility and Surfactant Screening for Practical Steam Foam Applications

By

Alberto Casquera García

in partial fulfilment of the requirements for the degree of

Master of Science
in Applied Earth Sciences

at the Delft University of Technology,
to be defended publicly on Friday November 30th, 2018 at 03:00 P.M.

| | | |
|-------------------|------------------------------------|----------------|
| Supervisor: | Prof. Dr. Rouhi Farajzadeh | TU Delft |
| | Dr. Sian Jones | TU Delft |
| | Prof. Dr. Hans Bruinning | TU Delft |
| Thesis committee: | Prof. Dr. Rouhi Farajzadeh (Chair) | TU Delft |
| | Prof. Dr. Hans Bruinning | TU Delft |
| | Prof. Dr. Denis Voskov | TU Delft |
| | Prof. Dr. Karl-Heinz Wolf | TU Delft |
| | Dr. Sian Jones | TU Delft |
| | Dr. Sebastien Vincent-Bonnieu | Shell/TU Delft |

An electronic version of this thesis is available at <http://repository.tudelft.nl/>.

Acknowledgements

I would first like to express my sincerest gratitude to my supervisor, Prof. Dr. Rouhi Farajzadeh, for making it possible to write this thesis. His guidance helped me throughout my research, manifesting in the completion of this thesis. I would also like to thank my supervisor, Dr. Sian Jones, not only for her friendship and daily support, but also for her insightful comments and guidance, which encouraged me to critically look at my research project from a scientific perspective.

Further, I would like to thank Prof. Dr. Hans Bruinning, for his great advice in key thermodynamic and petroleum engineering topics. Also, I would like to thank Michiel Slob for providing his technical expertise and help to carry out the different experiments. Finally, I would like to thank CONACYT and SENER in Mexico for sponsoring my studies and stay in the Netherlands for the last two years.

Table of Contents

| | | |
|-------|---|----|
| 1 | Introduction..... | 11 |
| 2 | Literature Review..... | 14 |
| 2.1 | Enhanced Oil Recovery..... | 14 |
| 2.2 | Foams in Enhanced Oil Recovery..... | 15 |
| 2.2.1 | Surfactants..... | 15 |
| 2.2.2 | Foams General Definition..... | 16 |
| 2.2.3 | Local Foam Film Stability..... | 17 |
| 2.2.4 | Factors Influencing Foam Stability..... | 18 |
| 2.2.5 | Foams in Porous Media..... | 18 |
| 2.2.6 | Steam Foams..... | 23 |
| 2.3 | Exergy Analysis..... | 25 |
| 3 | Surfactant Screening Methodology..... | 28 |
| 3.1 | Overview..... | 28 |
| 3.2 | Solubility..... | 29 |
| 3.3 | Thermal Stability..... | 31 |
| 3.3.1 | Thermal stability setup..... | 31 |
| 3.3.2 | Thermal stability experiments..... | 32 |
| 3.4 | Critical Micelle Concentration..... | 34 |
| 3.4.1 | Static Surface Tension..... | 34 |
| 3.4.2 | Dynamic Surface Tension..... | 35 |
| 3.4.3 | Determination of CMC..... | 35 |
| 3.5 | Foam Quality..... | 36 |
| 3.5.1 | Foamability Tests Setup..... | 36 |
| 3.5.2 | Correction of volumetric flow rate of injected gas..... | 37 |
| 3.5.3 | Core Samples..... | 38 |
| 3.5.4 | Surfactant solutions composition..... | 39 |
| 3.6 | Static and Dynamic Adsorption..... | 40 |
| 4 | Experimental Results and Analysis..... | 42 |

| | | |
|-------|---|----|
| 4.1 | Solubility | 42 |
| 4.1.1 | Enhancement of Surfactant B Solubility..... | 43 |
| 4.2 | Thermal Stability..... | 44 |
| 4.2.1 | Test Series Results | 45 |
| 4.2.2 | Analysis of Surfactant Thermal Stability..... | 51 |
| 4.3 | Foam Behaviour in Porous Media..... | 54 |
| 4.3.1 | Surfactant B: Foam Quality Scan | 54 |
| 4.3.2 | Surfactant C: Foam Quality Scan | 55 |
| 4.3.3 | Surfactant E and F: Foam Quality Scan..... | 55 |
| 4.3.4 | Comparison of surfactants at 60°C, 120°C & 180°C..... | 56 |
| 4.3.5 | Static Adsorption | 57 |
| 4.4 | Dynamic Adsorption | 58 |
| 4.5 | Critical Micelle Concentration | 59 |
| 5 | Exergy Analysis Methodology | 61 |
| 5.1 | Overview | 61 |
| 5.1.1 | Exergy of Gas Capture..... | 62 |
| 5.1.2 | Exergy of Compression and Recompression | 63 |
| 5.1.3 | Exergy of Separation..... | 68 |
| 5.1.4 | Exergy of Water Treatment and Injection | 68 |
| 5.1.5 | Exergy of Surfactant | 70 |
| 6 | Exergy Analysis Results | 73 |
| 6.1 | Oil Recovery Factor | 73 |
| 6.2 | Exergy Recovery Factor – Base Scenario | 75 |
| 6.3 | Sensitivity Analysis..... | 76 |
| 6.3.1 | Scenario 2 – No Separation of Produced Gases..... | 78 |
| 6.3.2 | Scenario 3– No Separation and no Recompression of Produced Gases | 80 |
| 6.3.3 | Scenario 4– No Recompression of Produced Gases | 83 |
| 6.3.4 | Scenario 5– Changing the Surfactant Concentration | 85 |
| 6.4 | Comparison of Performance Between N ₂ , CH ₄ , Flue gas and CO ₂ | 88 |
| 6.5 | CO ₂ Emissions to the Atmosphere | 89 |

| | | |
|-------|---|----|
| 7 | Conclusions and Recommendations | 92 |
| 7.1 | Surfactant Screening for Steam Foam Applications | 92 |
| 7.1.1 | Recommendations for Future Research – Surfactant Screening..... | 93 |
| 7.2 | Exergy Analysis of SAG and WAG..... | 94 |
| 7.2.1 | Recommendations for Future Research – Exergy Analysis | 95 |
| | References..... | 96 |

List of Figures

| | |
|--|----|
| Figure 1-1. World energy demand by fuel and scenario [2] | 12 |
| Figure 2-1. Basic monomer structure of a surfactant [10] | 15 |
| Figure 2-2. Representation of surfactant molecules adsorbed on the interface and aggregated as micelles. [10] | 16 |
| Figure 2-3. General 2-D foam system [13] | 16 |
| Figure 2-4. A) Normal Lamella. B) Stretched lamella and diffusion of surfactant monomers [14] | 17 |
| Figure 2-5. Foam in porous media. Grains are squared objects, lamellae dotted white and gas dark gray [18] | 19 |
| Figure 2-6. Snap-off mechanism. A) Gas penetrating a constriction and B) a bubble is formed [13] | 19 |
| Figure 2-7. Lamella division mechanism. A) Approaching a branch point. B) Separate gas bubbles being formed [13] | 20 |
| Figure 2-8. Leave-behind mechanism. A) gas flowing through adjacent constrictions and B) forming lamellae [13] | 20 |
| Figure 2-9. Foam apparent viscosity as a function of interstitial velocity at a fixed foam quality [22] | 22 |
| Figure 2-10. Foam apparent viscosity as a function of foam quality at a fixed interstitial velocity [22] | 23 |
| Figure 2-11. Water-steam enthalpy diagram. A) Water. B) Saturated water. C) Saturated steam. D) Superheated steam. [29] | 25 |
| Figure 3-1. Surfactant A, B, C, D E and F diluted at a concentration of 2% wt. of active matter | 30 |
| Figure 3-2. (A) Steel holder and 10 ml glass tube (B) Steel holders connected to central gas lines inside oven | 31 |
| Figure 3-3. Thermal stability setup diagram indicating grouping of the containers steel holders and location of the valves | 31 |
| Figure 3-4. Glove bag with Nitrogen or Helium atmosphere and vacuum pump | 32 |
| Figure 3-5. Close-up view of foaming (caused by dissolved oxygen) in a 10 ml glass tube after depressurization to atmospheric pressure | 33 |
| Figure 3-6. Kibron EZPi ^{plus} Tensiometer | 34 |

| | |
|--|----|
| Figure 3-7. Du Noiüy-Padday steps to measure surface tension [40]..... | 34 |
| Figure 3-8. (A) Steps to measure dynamic surface tension. B) Dynamic surface tension behavior for a surfactant at different concentrations (mM = millimolar).[40] [10]..... | 35 |
| Figure 3-9. Surface tension (γ) as a function of surfactant concentration (A) for pure surfactant (B) for surfactant containing impurities. [10] | 35 |
| Figure 3-10. Schematic diagram of the core flooding set up..... | 36 |
| Figure 3-11. Illustration of core flooding setup | 37 |
| Figure 3-12. Aluminum core holder inside oven, showing the connection to the inlet and outlet streams, and the locations of the two pressure taps | 37 |
| Figure 3-13. Bentheimer sandstone core. | 39 |
| Figure 3-14. Crushed reservoir rock and surfactant solution after being centrifuged | 40 |
| Figure 3-15. Normalized concentration vs. pore volumes produced of Surfactant and tracer. The dotted lines represent the breakthrough. The surfactat loss, in this case is equal to 0.9 PV [46]..... | 41 |
| Figure 4-1. Surfactants A, B, C, D and E at a concentration of 2wt% after 24 hours under static conditions..... | 42 |
| Figure 4-2. Linear Toluene Sulfonate with an alkyl chain of 18 carbons..... | 43 |
| Figure 4-3. Surfactant Bin demineralized before and after heated at 90°C for 24 hours | 44 |
| Figure 4-4. Aryl group generic formula, which are those compounds containing an aromatic ring | 44 |
| Figure 4-5. Surfactants A and B active matter remaining after 0, 1,2, 4 and 8 days at 250°C and 100 bar | 45 |
| Figure 4-6. Surfactants C and D active matter remaining after 1,2, 4 and 8 days at 250°C and 100 bar | 46 |
| Figure 4-7. Surfactants A and B active matter remaining after 0, 1,2, 4 and 8 days at 275°C and 100 bar | 47 |
| Figure 4-8. Surfactants C and D active remaining after 0, 1,2, 4 and 8 days at 275°C and 100 bar | 47 |
| Figure 4-9. Surfactant B and C active matter remaining after 0, 1,2, 4 ,8, 16 and 32 days at 250°C and 100 bar | 48 |
| Figure 4-10. Surfactant E and F active matter remaining after 0,1,2,4,8,16 and 32 days at 250°C and 100 bar..... | 49 |

| | |
|--|----|
| Figure 4-11. Surfactant B with and without oxygen scavenger, active matter remaining after 32 days at 275°C and 100 bar | 49 |
| Figure 4-12. 32-day sample tubes, of Surfactant B and Surfactant B+OS, inside metal containers showing a white deposit | 50 |
| Figure 4-13. Thermal Stability of Surfactant A at 100 bar | 51 |
| Figure 4-14. Surfactant B, thermal stability at 100 bar..... | 52 |
| Figure 4-15. A) Surfactant C and B) Surfactant D thermal stability at 100 bar | 53 |
| Figure 4-16. A) Surfactant E and B) Surfactant F thermal stability at 100 bar | 53 |
| Figure 4-17. A) Apparent viscosity and B) MRF vs. foam quality at 60°C, 120°C and 180°C for Surfactant B..... | 55 |
| Figure 4-18. A) Apparent viscosity and B) MRF y vs. foam quality at 60°C, 120°C and 180°C for Surfactant C..... | 55 |
| Figure 4-19. A) Apparent viscosity and B) MRF vs. foam quality at 60°C, 120°C and 180°C for Surfactant E..... | 56 |
| Figure 4-20. A) Apparent viscosity and B) MRF vs. foam quality at 60°C, 120°C and 180°C for Surfactant F | 56 |
| Figure 4-21. Apparent viscosity and MRF of surfactants at 60°C..... | 57 |
| Figure 4-22.Apparent viscosity and MRF of surfactants at 120°C..... | 57 |
| Figure 4-23. Apparent viscosity and MRF of surfactants at 180°C..... | 57 |
| Figure 4-24. Surfactant adsorbed on core crushed stone with respect to temperature | 58 |
| Figure 4-25. Dynamic adsorption of surfactant B in Bentheimer sandstone core at 120°C | 58 |
| Figure 4-26. Surfactant A surface tension variation with concentration at 23°C | 59 |
| Figure 4-27. Surfactant B surface tension variation with concentration at 23°C | 59 |
| Figure 4-28. Dynamic surface tension (Wilhelmy method) for Surfactant B A) at 5 ppm tending to a constant value (squared) and B) at 1 ppm not tending to a constant value after 155 min. The transition to the linear decrease and recorded surface tension is indicated. | 60 |
| Figure 5-1. Schematic Diagram of gas and water injection system for WAG and SAG..... | 61 |
| Figure 5-2. First step of compression - CO ₂ and flue gas transport through a pipeline. P=pressure, T=temperature, S= entropy, H= enthalpy | 65 |
| Figure 5-3. Thermodynamic phase diagram of CO ₂ | 65 |
| Figure 5-4. Second step of compression – Injection into the reservoir | 66 |
| Figure 5-5. Recompression of gases to be reinjected into the reservoir | 67 |
| Figure 5-6. Gravity fluid separator [68]..... | 68 |

| | |
|---|----|
| Figure 5-7. Schematic diagram of water treatment and injection facilities | 69 |
| Figure 5-8. 2D reservoir model representation. | 71 |
| Figure 6-1. ExRF of SAG and WAG for all gases | 76 |
| Figure 6-2. Exergy invested and gained for WAG – Base Scenario | 77 |
| Figure 6-3. WAG energy invested | 77 |
| Figure 6-4. Scenario 2 - WAG and SAG ExRF without separation of produced gases | 79 |
| Figure 6-5. Exergy invested and gained for WAG – Scenario 2 | 79 |
| Figure 6-6. WAG energy invested – Scenario 2 | 80 |
| Figure 6-7. Scenario 3- WAG and SAG ExRF without separation and recirculation of produced gases..... | 81 |
| Figure 6-8. Exergy invested and gained for WAG – Scenario 3 | 82 |
| Figure 6-9. WAG energy invested – Scenario 3 | 82 |
| Figure 6-10. Scenario 4- WAG and SAG ExRF without separation and recirculation of produced gases..... | 84 |
| Figure 6-11. Exergy invested and gained for WAG – Scenario 4 | 84 |
| Figure 6-12. Share of energy invested for WAG – Scenario 4..... | 85 |
| Figure 6-13. Exergy invested and gained for SAG – All scenarios..... | 86 |
| Figure 6-14. Share of energy invested for SAG – Scenario 1 | 87 |
| Figure 6-15. Scenario 5- SAG ExRF at surfactant concentration of 0.5%, 2% and 5%..... | 88 |
| Figure 6-16. Best scenario for WAG, according to the highest ExRF | 88 |
| Figure 6-17. Best scenario for SAG, according to the highest ExRF | 89 |
| Figure 6-18. Cumulative CO ₂ emissions of WAG and SAG..... | 90 |
| Figure 6-19. CO ₂ emissions per barrel of incremental oil [kgCO ₂ /bbl] | 91 |

List of Tables

| | |
|---|----|
| | |
| Table 3-1. Anionic surfactants used for experiments. | 28 |
| Table 3-2. 5-Salt brine composition..... | 30 |
| Table 3-3. Summary table of conditions of thermal stability tests at 100 bar | 33 |
| Table 3-4. Bentheimer sandstone core characteristics. | 39 |
| Table 3-5. Surfactant solution compositions for core flooding | 40 |
| Table 4-1. Krafft point for Octyl- and Dodecyl-benzene sulfonates, for their sodium salts ... | 43 |
| Table 4-2. Dissociation Energy of non-metal and carbon (ethyl and aryl group) bonds at 25°C. | 52 |
| Table 4-3. CMC of Surfactants A and B by Du Noüy-Padday and Wilhelmy methods | 60 |
| Table 5-1. Exergy values for gas capture..... | 63 |
| Table 5-2. Exergy values for gas compression. First stage..... | 66 |
| Table 5-3. Exergy values for compression. Second stage | 67 |
| Table 5-4. Exergy values for gas recompression | 67 |
| Table 5-5. Exergy values for injected gas – CH ₄ separation..... | 68 |
| Table 5-6. Exergy of water injection | 70 |
| Table 5-7. Three-phase relative permeability parameters to water, oil, and gas (no foam). ... | 71 |
| Table 6-1. Oil Recovery with WAG and SAG for all gases | 73 |

Abstract

As the world population is projected to keep growing over the next decades, an increase in energy is required and hydrocarbon fuels will remain as the primary source of energy. Since most of the hydrocarbon resources have been discovered, it is necessary to extend the use of Enhanced Oil Recovery (EOR) methods on these mature fields to increase the fraction of oil recovered. Foam-EOR has shown to improve sweep efficiency during gas injection. However, there are two challenges regarding the use of foams: 1) the performance of the surfactants needed to generate foam and 2) the cost of these surfactants.

In this study the performance of six surfactants was tested for steam foam applications; focusing on solubility, thermal stability, foam stability and adsorption in porous media. The solubility of the surfactants ranged from good to poor. However, poor solubility can be enhanced by heating up the solution. The surfactants tested showed a large range of stability behavior, from very good to very poor. The surfactant with the best thermal stability at 275°C has a molecule with three characteristics related to high thermal stability: 1) Sulfonate head, 2) aromatic compound attached to the head, and 3) a long hydrophobic tail (above 18 carbon atoms). The other surfactants, with a low to very low thermal stability lacked one or more of these characteristics. The surfactant with the best thermal stability also had the best foam behavior in porous media at 180°C, showing a max. apparent viscosity of 0.42 Pa·s and a Mobility Reduction Factor of 2818. Finally, for this surfactant, the dynamic adsorption in Bentheimer sandstone was 0.059 mg/g_{rock} at 120°C.

Additionally, an exergy analysis was carried out to assess the cost of the surfactant from a thermodynamic point of view. For this purpose, the Exergy Recovery Factor was calculated for a system on which the Water Alternating Gas (WAG) and Surfactant Alternating Gas (SAG) EOR methods are applied, with different gases injected. The system includes from the initial capture of the gas and transport of the gas to the final oil and gas production from the reservoir and separation and recirculation of produced fluids. Despite the high exergy cost of the surfactant, the exergy recovery factor was higher for SAG than for WAG, meaning that more energy is extracted than invested. It was also found that less CO₂ was produced per barrel of incremental oil extracted with SAG than with WAG.

1 Introduction

1.1 A Global Energy Outlook and the Role of Hydrocarbon Fuels

According to the United Nations (UN), the world population is projected to keep growing over the next few decades. It is estimated that by 2050 the world population will be 10 billion; and by 2100, 11.2 billion [1]. In the worst case scenario, if the fertility rate declines slower than assumed, the population could increase to 16.5 billion by 2100. [1]. Because of this global population increase, a constant increase in energy is required. The International Energy Agency (IEA) estimates that by 2040 the total energy demand will be 30% higher than today [2].

The IEA considers 3 principal scenarios for future energy use: The ‘Current Policies Scenario’, the ‘New Policies Scenario’, and the ‘Sustainable Development Scenario’ [2]. The ‘Current Policies Scenario’ provides a point of comparison by considering only those policies and measures already ratified into legislation (middle of 2017). Meanwhile, ‘The New Policies Scenario’ is designed to show where current policies along with announced policies would lead the energy sector. In addition, the ‘Sustainable Development Scenario’ examines what would be necessary to achieve the main energy-related components of the “2030 Agenda for Sustainable Development” adopted in 2015 by member states of the United Nations. The three energy-related goals stated in “2030 Agenda for Sustainable Development” are: 1) to achieve universal energy access to modern energy by 2030; 2) to take urgent action to combat climate change; and 3) to drastically reduce the pollutant emissions that cause poor air quality.

It is expected that in the future China will remain as the world’s largest energy-consuming country. On the other hand, the largest energy consumers per capita will be in North America, zones of Eurasia, the developed nations of Asia, and the Middle East. Consumers in these areas are characterized by: 1) higher incomes and therefore, higher general consumption habits such as in Australia, Canada, Japan, South Korea, United States, etc., 2) high heating needs such as in countries with adverse cold temperatures like Russia and Canada, and 3) abundant fossil-

fuel resources and subsidies that promote an inefficient consumption and waste such as in the Middle East and Russia.

To cover this expansion in energy demand, the energy mix projected for the 3 scenarios by 2040 is shown in Figure 1-1. In the ‘New Policies Scenario’, the oil and gas share will be 53%. Even in the ‘Sustainable Development Scenario’, where the renewable energies share increases significantly, the oil and gas share is still 48%, representing a total of 6764 thousand Mtoe. So it seems that hydrocarbon fuels will remain as the primary source of energy for the coming years [2].

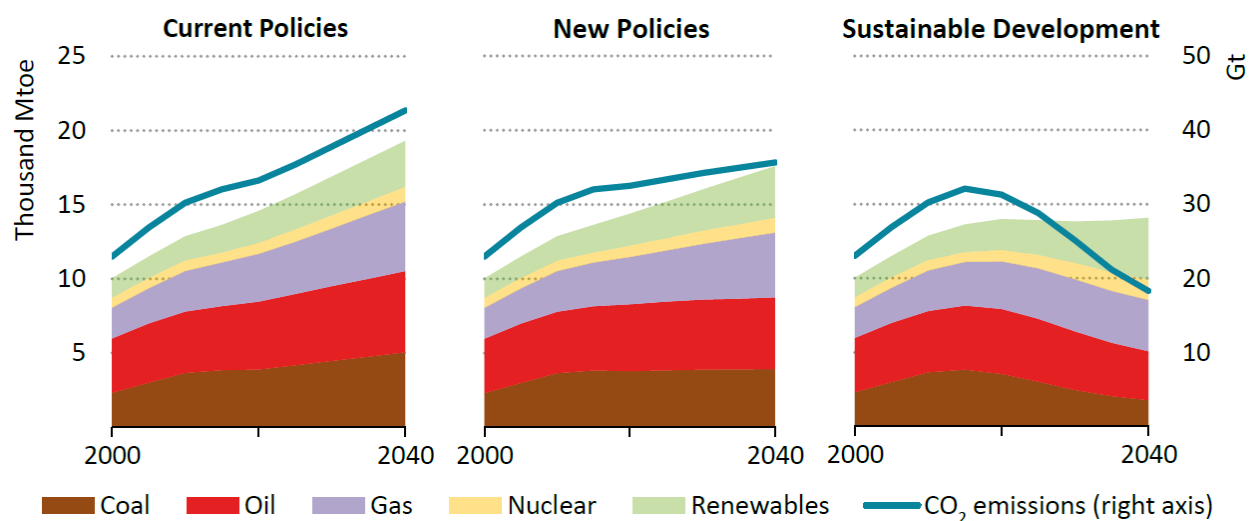


Figure 1-1. World energy demand by fuel and scenario [2]

1.2 Energy Supply and Enhanced Oil Recovery

How can the oil and gas industry fill this extra energy demand, but in a cleaner, more energy-efficient way? Since most of the oil and gas resources have already been discovered [3], it is necessary to extend the application of ‘Enhanced Oil Recovery’ (EOR) methods to maximize the production of mature fields. Among EOR methods, gas injection projects are steadily increasing [4]. Unfortunately, gas injection has some disadvantages that lead to a poor sweep efficiency.

Foam-EOR has been shown to improve gas injection sweep efficiency. However, there have been 2 main challenges regarding the use of foams: 1) the performance of the surfactants

needed to generate foam; specially at higher temperatures and salinities, and 2) the cost of these surfactants.

1.3 Thesis Outline

In this study, the performance of surfactants is evaluated at high pressure and high temperature for a real case injection scenario where steam foams are expected to be used. Also, an exergy analysis is done to assess the cost of Foam-EOR vs. other gas injection methods, from a thermodynamic point of view.

Key concepts about surfactants, foams, Foam-EOR, Steam Foam-EOR and Exergy, relevant for this study, are presented in Chapter 2. Chapter 3 contains the experimental methodology used to test surfactants for steam applications, including the experiments' setups, procedures, and materials. Chapter 4 presents and discusses the results of these experiments.

Chapter 5 describes the methodology used to carry out an exergy analysis, including values, formulas, models, and the software used. Chapter 6 shows the results of these calculations and discusses the sensitivity of key parameters. Finally, in Chapter 7 the conclusions of both the experimental and energy analysis are summarized and recommendations for further research are made.

2 Literature Review

2.1 Enhanced Oil Recovery

Enhanced Oil Recovery means oil recovery by the injection of materials that are not normally present in the reservoir [5]. During the producing life of a reservoir, there are 3 recovery stages: primary, secondary, and tertiary. Primary recovery is the stage in which hydrocarbon fluid is recovered by means of natural reservoir mechanisms. Such mechanisms can be liquid expansion, dissolved gas, gas cap, water influx and gravity drainage [5]. Secondary Recovery refers to the injection of water or hydrocarbon gas to increase or maintain the reservoir pressure and displace additional oil. After Secondary Recovery, most of the oil still remains in the reservoir around 60 to 70% [6]. Any technique applied to recover the oil left is known as Tertiary Recovery. Although EOR doesn't restrict to a stage, most EOR techniques target Tertiary Recovery.

EOR methods can be classified into thermal and non-thermal. The main mechanism of thermal methods is to raise the temperature of regions of the reservoir in order to heat crude oil and reduce its viscosity. Thermal methods include the injection of hot water or steam, or by conducting in situ combustion of hydrocarbons. Non-thermal methods are divided principally into Gas Flooding and Chemical Flooding. Other existing methods include microbial injection, hydrodynamic EOR [7], radial hydraulic jet drilling [8], etc.

The main mechanism of Gas Flooding is the mass transfer of components between the flowing gas and oil phase causing swelling and viscosity reduction. The mass transfer increases when the gas and oil become miscible as the pressure is increased. Injected gases can be light hydrocarbons, carbon dioxide (CO₂), nitrogen (N₂), and others. Gas injection can be implemented in a variety of ways such as continuous gas injection, continuous gas injection displaced by a chase phase, water-alternating-gas (WAG), tapered WAG, where the water/gas ration is increased or decreased continuously; and Simultaneous water-gas injection (SWAG) where water is injected into an upper zone, while gas is injected into a lower zone [9].

Finally, in Chemical Flooding, chemicals are injected with the water to improve the displacement efficiency in different ways. The main techniques of Chemical Flooding are

Polymer Flooding, Alkali Flooding and Surfactant Flooding. Polymer flooding increases the viscosity of the water injected decreasing the permeability to water and thus, increasing the sweep efficiency. Alkalis react with certain oil constituents and can lower the water-oil interfacial tension, emulsify oil and water and change rock wettability. Lastly, adding surfactants decreases the interfacial tension between oil and formation water, thereby lowering the capillary forces and facilitating oil mobilization.

2.2 Foams in Enhanced Oil Recovery

Thermal, gas, chemical, and other EOR methods can be combined to integrate the advantages of each. For instance, adding surfactants to gas injection or steam injection generates foam that reduces the shortcomings of these methods.

2.2.1 Surfactants

Surfactants are organic compounds with at least one hydrophilic non-polar group and one hydrophobic polar group in the same molecule as seen in Figure 2-1.

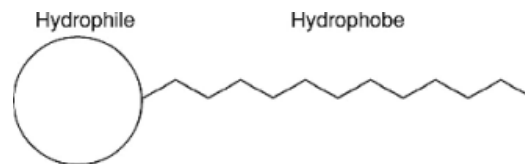


Figure 2-1. Basic monomer structure of a surfactant [10]

In aqueous media, surfactant molecules will migrate to, and will be adsorbed on, the interface (air-water, oil-water, or solid-water), positioned in such way to minimize the contact between their hydrophobic tail and the water [10]. Similarly, another way of limiting the contact between the hydrophobic tail and water is to aggregate in the bulk solution with the hydrophilic heads directed towards the aqueous phase. These aggregates are known as micelles and are shown in Figure 2-2. Micelles begin to form at the Critical Micelle Concentration (CMC), the concentration at which the interface is saturated with surfactant molecules. The CMC is influenced by temperature, pH and salt concentration.

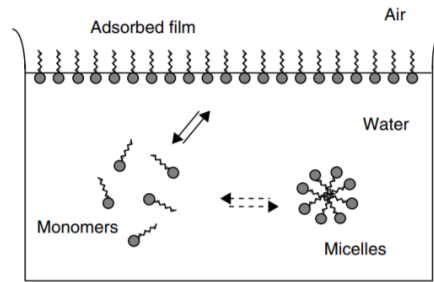


Figure 2-2. Representation of surfactant molecules adsorbed on the interface and aggregated as micelles. [10]

The hydrophilic head of a surfactant may carry a negative or positive charge, both positive and negative charges or no charge at all. These are classified as anionic, cationic, amphoteric (zwitterionic) or non-ionic surfactants respectively.

2.2.2 Foams General Definition

Foams are dispersions of a large volume of gas trapped in a small volume of liquid. The gas phase is separated by thin liquid-films called lamellae, as illustrated in Figure 2-3. The region enclosed by a dotted circle and connected by three lamellae is referred to as the Plateau border.

The average bubble size tends to increase with time as bubbles merge to form larger ones [11]. There are two mechanisms responsible for this, coarsening and coalescence. Coarsening is when gas diffuses from one gas bubble to another, driven by a difference in pressure. Coalescence is when the lamella separating two bubbles breaks. This breakage can be caused by the non-uniformity in the thickness of the lamellae [12] or by mechanical stress (e.g. rapid stretching), antifoams/defoamers, etc.

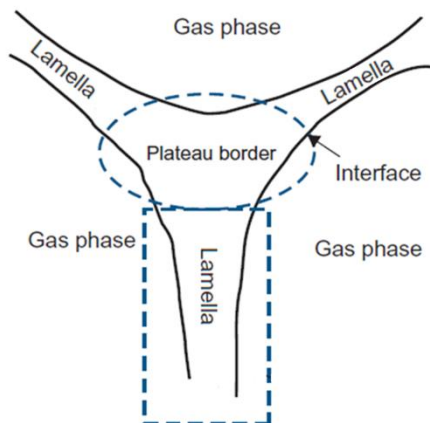


Figure 2-3. General 2-D foam system [13]

2.2.3 Local Foam Film Stability

In pure liquids, gas bubbles will rapidly coalesce. However, the presence of a foaming agent (surfactant) at the gas-liquid interface promotes thin-film stability and gives persistence to the foam structure. The mechanism of how a surfactant provides this stability is illustrated in Figure 2-4. When a liquid lamella is stretched, zones of high surface tension (γ) are created, then the surfactant diffuses from the bulk phase to the surface and then along the interface helping to stabilize the stretched lamella. This is known as the Gibbs-Marangoni effect. At very low bulk surfactant concentrations, or at very high bulk concentrations it is not effective [14].

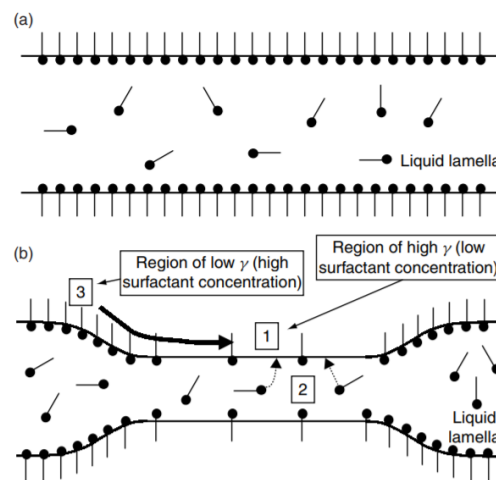


Figure 2-4. A) Normal Lamella. B) Stretched lamella and diffusion of surfactant monomers [14]

The surfaces of the lamellae interact, because of the surfactant molecules on them, and a disjoining pressure is exerted that acts to keep the two surfaces apart. The disjoining pressure is composed of the following three elements:

- **Electric double-layer repulsion.** - The interfaces are filled with ionic surfactant molecules which induce a repulsive force that opposes the thinning of the film.
- **Steric repulsion.** – Steric forces are the result from the repulsion between overlapping electron clouds. As the film begins to get thinner, steric repulsion of thin films becomes important. It is suggested to be the main stabilizing factor [13].
- **Dispersions forces (Van der Waals forces).** - These are attractive forces between the two lamella surfaces that result when temporary dipoles between atoms are formed. These attractive forces have a negative impact to the film stability.

2.2.4 Factors Influencing Foam Stability

A bulk foam exists when the size of the space in which the foam is contained is larger than the average size of the bubbles [15]. Therefore, the foam can be treated as a single-phase fluid [5]. According to thermodynamics, there are no infinitely stable foams; eventually they all collapse [5]. However, it is possible to influence the kinetics to delay collapsing.

The main mechanisms that affect bulk foam stability are:

- **Gravity drainage.** - Gravity will cause the liquid in the lamellae to drain downwards, causing the foam to dry out and thereby coalesce. Higher liquid viscosity will retard liquid drainage.
- **Capillary suction.** - There is a pressure difference between the Plateau borders and the lamellae. Because of this capillary pressure difference (i.e. the pressure difference resulting from the interaction of the fluid and the gas phase), liquid flows toward the Plateau borders causing thinning of the films.

Some other factors that also influence foam stability are:

- **Additional phases.** - Foam stability can be affected, both positively and negatively, by the presence of other phases such as oil or fine solids [16].
- **Bubble size.** - Foams that have a bubble size distribution that is weighted toward the smaller sizes will tend to show the most stable foam [16].
- **Temperature and pressure.** - When pressure is increased, the bubbles become smaller as the gas compresses. However, too high a pressure may break the bubble films [13]. Higher temperatures can also destabilize foams in 2 ways: by increasing the surfactant solubility in the liquid phase resulting in less surfactant in the gas-liquid interface and by speeding up liquid drainage [13].

2.2.5 Foams in Porous Media

In applications where foam enters porous media, the bubbles are generally the same size as, or larger than the individual pores [5] as shown in Figure 2-5. Therefore, generation mechanisms

are different, and stability is not necessarily influenced by the same mechanisms as bulk foams. In particular, the wettability of the rock has a significant impact, with foam generation and stability favored in water-wet rock rather than oil-wet rock [17].

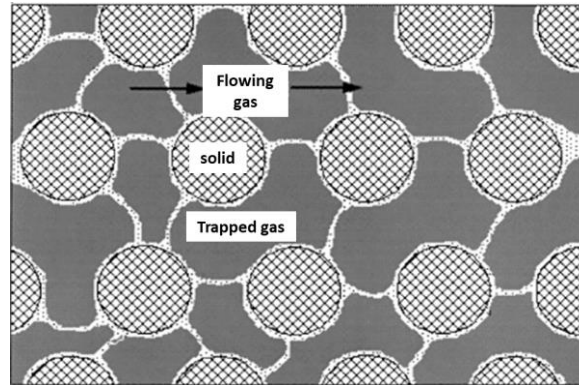


Figure 2-5. Foam in porous media. Grains are squared objects, lamellae dotted white and gas dark gray [18]

2.2.5.1 Foam Generation Mechanisms in Porous Media

There are three main foam generation mechanisms at the pore level:

1. **Snap-off.** – This occurs when gas penetrates a pore throat pushing the liquid, stretches and separates forming a new bubble as shown in Figure 2-6. It is believed to be the major foam-generation mechanism in rocks [19] [20].

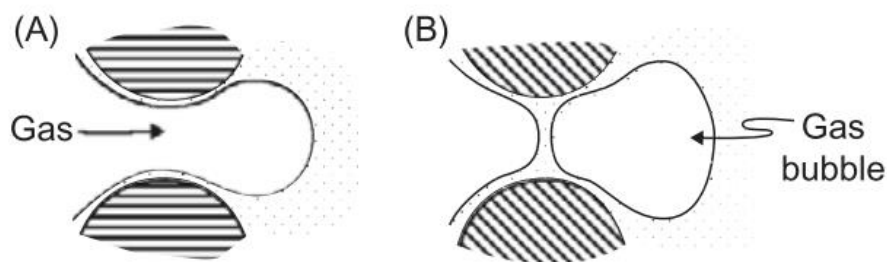


Figure 2-6. Snap-off mechanism. A) Gas penetrating a constriction and B) a bubble is formed [13]

2. **Lamella division.** – This occurs when a lamella approaches a branched point where the lamella is divided into two or more lamellae, forming new separated bubbles, as illustrated in Figure 2-7.

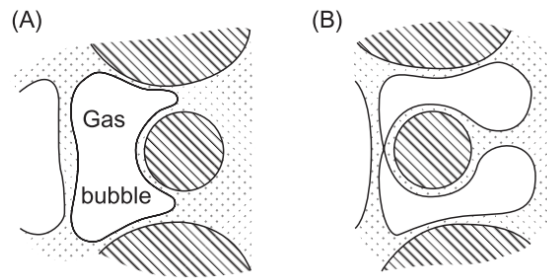


Figure 2-7. Lamella division mechanism. A) Approaching a branch point. B) Separate gas bubbles being formed [13]

3. **Leave-behind.** – This occurs when gas invades adjacent pore bodies, as seen in Figure 2-8, leaving behind a lamella between grains. This mechanism is more significant at low velocities and generates relatively weak foams.

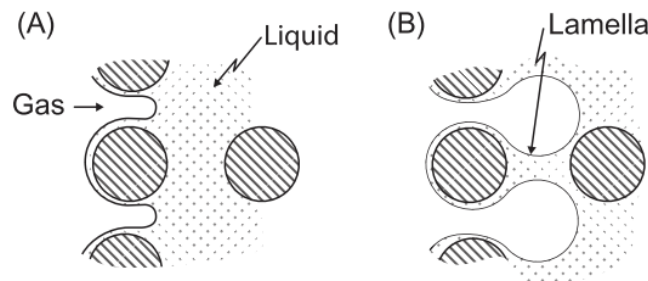


Figure 2-8. Leave-behind mechanism. A) gas flowing through adjacent constrictions and B) forming lamellae [13]

In porous media, capillary suction is the main mechanism that triggers coalescence [13]. The coalescence rate of lamellae in porous media depends on the capillary pressure. As the liquid fraction decreases, the capillary pressure increases until a critical capillary pressure is reached that lamellae cannot withstand, and coalescence occurs.

Coarsening rapidly removes bubbles smaller than a pore. However, for bubbles larger than a pore, coarsening stops once lamellae occupy pore throats. Consequently, coarsening is relatively unimportant in porous media [5]. Regarding the effect of wettability, foams were observed to be favored in water-wet porous media rather than oil-wet.

2.2.5.2 Performance of Foams in Porous Media

Foams have been shown to reduce gas relative permeability by blocking many of the flow pathways. Moreover, the drag forces exerted by the moving bubbles on pore walls increase the

gas apparent viscosity [21]. Therefore, a lower, more favorable mobility than pure gas injection is obtained. The mobility, λ , of any fluid is defined as [5]:

$$\lambda = \frac{kk_r}{\mu} \quad (1)$$

where:

$$\begin{aligned} k &= \text{Rock permeability} \\ k_r &= \text{Fluid relative permeability} \\ \mu &= \text{Viscosity of fluid} \end{aligned}$$

Therefore, the mobility ratio during gas injection is defined as [5]:

$$M = \frac{k_{rg}/\mu_g}{k_{ro}/\mu_o} = \frac{k_{rg}\mu_o}{k_{ro}\mu_g} \quad (2)$$

where:

$$\begin{aligned} k_{rg} &= \text{Gas relative permeability} \\ \mu_g &= \text{Gas viscosity} \\ k_{ro} &= \text{Oil relative permeability} \\ \mu_o &= \text{Oil viscosity} \end{aligned}$$

Having a lower gas mobility and thereby a lower mobility ratio, means that sweep efficiency is increased by reducing viscous fingering and fluid channeling.

Foaming performance is classically evaluated by measuring steady state pressure drop across a sand pack or core [22]. There are 2 parameters commonly used to represent the capacity of a foam to reduce gas mobility: foam apparent viscosity (μ_{app}) and mobility reduction factor (MRF) [22]. These are defined as follows [23]:

$$\mu_{app} = \Delta P_{foam\ flood} \frac{k}{(u_w + u_g)} \quad (3)$$

$$\text{MRF} = \frac{\Delta P_f}{Q_t} \bigg/ \frac{\Delta P_w}{Q_w} \equiv \frac{\mu_{app}}{\mu_{water}} \quad (\text{if } Q_f = Q_w) \quad (4)$$

where:

ΔP_f = Foam flood pressure gradient

ΔP_w = Water flood pressure gradient

u_w = Water velocity (Darcy)

u_g = Gas velocity (Darcy)

μ_{water} = water viscosity

Q_t = Total volumetric flow rate for foam (gas + water)

Q_w = Water volumetric flow rate

MRF and μ_{app} vary as a function of interstitial velocity (v_i), which is the fluid velocity in the pores, and foam quality (X_F), which is the fraction of gas relative to the total flow during foam flooding. These are defined as:

$$v_i = \frac{Q_t}{A\phi} \quad (5)$$

$$X_F = \frac{u_g}{u_g + u_w} \quad (6)$$

where:

A = Cross sectional area of sand pack or core

ϕ = Porosity sand pack or core

The behavior of apparent viscosity as a function of interstitial velocity, at fixed foam quality, is presented in Figure 2-9. A weak foam, that develops low to moderate apparent viscosities, shows Newtonian behavior. On the other hand, a strong foam develops higher apparent viscosities until a critical interstitial velocity (v_i^*) is reached. Above v_i^* , foam has shear thinning behavior.

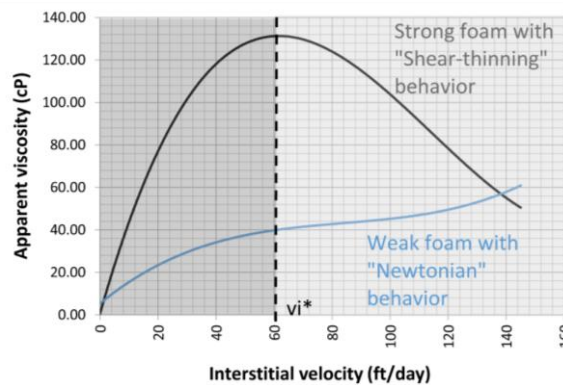


Figure 2-9. Foam apparent viscosity as a function of interstitial velocity at a fixed foam quality [22]

The behavior of apparent viscosity as a function of foam quality, at a fixed interstitial velocity is shown in Figure 2-10. Two regimes are described for a strong foam: low foam quality (wet) regime and high foam quality (dry) regime. In the low foam quality regime, the pressure gradient is independent of the liquid flow rate and the foam behavior is determined by bubble trapping and mobilization [24] and the foam is stable towards coalescence [22]. In the high foam quality regime, the steady-state pressure gradient is independent of the gas flow rate and the foam behavior is dominated by capillary pressure and coalescence [24].

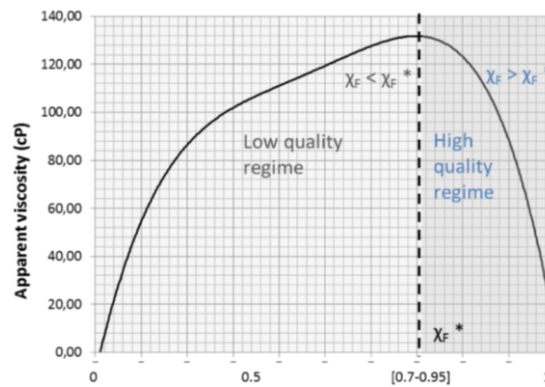


Figure 2-10. Foam apparent viscosity as a function of foam quality at a fixed interstitial velocity [22]

2.2.6 Steam Foams

Steam injection is a common EOR technique to recover heavy oil [25]. The principal effects of steam injection are thermal expansion of fluids and minerals, viscosity reduction and the distillation effect of steam under reservoir conditions [25]. Although it is a thermal method, there are two significant problems as in the other gas injection processes. First, gravity segregation or steam override makes the injected steam gradually rise to the top of the reservoir. Secondly, formation heterogeneities and the viscosity difference between steam and oil cause steam fingering. Both issues lead to an early breakthrough to production wells [26].

Steam foams reduces the mobility of steam and improves sweep efficiency as with the other gases. In laboratory studies, foams reduce steam mobility up to 40% in porous media [27]. In the field, numerous field trials attest to the efficiency of the process to improve steam conformance and increase oil production and recovery [22]. The first recorded field application of steam foam took place in 1973[22]. Since then, many field tests have been performed particularly in the USA. However, most of these tests took place between the 1980s and the

mid-1990s, but were stopped due to technical challenges and oil price fluctuations [22]. Nevertheless, due to technological improvements, especially with surfactants, steam foams have gained attention again.

To select a surfactant for any foam flooding process, it must comply with the following criteria:

- Good solubility,
- Low adsorption in porous media, and
- Good foaming properties in porous media; with or without oil.

For steam foam applications, these characteristics must persist at steam temperatures. However, thermal stability at high temperatures is the most important property that surfactants must possess. Above 200 °C, most anionic surfactants with an hydrophilic sulfonate group are stable in the following order: sulfonates < alpha olefin sulfonates < alkybenzene(toluene)sulfonates [13]. Commercially, mixtures of these main surfactants with other compounds have been made, to improve solubility and adsorption [22].

There are some particular considerations regarding the use of steam foams in the field; these are:

- **Surfactant concentration.** – There must be enough surfactant available to assure a strong foam, given that adsorption to the reservoir rock and thermal degradation will occur. In field tests, concentrations typically range between 0.5% wt. and 2% wt. [22].
- **Degradation of Surfactant.** – Although it is hoped that surfactants will be stable at high temperatures over time, eventually they will degrade. Producing high amounts of surfactants can cause water-oil separation issues due to the formation of emulsions, which would increase operation costs [22] [28].
-
- **Steam quality.** – This is the proportion of saturated steam in a saturated water-steam mixture as shown in Equation (7). There must be enough moisture in the mixture for the foam to form. A good knowledge of the thermodynamics of the system is essential, from the injection surface facilities to the producer well, to assure the mixture stay in a

two-phase region as shown in Figure 2-11. In field tests, the steam quality range between 50% - 80% [22].

$$X_s = \frac{q_s}{q_w + q_s} \quad (7)$$

Where:

q_s = steam flow rate
 q_w = water flow rate

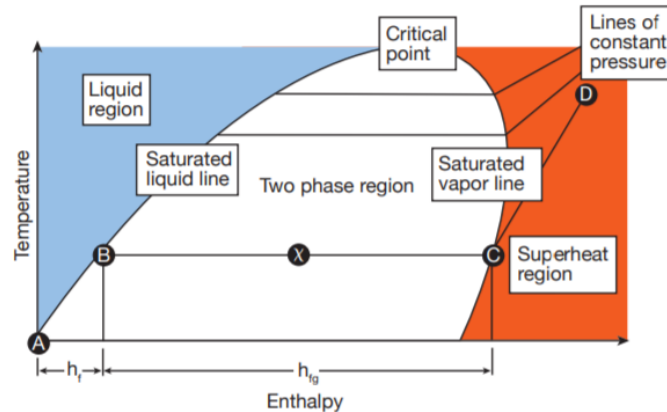


Figure 2-11. Water-steam enthalpy diagram. A) Water. B) Saturated water. C) Saturated steam. D) Superheated steam. [29]

- **Non-condensable gas.** – Condensation of the steam in the reservoir due to loss of energy with the surroundings is likely to happen causing collapse of the foam. Adding a non-condensable gas can help maintaining the foam structure, and in field tests, N₂ is the most used gas [27].
- **Surfactant slug design.** – Continuous injection has achieved the highest incremental recovery, but cyclic injection is more efficient in terms of incremental barrel of oil per kilogram of surfactant (bbl_{oil}/kg_{surfactant}) [22].

2.3 Exergy Analysis

Exergy can be defined as the quality of energy, useful energy, or available energy in any process. [30]. Therefore, an exergy analysis is an energy balance over a system with the aim to determine the locations, types, and magnitude of losses of energy. Moreover, from the outcome of the exergy analysis it is possible to find means to reduce such losses to make the energy system more efficient [31].

An exergy analysis is performed using classical thermodynamic principles and concepts such as heat (Q), work (W), Internal Energy (U), Enthalpy (H), Entropy (S), Gibb's free Energy (G),

efficiencies, etc. Exergy uses units of energy (SI for this study) and can be expressed as bulk exergy (Ex) [J], exergy power or exergy rate (\dot{Ex})[J/s] and specific exergy (\widehat{Ex}) [J/kg].

A system is defined an object or a collection of objects on which the exergy analysis is done [32]. The system has a definite boundary, called the system boundary, that is chosen and specified at the beginning of the analysis. Once a system is defined and delimited, everything external to it is called the surroundings. Thus, energy and mass that leave the system enter the surroundings and vice versa.

The state of a system is specified by a certain number of variables such temperature, pressure, mass, composition, velocity, and position. The state of a system can be changed; for instance, by increasing its temperature or varying its composition. Properties of the system, such as U, H, E and S, whose change depends only on the initial and final state are referred to as state properties or state functions. Exergy can only be measured by a change in one of the state functions. If the initial state of a system is not specified, it is assumed to be compared with a reference state, called the dead state, which will be assumed to be at $T_0=25^\circ\text{C}$ and $P_0=1\text{bar}$, $V_0=0\text{ m/s}$, $Z_0=0\text{ m}$

The total exergy of a material, Ex , can be defined as [33]:

$$Ex = Ex^{ch} + Ex^{ph} + Ex^{ke} + Ex^p \quad (8)$$

where:

- Ex^{ch} [J] is the chemical exergy, or internal exergy based on all molecular, atomic, and subatomic motions and interactions [34].
- Ex^{ph} [J] is the physical exergy or flow work based on temperature pressure and volume changes [34].
- $Ex^{ke} = \frac{mV^2}{2}$ [J] is the kinetic exergy associated with directed motion of a moving object of mass m and travelling with speed V .
- $Ex^p = mgZ$ [J] is the gravitational potential exergy of an object of mass m at an elevation Z in a gravitational field. Kinetic and potential exergies are assumed to be negligible compared to physical and chemical exergies.

The chemical exergy of a substance becomes relevant whenever energy is released in such way that it can be used directly or converted to other energy forms during a chemical exothermic reaction; like the combustion of fossil fuels where the hydrocarbon components are oxidized and converted to carbon dioxide and water.

The combustion exergy of fossil fuels can be estimated from the combustion exergy of each pseudo component (at dead state). The amount of energy released is dependent the hydrogen/carbon ratio; the more hydrogen/carbon ratio, the more energy released on combustion [35]. For fossil fuels, the chemical exergy can be defined as:

$$Ex_{oil}^{ch} = \sum_{i=1}^n x_i Ex_{psc}^{comb} \quad (9)$$

Where x_i and Ex_{psc}^{comb} are the mole fraction and the combustion exergy of the pseudo-component in the crude oil. For fossil fuels that have several individual components, it becomes difficult to estimate the exergy of combustion for each one, instead correlations can be used.

The physical exergy is the work required (or obtained) by taking a material stream through a reversible process from its initial state (T_0, P_0) to a final state (T, P) [32]. The specific physical exergy is expressed as [36]:

$$Ex^{ph} = H - H_0 - T_0(S - S_0) \quad (10)$$

Finally, the concept of Exergy Recovery Factor (ExRF) is introduced. It is relationship between the net available or useful exergy from a source and the original exergy contained in that source. A positive ExRF means that more exergy is available from a source than the input exergy required to extract that energy. A negative ExRF specifies that more input exergy is required than extracted.

The equation to calculate the ExRF is:

$$Ex_{RF} = \frac{\text{Exergy Gained} - \text{Exergy Invested}}{\text{Exergy Gained}} \quad (11)$$

Consequently, the Exergy Gained is chemical exergy of a substance and the Exergy Invested is the physical exergy required to extract that substance

3 Surfactant Screening Methodology

3.1 Overview

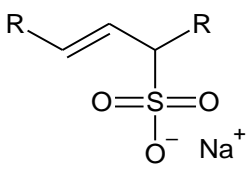
This work has been carried out to de-risk the steam-foam technology, the ultimate aim is to apply foams to fields currently flooded with steam to recover heavy oil.

For steam foam flooding applications, the desired characteristics required in a surfactant are high temperature stability, good foaming properties, good solubility in saline water and a low adsorption on reservoir rock [22]. Consequently, to select a suitable surfactant for steam-foam core flooding experiments, the following screening criteria were evaluated:

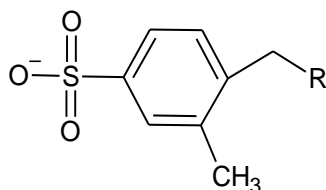
- i. Solubility
- ii. Thermal stability
- iii. Critical Micelle Concentration
- iv. Static and dynamic adsorption
- v. Foam quality scan (core flood)

Six anionic surfactants were tested, two surfactants from three companies. These surfactants represent a mixture of different constituents, rather than a single pure component. The main surfactant molecules are described in Table 3-1.

Table 3-1. Anionic surfactants used for experiments.

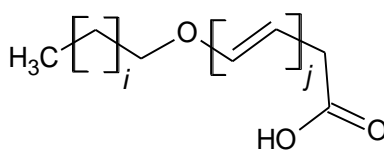
| Label | Classification | Typical structure | Comments |
|-------|---------------------------|---|--|
| A | Internal olefin sulfonate |  | This surfactant has a hydrophobic chain (R) of 20-24 carbons (from R to R), and offers a maximum application temperature of 200°C. It has a limited divalent ion tolerance. [37] |

B Linear alkyl
toluene sulfonate



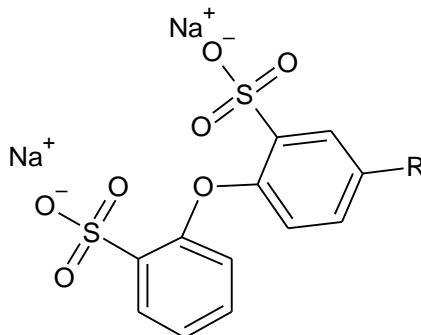
It has an hydrophobic chain (R) of 18-25 carbons, and offers a maximum application temperature of 250°C. It has a limited divalent ion tolerance. [37]

C, D alkyl ether
carboxylic acids



This surfactant molecule has “i” number of carbons and “j” number of ethylene units [38].

E, F Disodium
diphenyl oxide
disulfonate



This type of surfactant does not tend to precipitate in the presence of cations because of the disulfonate anion [16].

3.2 Solubility

Surfactants used in EOR processes are frequently exposed to saline environments specially sodium and calcium salts. This is either due to the formation water present in the reservoir, or because of the use of produced water and sea water to produce the surfactant solution to be injected. These surfactant solutions can experience a cation exchange with divalent ions leading to precipitation and therefore, a reduction in the surfactant concentration. The effect of a lower surfactant concentration is a slower and less efficient foam front from the injector to the production well.

To test the solubility, and for all the thermal stability experiments, the brine whose composition is shown in Table 3-2 was used. The field where the steam foam will be tested has been injected

for some years just with steam. Thus, this composition corresponds to the worst-case scenario brine that might be encountered in the field.

Table 3-2. 5-Salt brine composition

| Salt | Concentration (g/l) |
|--------------------------------------|---------------------|
| NaCl | 4.851 |
| CaCO ₃ | 0.000345 |
| MgCl ₂ .6H ₂ O | 0.293 |
| CaCl ₂ .2H ₂ O | 0.293 |
| Na ₂ SO ₄ | 0.518 |
| Total Dissolved Solids (TDS) | 5.9 |

Solutions of the surfactants shown in Figure 3-1 were prepared with a concentration of 2% wt. of surfactant active matter in the 5-salt brine. They were mixed for 20 minutes and degassed for at least another 30 minutes until no visible foam was generated by stirring. They were then left inactive for 24 hours at room temperature.



Figure 3-1. Surfactant A, B, C, D E and F diluted at a concentration of 2% wt. of active matter

To evaluate solubility qualitatively, the “Diagnostic Guide to Visual and Microscopic Observations of Surfactant Systems for interpreting visual observations of surfactant dispersions” [39] was applied. Using this guide, it is possible to get information about the size range of dispersed particles in surfactant solutions. This qualitative approach is based on principles of light scattering and spectroturbidimetry; and the perceptions of transparency and color.

3.3 Thermal Stability

The purpose of these tests was to determine the stability of the surfactant molecules at the temperatures that will be experienced in the injection wells (~250-270°C) and to evaluate the level of degradation of the active surfactant over time. The surfactant degradation mechanisms are complex; however, decomposition rate is influenced by temperature, at an exponential rate, and also, by a drop in pH. It is known that under the effect of these parameters, the surfactant will ultimately degrade underground.

3.3.1 Thermal stability setup

The surfactant solutions were tested at high temperatures and high pressure, at anaerobic conditions using oxygen free gas caps, and at different and solution pH's. The setup consisted of a custom-made steel containers capable of holding 10 ml glass tubes as shown in Figure 3-2 A. These steel containers were connected to the helium or nitrogen gas tank in groups of 4 (Figure 3-2 B). A full schematic of the system is shown in Figure 3-3.



Figure 3-2. (A) Steel holder and 10 ml glass tube (B) Steel holders connected to central gas lines inside oven

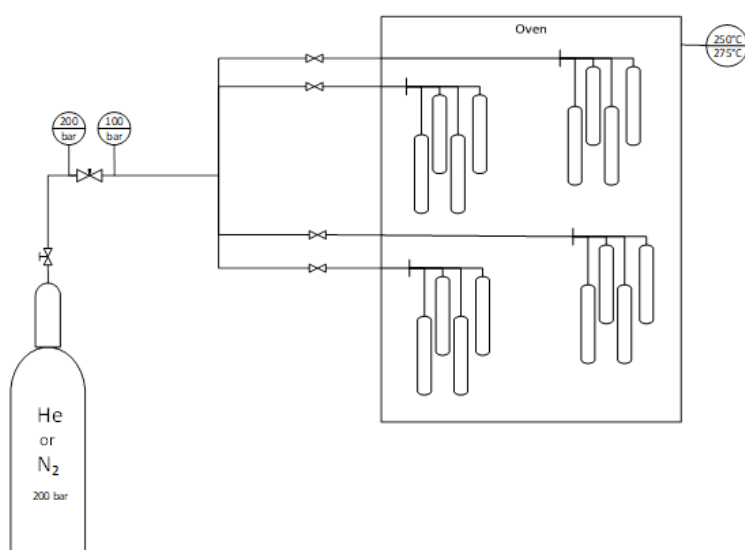


Figure 3-3. Thermal stability setup diagram indicating grouping of the containers steel holders and location of the valves

3.3.2 Thermal stability experiments

Test Series I: Surfactants A, B, C and D

In the first run of experiments, surfactants A, B, C and D at a concentration of 2% wt. of active matter in the 5-salt brine (Table 3-2) were tested for 1, 2, 4 and 8 days at 250°C and 100 bar, under anaerobic conditions to prevent any oxidation. For this last condition, the solutions were degassed for 30 min with the help of a vacuum pump. Then, the transfer of solution to the glass tubes and steel containers was carried out inside a glove bag with a nitrogen atmosphere as illustrated in Figure 3-4.



Figure 3-4. Glove bag with Nitrogen or Helium atmosphere and vacuum pump

Test Series II: Surfactants A, B, C and D

For the second run of experiments, the same methodology was applied, except the temperature was increased to 275°C.

Test Series III: Surfactants B, C, E and F

The initial pH of the brine was 6.7. This is because the pH of the demineralized water used in the laboratory is also 6.7. However, the pH of the production brine, which serves as a feed water of the steam generators, is 8.5. Moreover, an alkaline environment has been shown to be beneficial in limiting the autocatalytic degradation of surfactants [22]. For this reason, it was decided to increase the brine pH to 10 and test Surfactant B and Surfactant C at this pH, with the aim of potentially improving the performance. In addition, it was decided to replace the nitrogen gas with Helium, due to its lower solubility in water. This replacement was made to avoid the foaming that occurred once the samples were out of the oven and the temperature and pressure had decreased to room temperature and atmospheric pressure. It was desirable to

avoid foaming, as shown in Figure 3-5, to prevent any possible loss of material when depressurizing the metal containers. Any loss of material could potentially affect the organic active matter concentration in the glass sample tubes.



Figure 3-5. Close-up view of foaming (caused by dissolved oxygen) in a 10 ml glass tube after depressurization to atmospheric pressure

Test Series IV: Surfactants B, E and F

With the help of an oxygen-meter, it was possible to determine that the oxygen concentration in the solutions decreased to <1.0 mg/l after degassing. To determine if this quantity of oxygen could affect the results, the oxygen scavenger, sodium bisulfite, was also added to Surfactant B to remove any remaining dissolved oxygen. Also, it was added to determine if it had any influence on the surfactant degradation at 275°C.

Tests are summarized in Table 3-3.

Table 3-3. Summary table of conditions of thermal stability tests at 100 bar

| Number | Temperature [°C] | Surfactant | Time Step [days] | Comments |
|--------|------------------|---------------|--------------------------|---|
| I | 250 | A, B, C and D | 0, 1, 2, 4 and 8 | N ₂ gas cap. Brine pH 6.7-7. |
| II | 275 | A, B, C and D | 0, 1, 2, 4 and 8 | N ₂ gas cap. Brine pH 6.7-7. |
| III | 250 | B, C, E and F | 0, 1, 2, 4, 8, 16 and 32 | He gas cap. Brine pH 7 for E and F. Brine pH 10 for B and C. |
| IV | 275 | B, E and F | 0, 1, 2, 4, 8, 16 and 32 | He gas cap. Brine pH 7. B tested with and without oxygen scavenger. |

Finally, as previously arranged with the different manufacturers of the surfactants, the matured samples of the surfactants were sent to the manufacturer's laboratories to track the remaining surfactant active matter by mass spectrometry and titration.

3.4 Critical Micelle Concentration

Due to confidentiality issues, it was not permitted to determine the CMC of the surfactants, except for Surfactant A and B. To determine the CMC of Surfactants A and B, dilutions were prepared in the 5-salt brine at the following concentrations: 1, 0.1, 0.01, 0.001, 0.0001% wt., and 0.5, 0.05, 0.005, 0.0005 and 0.00005% wt. Then, the static and dynamic surface tension was measured using the Kibron EZPi^{plus} tensiometer shown in Figure 3-6.

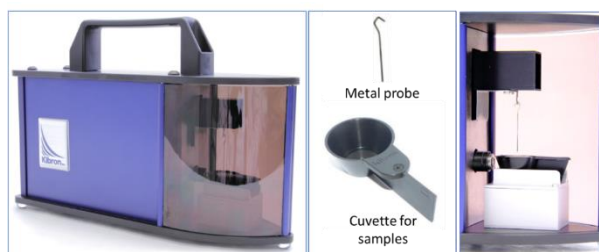


Figure 3-6. Kibron EZPi^{plus} Tensiometer

3.4.1 Static Surface Tension

The static surface tension measurement is based on the Du Noüy-Padday method where the maximum force exerted by the surface tension is recorded. First, the metal probe is immersed into the cuvette (step 1 in Figure 3-7) filled with 3 ml of solution; then, the probe is withdrawn from the cuvette (step 2). The maximum force is reached at the moment of separation between the probe and the sample solution as illustrated in step 3 of Figure 3-7. For all concentrations prepared, the static surface tension was measured after each solution had reached equilibrium. To allow the solution to reach equilibrium, several measurements were taken over a period of a least 20 minutes until the results did not differ.

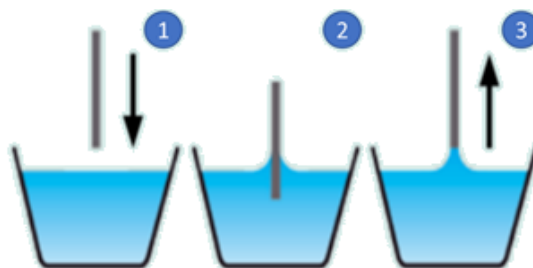


Figure 3-7. Du Noüy-Padday steps to measure surface tension [40]

3.4.2 Dynamic Surface Tension

The dynamic measurements are based on the Wilhelmy technique. First, to wet the probe, it is lowered to the surface of the liquid and immediately withdrawn. Then, it is again immersed into the cuvette with the surfactant sample. While the probe is immersed, the force pulling the probe is being recorded over time as shown in Figure 3-8 (A). The common behavior of the dynamic surface tension for a range concentration is shown in Figure 3-8 (B); surface tension decreases with time, until a constant value is reached. As can be seen, at concentrations lower than the CMC it takes longer to reach a steady state value of the surface tension.

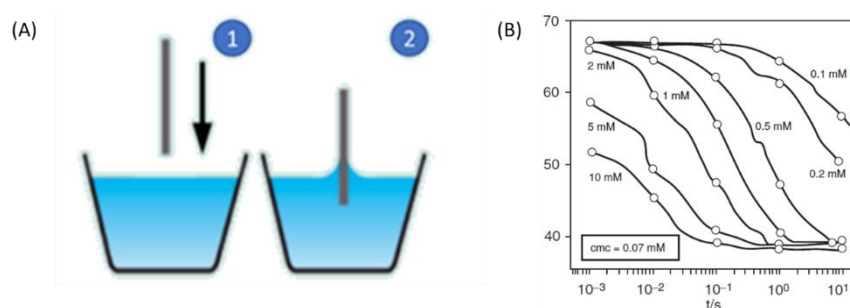


Figure 3-8. (A) Steps to measure dynamic surface tension. (B) Dynamic surface tension behavior for a surfactant at different concentrations (mM = millimolar).[40] [10]

3.4.3 Determination of CMC

To determine the CMC, the surface tensions vs. concentration were plotted on a logarithmic scale. At lower surfactant concentrations, the surface tension changes sharply. After reaching the CMC, the surface tension remains constant. Hence, the CMC lies at the intersection between the steep and the flat slopes as illustrated in the Figure 3-9.

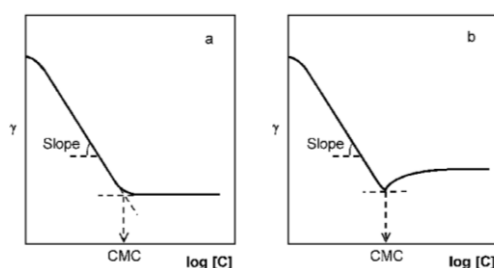


Figure 3-9. Surface tension (γ) as a function of surfactant concentration (A) for pure surfactant (B) for surfactant containing impurities. [10]

3.5 Foam Quality

Selected surfactants from the thermal stability experiments were tested for their capacity to produce foam in a porous medium at 60°C, 120°C, and 180°C; by measuring the pressure drop along a rock core while surfactant solutions and nitrogen were simultaneously injected into the core at different liquid and gas fractions but maintaining a constant total flowrate.

3.5.1 Foamability Tests Setup

A schematic diagram of the core flood set-up is shown in Figure 3-10, and the corresponding physical set-up in the lab is shown in Figure 3-11. The liquid flow was controlled by a Vindum liquid pump and the nitrogen flow rate was controlled by a Bronkhorst mass flow controller. The total flow rate was 0.1 ml/min. A back pressure of 20 bar was applied to the whole system using a back-pressure regulator.

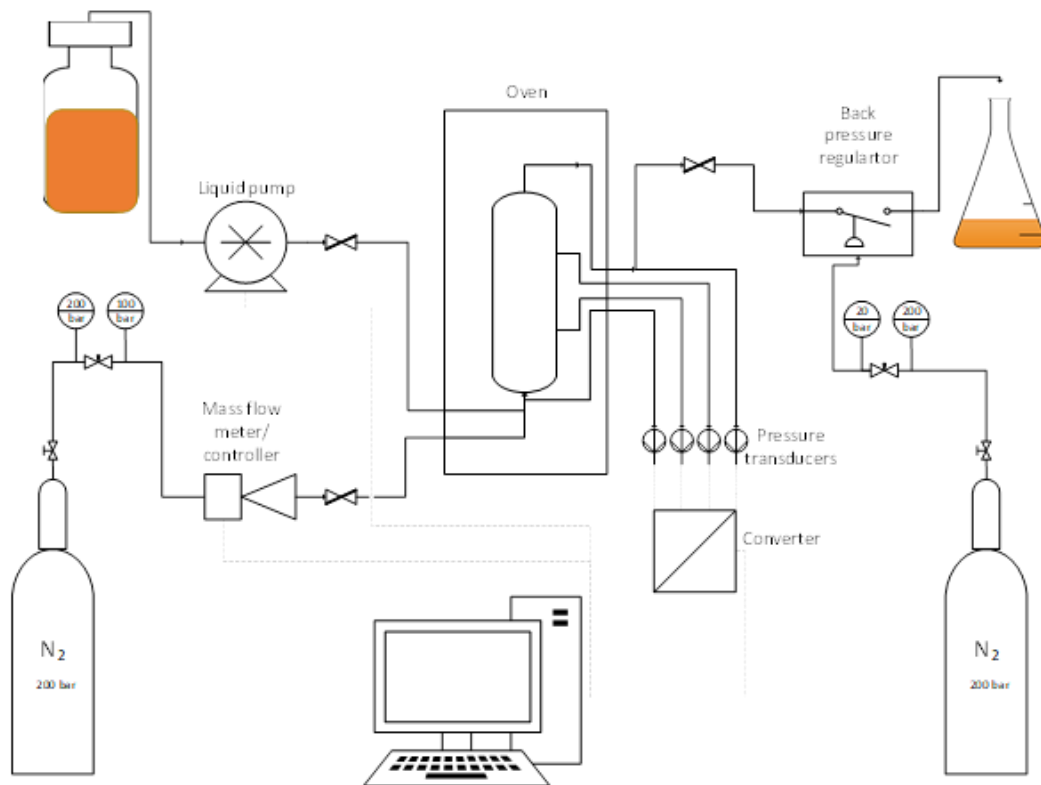


Figure 3-10. Schematic diagram of the core flooding set up

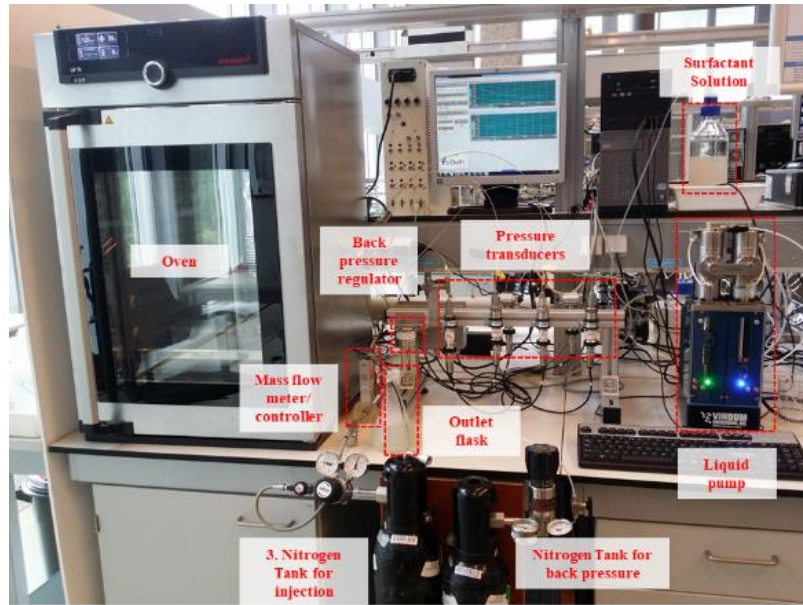


Figure 3-11. Illustration of core flooding setup

Bentheimer sandstone cores were glued with epoxy resins, then placed into aluminum core holders in the oven. Four pressure transducers were connected to the core, one at the inlet, one at the outlet, and two in the middle of the core as shown in Figure 3-12. To connect the two pressure transducers in the middle of the core, two pressure taps were drilled, with a separation of 6.5 cm.

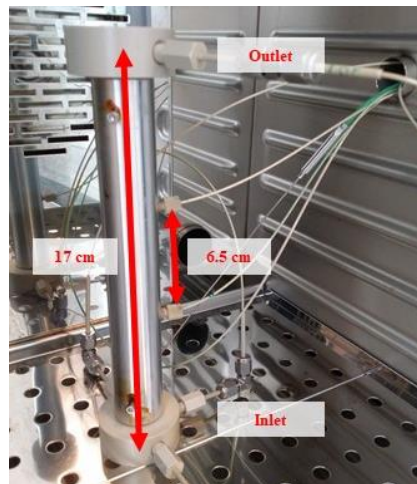


Figure 3-12. Aluminum core holder inside oven, showing the connection to the inlet and outlet streams, and the locations of the two pressure taps

3.5.2 Correction of volumetric flow rate of injected gas

Given that the mass flow controller had been calibrated to operate at 150 bar, whilst the nitrogen inlet pressure for this experiments is 100 bar, the gas volumetric flowrate input value must be corrected as follows [41]:

$$Q_{MFC} = Q_{FQ} \times MFC_{factor} \quad (12)$$

where,

- Q_{MFC} is the gas volumetric flow rate that should be input into the Mass Flow Controller [ml/min].
- Q_{FQ} is the gas volumetric flow required for the desired foam quality [ml/min].
- MFC_{factor} is the correction factor obtained from the FLUIDAT online software. FLUIDAT is the manufacturer of the mass controller.
- The pressure in the core must also be taken into account when setting the flowrate on the mass flow controller. $P_{midpoint}$ is the absolute pressure at the center of the core, and is calculated as an average of pressures measured by two transducers in the middle of the core as shown in the Figure 3-12.

The final volumetric flow rate that should be set on the mass flow controller is therefore defined as:

$$Q_{MFC} = Q_{FQ} \times MFC_{factor} \times P_{midpoint} \quad (13)$$

Finally, to verify the actual volumetric flow rate injected, after the test, the following formula is used [41]:

$$Q_{FQ,actual} = \frac{Q_{MFC}}{MFC_{factor}} \times JS_{CF} \quad (14)$$

where,

JS_{CF} is the Jacobson Stewart correction factor, which is the ratio of the Jacobson Stewart molar density of the gas at the midpoint pressure to the Jacobson Stewart molar density of the gas at atmospheric pressure.

3.5.3 Core Samples

Bentheimer sandstone cores were used for these core flood tests, and an example of a typical core is given in Figure 3-13. The characteristics of these cores are listed in Table 3-4.



Figure 3-13. Bentheimer sandstone core.

Table 3-4. Bentheimer sandstone core characteristics.

| Characteristic | Value |
|----------------------|-------|
| Clay content [%][42] | 2.7 |
| Porosity [43] | 0.23 |
| Length [cm] | 17 |
| Diameter [cm] [44] | 0.994 |
| Pore Volume [ml] | 3.03 |

3.5.3.1 Permeability Measurement

The permeability of the cores was obtained by measuring the pressure drop (ΔP) along the core while injecting tap water at different flow rates (Q_w). The permeability (k) is calculated from the slope of the plot of the pressure gradients vs. the water flow rates; by rearranging Darcy's Law as follows [45]:

$$\frac{\Delta P}{L} = \frac{\mu_w Q_w}{k A} \quad (15)$$

Where,

A = Core cross sectional area

μ_w = Tap water viscosity (30°C)

The permeability was measured at the beginning of testing, and after cleaning the cores, when a different surfactant was injected. The average permeability of the Bentheimer was $1.33 \times 10^{-12} \text{ m}^2$.

3.5.4 Surfactant solutions composition

The concentration of surfactant in the flooding solutions is listed in Table 3-5: The decision to use demineralized water and a NaCl brine, instead of the original brine recipe (Table 3-1), is related to the results of the solubility tests will be discussed in the Chapter 4.

Table 3-5. Surfactant solution compositions for core flooding

| | Surfactant B | Surfactant C | Surfactant E | Surfactant F |
|---------------------|---------------------|---------------------|---------------------|---------------------|
| Concentration [wt%] | 0.5 | 0.5 | 0.5 | 0.5 |
| Solvent | Demi water | Brine | Brine | Brine |
| NaCl [mg/l] | - | 4.851 | 4.851 | 4.851 |

3.6 Static and Dynamic Adsorption

The purpose of these experiments was to measure the amount of surfactant being absorbed by the reservoir rock during the flooding of the reservoir. The aim to select the surfactant that is less easily absorbed.

3.6.1.1 Static Adsorption Test

7 g of 1wt% of Surfactant B, C, E and F in brine (Table 3-2) were mixed with 3 g of reservoir rock in a 10 ml glass tube. Each set of four surfactants was placed into an oven at 24°C, 60°C and 90°C for 72 hours. Every 24 hours the glass tubes were shaken for 1 minute. After the samples were taken out from the oven, they were centrifuged for 30 minutes as shown in Figure 3-14. From the centrifuged samples, 0.5 ml of solution were taken and diluted by a factor of 20 in demi water. The total organic content (TOC) of each diluted sample was then measured and compared to the TOC of the surfactant solutions not in contact with the reservoir rock.



Figure 3-14. Crushed reservoir rock and surfactant solution after being centrifuged

3.6.1.2 Dynamic Adsorption Test.

The same setup and type of core described in Section 3.5 for the foam quality tests was used for the dynamic adsorption tests. The surfactants were injected at 120°C different concentrations, 0.05% and 0.5wt% Potassium Iodide (KI) was added as a tracer at a

concentration of 0.3% and 0.4wt% The effluent samples were collected in a fraction collector every 0.1 pore volumes (i.e. 0.3 ml). The flowrate was 0.1 ml/min, the same as that used in the core floods. The total volume injected was 3 pore volumes at each concentration to allow the core to absorb as much surfactant as possible.

The TOC was measured to determine the surfactant concentration, as with the static adsorption tests. The KI was measured by spectrophotometry. The normalized concentration $[C/C_0]$ vs. the pore volumes produced was plotted for both the surfactant and the tracer as in the example shown in Figure 3-15. Normalized concentration vs. pore volumes produced of Surfactant and tracer. The dotted lines represent the breakthrough. The surfactat loss, in this case is equal to 0.9 PV. The breakthrough difference indicates the total pore volumes loss of surfactant. Finally, the concentration absorbed in terms of $\text{mg}_{\text{surfactant}}/\text{g}_{\text{rock}}$ was determined.

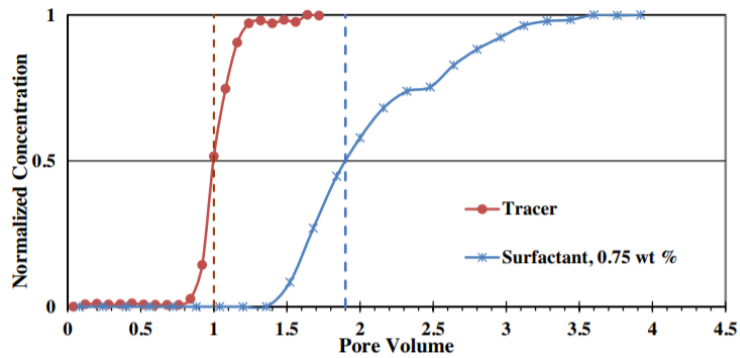


Figure 3-15. Normalized concentration vs. pore volumes produced of Surfactant and tracer. The dotted lines represent the breakthrough. The surfactat loss, in this case is equal to 0.9 PV [46]

4 Experimental Results and Analysis

4.1 Solubility

After resting for 24 hours, from the 6 surfactants prepared at a concentration of 2wt%, only Surfactant B presented a precipitate, Meanwhile, the other surfactants look homogeneous as shown in Figure 4-1.



Figure 4-1. Surfactants A, B, C, D and E at a concentration of 2wt% after 24 hours under static conditions

Surfactants E and F were transparent and homogeneous with no precipitate. This can be explained either by the double sulfonate anion and by the oxygen atom joining two sulfonate molecules as shown in Table 3-1; which mean that there are more oxygen atoms in the head of the surfactant to interact with the water molecules. It was previously shown that adding alkoxy (R-O⁻) units increased the tolerance of surfactants to divalent cations and solubility in high salinity environments [28]. It was also shown that N-ethoxy (an alkoxy group with a 2-carbon molecule from one side) sulfonates are stable and soluble when high salinity and high temperatures are present [47].

In contrast, Surfactants A, B, C and D showed a milky appearance that is unusual compared to what is seen typically in the oil industry for enhanced oil recovery processes. By applying the methodology “Diagnostic Guide to Visual and Microscopic Observations of Surfactant Systems for interpreting visual observations of surfactant dispersions” [39], described in the previous chapter, to Surfactants A, B, C and D, the following general characteristics were detected:

- i. No visually resolvable particles or droplets observed for any solution.
- ii. Observation of one visible discernible homogeneous layer, with no apparent change upon gentle stirring, for Surfactant A, C and D. Observation of one inhomogeneous discernible layer that changed upon gentle stirring for Surfactant B.

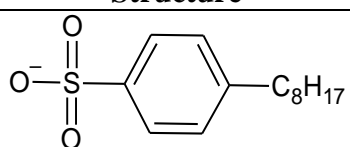
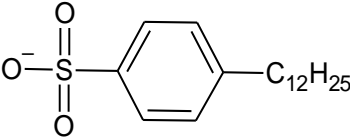
- iii. Observed that the milky appearance of all surfactants tested became foggy when using thinner/smaller glass containers.

It is specified [39] that these characteristics might indicate large particles with a size of 0.5 μm or more and a two-phase dispersion. Nevertheless, the behavior of these solutions is at room temperature, while the application and further experiments were carried at higher temperatures.

4.1.1 Enhancement of Surfactant B Solubility

The Surfactant B solution showed visible precipitation at room temperature with the 5-salt brine (Table 3-2), with NaCl brine, and also with demineralized water. This can be explained by the Krafft point temperature, which suggests that anionic surfactants would precipitate if the temperature is lower than the Krafft point [47]. Before this point, surfactants become ineffective and drop out of the aqueous solution. Also, longer tails generally lead to lower solubility of water and a higher Krafft point [48]. The Krafft point values are presented in Table 4-1 [49] for two linear alkylbenzene sulfonates.

Table 4-1. Krafft point for Octyl- and Dodecyl-benzene sulfonates, for their sodium salts

| Surfactant | Structure | Krafft Point [$^{\circ}\text{C}$] |
|---------------------------|---|-------------------------------------|
| Octyl-benzene sulfonate |  | 26 |
| Dodecyl-benzene sulfonate |  | 62.5 |

As can be seen, the Krafft point increases with respect to the number of carbons in the alkyl chain. Surfactant B is a linear toluene sulfonate with a long alkyl chain of 18 carbons as seen in Figure 4-2.

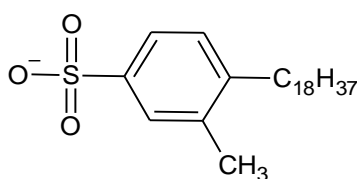


Figure 4-2. Linear Toluene Sulfonate with an alkyl chain of 18 carbons

For this reason, Surfactant B was heated to 90°C for 24 hours. After this time, the solubility improved considerably as a one-phase dispersion with no precipitate was observed. The dispersion was stable for one week, after which precipitation started again. It was possible to get a better appreciation of the effect of temperature on solubility if the glass tubes were inverted as demonstrated in Figure 4-3.



Figure 4-3. Surfactant Bin demineralized before and after heated at 90°C for 24 hours

Divalent cations as magnesium (Mg^{2+}) and calcium (Ca^{2+}) also have the potential effect of causing surfactant precipitation which can result in blocking of the pores. Anionic surfactants are more sensitive to these divalent cations. Particularly, surfactants with an aryl group (Figure 4-4). It has been previously found that problems with stability and effectiveness of surfactant solutions increase with high concentration of divalent cations such as Ca^{2+} , Mg^{2+} , etc. (more than 3000 ppm) [47]. The 5-salt brine used for this experiment has 115 ppm of Ca^{2+} and Mg^{2+} .

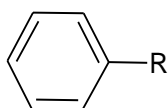


Figure 4-4. Aryl group generic formula, which are those compounds containing an aromatic ring

4.2 Thermal Stability

For this section, the results of each test series are correlated with the visible state of each solution, after being matured at high temperatures. Then, the behaviour of each surfactant at high temperatures is explained from a chemical point of view.

4.2.1 Test Series Results

4.2.1.1 Test Series I: 250°C, Surfactants A, B, C & D

As described in the previous chapter, the first series of the thermal stability tests consisted in evaluating Surfactants A, B C and D at 250 °C and 100 bar under N₂ gas cap. From this experiment it was determined that Surfactant A and B were the most stable, both showing a decline of active matter of less than 20%. Consistently, their appearance looked homogeneous and slightly clearer over time (Figure 4-5). However, for Surfactant A, a thin layer of an oily brown substance could be noticed on top. It was also perceived that Surfactant B improved in solubility at 250°C, as no precipitate is present after 1 day of aging.

From the mass spectrometry analysis to determine the surfactant organic matter remaining, results show a higher concentration after 1 day than the control sample without aging. An improved solubility at higher temperature could be the cause, as the control sample, that was always at room temperature, precipitated quickly even after just being shaken. Also, evaporation could have increased the concentration in the aged samples, because some condensate was found in the metal containers outside the glass tubes.

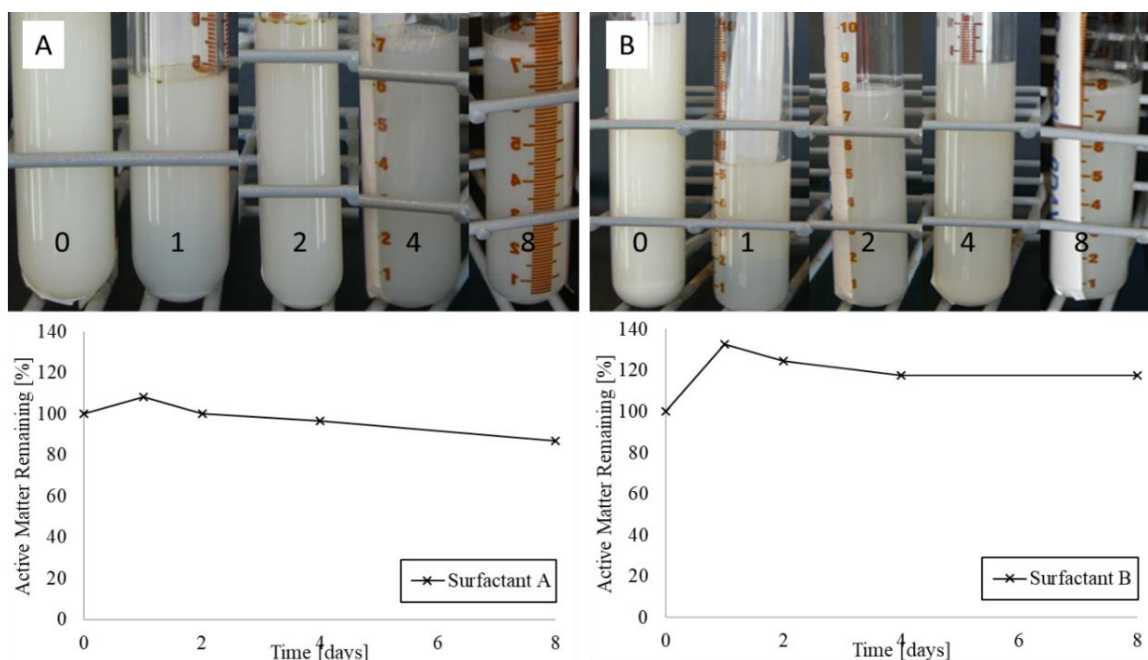


Figure 4-5. Surfactants A and B active matter remaining after 0, 1, 2, 4 and 8 days at 250°C and 100 bar

In contrast, surfactant C and D exhibited a deep decline of active matter, corresponding to a change in color from milky to transparent, with a separation of phases and the presence of a white and yellow precipitate. These changes are more drastic beyond 1 day of aging as shown in Figure 4-6.

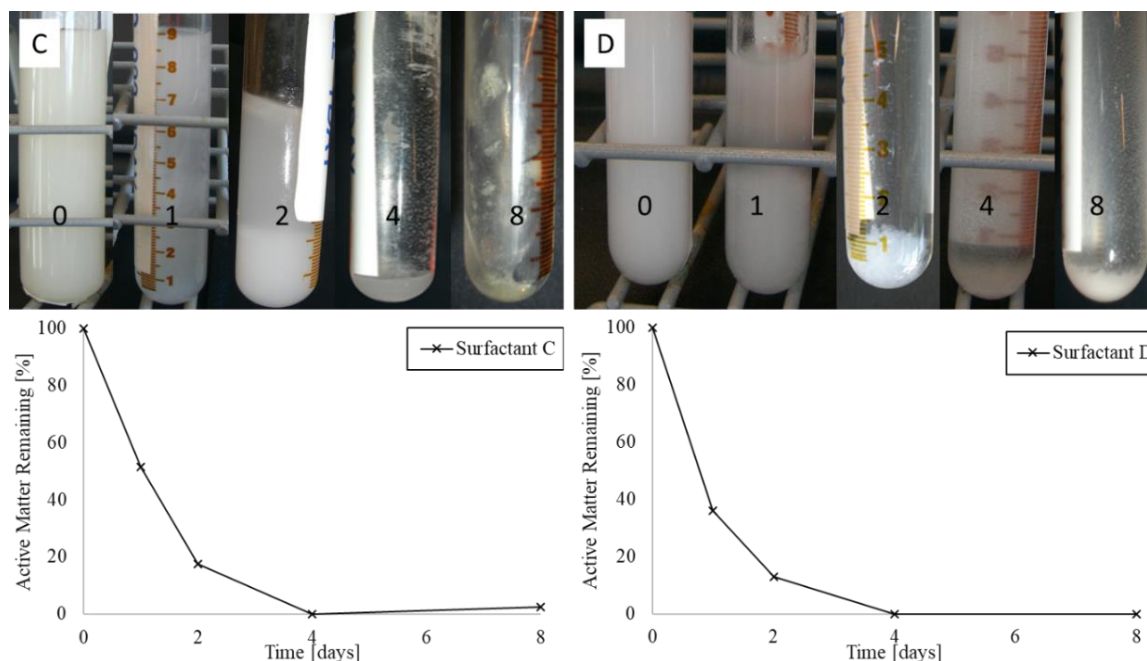


Figure 4-6. Surfactants C and D active matter remaining after 1,2, 4 and 8 days at 250°C and 100 bar

4.2.1.2 Test Series II: 275°C, Surfactants A, B, C & D

At 275 °C, Surfactant A was no longer stable, with an active matter decline of 92% after 8 days of aging. Again, it presented droplets of a brownish oily substance; although in a greater quantity. It also formed a precipitate in the 8-day sample; and finally, an increase in transparency, as showed in Figure 4-7. Moreover, a H₂S and SO_x odor was perceptible when opening the sample tubes, starting at the 4-day sample. In contrast, Surfactant B revealed again a homogeneous single-phase appearance which agrees with the chemical analysis, reflecting no decline of active matter; on the contrary, the measured surfactant organic matter increased by a factor of between 20 to 40%. The possible cause is the evaporation of some of the water that condensed out of the glass tubes, once the steel containers were brought to room temperature.

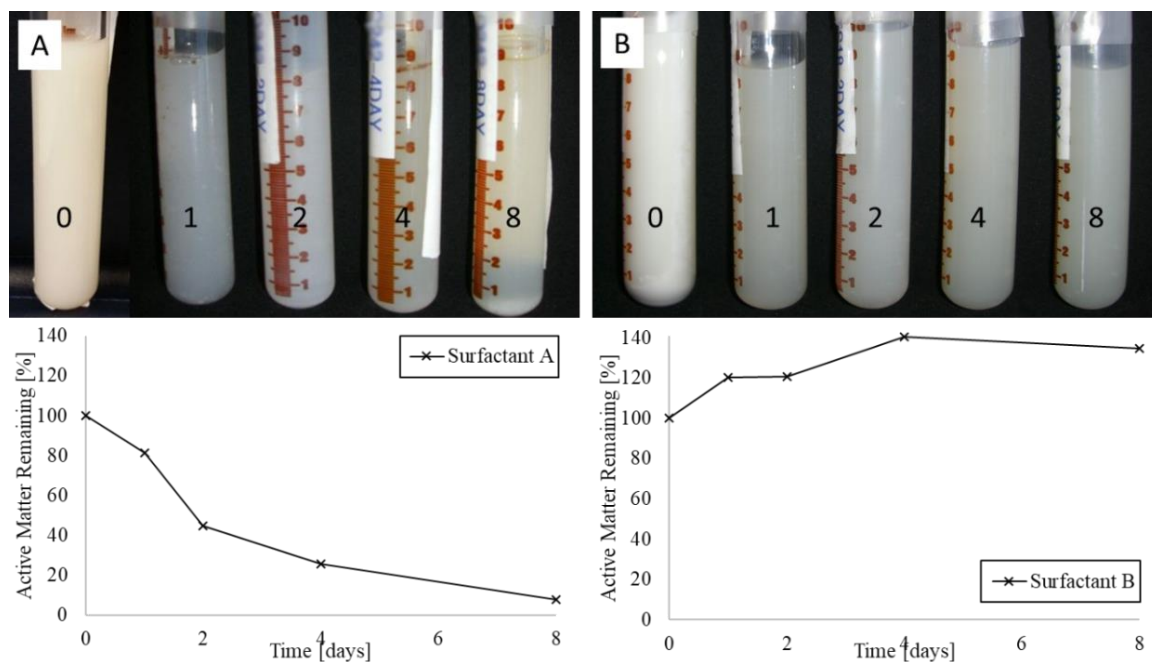


Figure 4-7. Surfactants A and B active matter remaining after 0, 1, 2, 4 and 8 days at 275°C and 100 bar

Similarly, to test series I, the active matter decreased for Surfactants C and D quickly. The rate was higher than at 250°C, and very low concentrations were reached after just 1 day of aging. However, Surfactant D active matter was stabilized between 3 and 8%, rather than declining to zero, as seen in Figure 4-8.

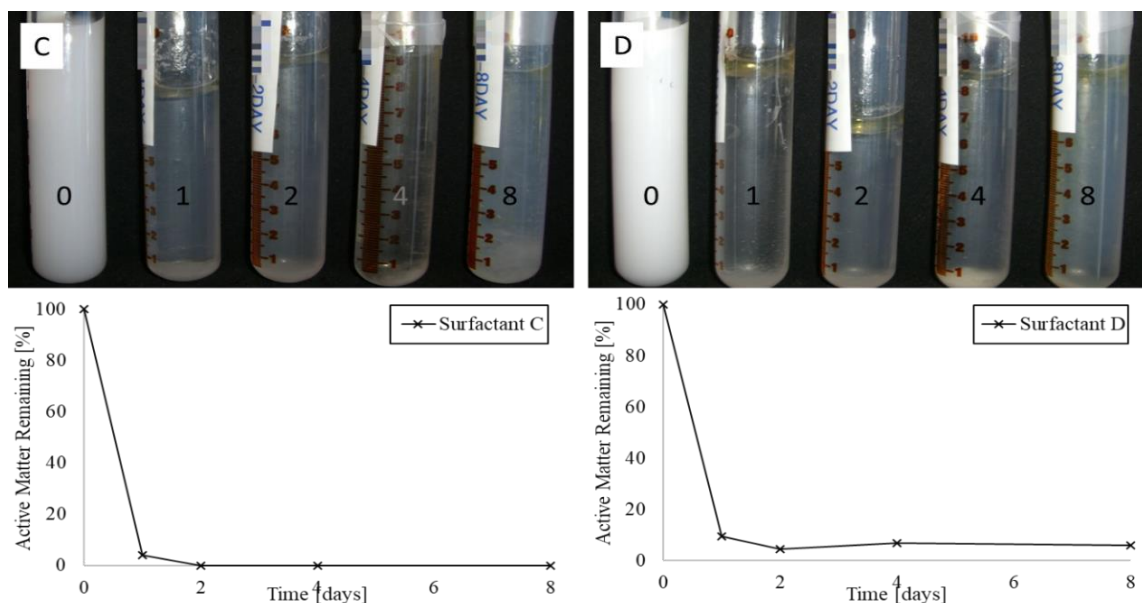


Figure 4-8. Surfactants C and D active remaining after 0, 1, 2, 4 and 8 days at 275°C and 100 bar

4.2.1.3 Test Series III: 250°C, Surfactants B, C, E & F

As illustrated in Figure 4-9, the 16 and 32-day samples of Surfactant B still looked homogeneous, and the chemical analysis results confirmed that it is stable after 8 days of aging and up to 32 days. Surfactant C also showed the same behavior as before, including: change in color, precipitate and oily layer on top. The chemical analysis results were similar to before, except for the 4-day sample that showed around 60% of surfactant active matter remaining, which was unusual compared to the previous sets. The reason for this spurious data point is not clear.

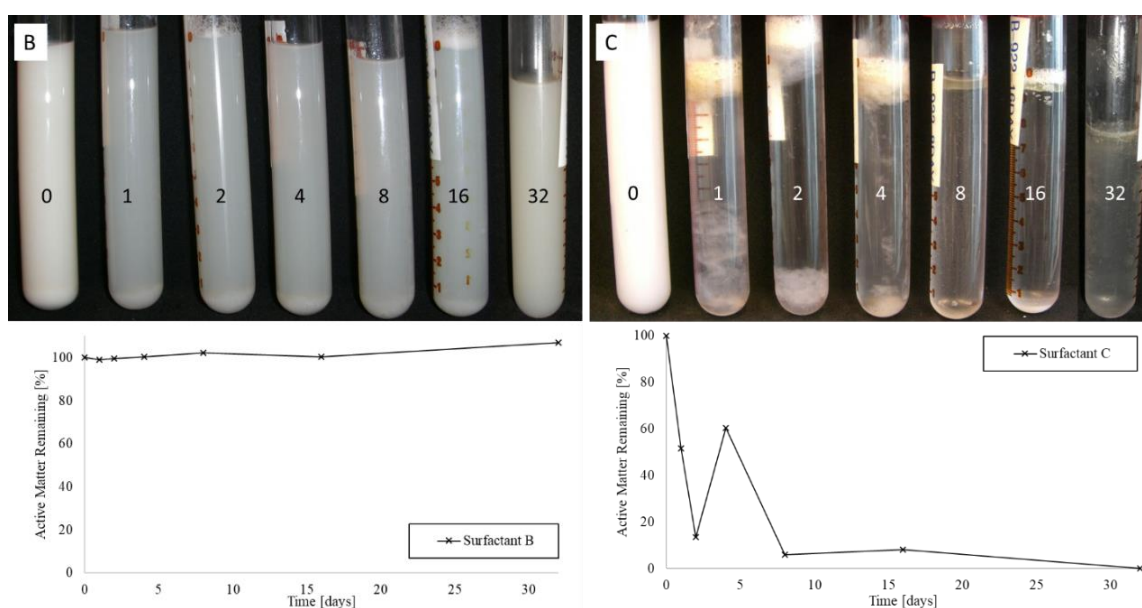


Figure 4-9. Surfactant B and C active matter remaining after 0, 1, 2, 4, 8, 16 and 32 days at 250°C and 100 bar

In Figure 4-10 it is possible to observe that Surfactant E and F behaved similarly during the 32 days of aging. They were both stable until the 4th day of maturation, after which, a drastic decline in the surfactant active matter was detected. This behavior coincides with the homogeneous appearance of the first 4 samples (except for the turbidity of the 2-day sample) and with the appearance of the brown oily layer on top on the 8, 16 and 32-day sample. A similar layer was also present in Surfactant A, C and D (Figure 4-7 and Figure 4-8). It is suggested that the oily layer is a break down product of the surfactant; containing the alkyl chain separated from the hydrophilic head [50].

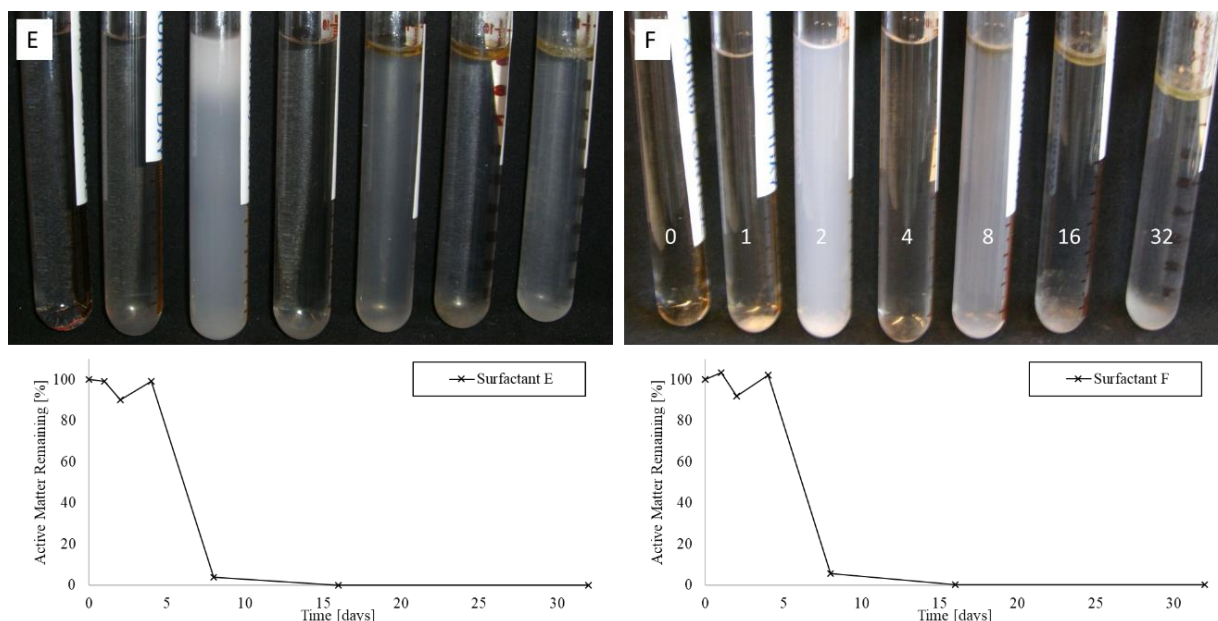


Figure 4-10. Surfactant E and F active matter remaining after 0,1,2,4,8,16 and 32 days at 250°C and 100 bar

4.2.1.4 Test Series IV: 275°C, Surfactants B, C, E & F

Even though all samples of Surfactant B at 275°C looked generally homogeneous; a very small droplet of a brownish oily substance was perceived on top as seen in Figure 4-11. This is possibly because during this set of experiments, a new batch of Surfactant B was used.

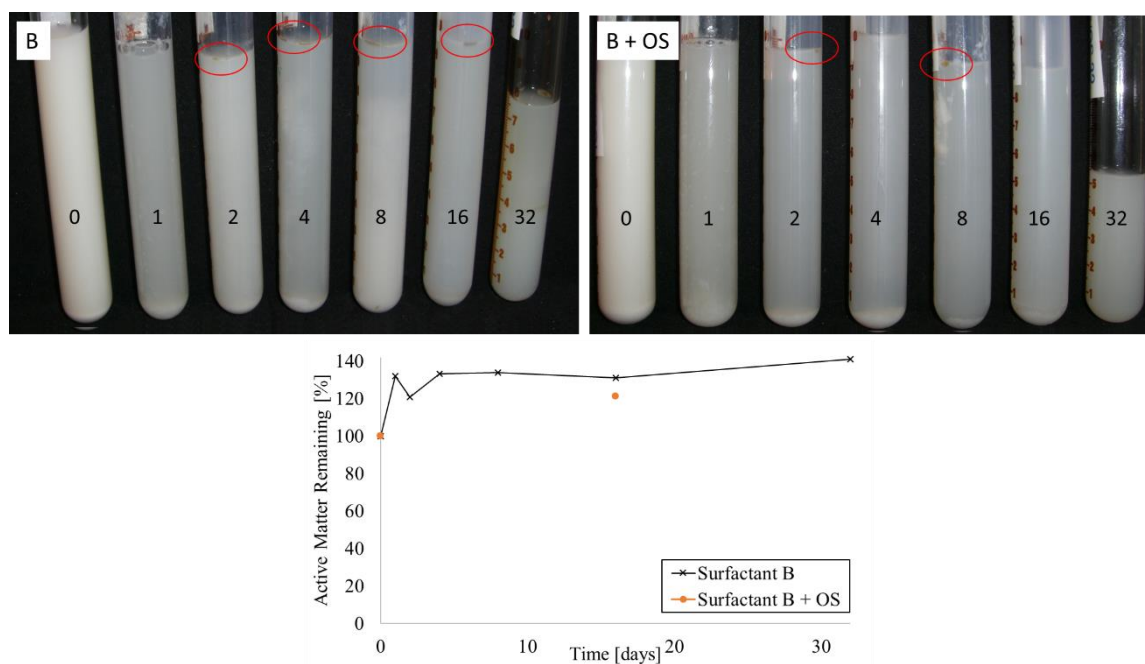


Figure 4-11. Surfactant B with and without oxygen scavenger, active matter remaining after 32 days at 275°C and 100 bar

Regarding the use of sodium bisulfite as an oxygen scavenger, there was no apparent change in the appearance of the surfactant. For this reason, it was assumed that no effect on the concentration of surfactant active matter should occur and therefore, only the 0 and 16-day were sent to be analyzed and these showed similar values to the sample without the oxygen scavenger. However, for the 32-day samples for both Surfactant B and Surfactant B+OS, white deposits appeared outside and inside the glass, specifically in the upper section. The effect was more drastic in the sample of Surfactant B+OS as seen in the Figure 4-12.



Figure 4-12. 32-day sample tubes, of Surfactant B and Surfactant B+OS, inside metal containers showing a white deposit

An X-Ray Fluorescence (XRF) analysis was carried out on the white deposit in order to know its composition. According to the results, this material consisted mainly in SiO_2 (91.45wt%), Na_2O (4.31wt%), Al_2O_3 (2.31wt%) and other traces. Therefore, as there is no other source of silicon in the setup or surfactant solutions rather than the glass tubes, it is believed that a modification of the surface of the glass occurred during the maturation time. The three main reactions that modify the surface of glass are: 1) weathering (i.e. leaching and corrosion by humidity), 2) ion exchange and 3) reactions in aqueous phase [51]. These kind of reactions and the final product depend on parameters such as the chemical composition of the glass, the physical characteristics of the glass surface, content of water, temperature, pH and the presence of alkaline ions [51].

The reaction of acid gases, such as SO_2/SO_3 , with the alkali in a glass surface is an ion exchange reaction that is known to alter the physical, chemical, and mechanical properties of a glass surface [52]. The effect of the process is the removal of the alkali from the glass, or any other species that are mobile and can leaving a surface that is enriched in silica (i.e. SiO_2) [52]. It is more likely that this kind of reaction happened inside the metal holders.

4.2.2 Analysis of Surfactant Thermal Stability

4.2.2.1 Surfactant A

Surfactant A was stable at 250°C for 8 days; although with a decrease of 13% in the surfactant active matter. However, at 275°C, the decline was significantly sharper and tending to 0 as shown in Figure 4-13. In the Chapter 3, it was stated that Surfactant A is categorized as an internal olefin sulfonate. It has previously been demonstrated that the presence of the sulfonate units makes the internal olefins stable at high temperatures up to 200 °C [47]. The desulfurization of the molecule as indicated by the production of H₂S and SO_x (Section 4.2.1.2) would follow a decomposition rate that increases exponentially with temperature [22]. This explains the difference of performance by an increase of just 25°C.

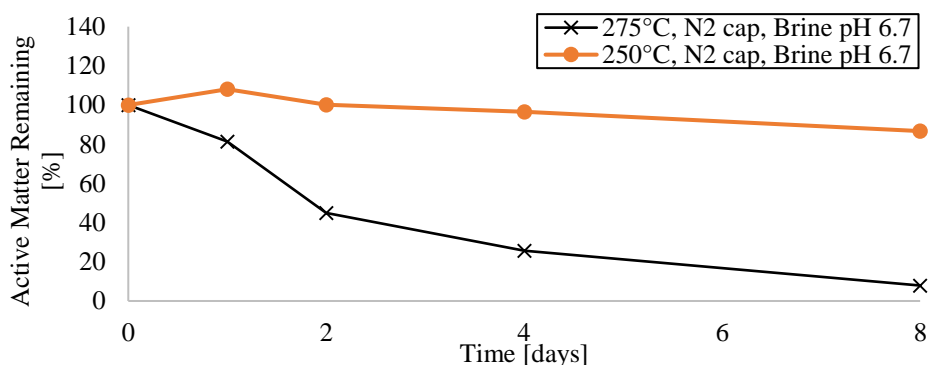


Figure 4-13. Thermal Stability of Surfactant A at 100 bar

4.2.2.2 Surfactant B

Surfactant B exhibited the best performance among the 6 surfactants tested. There was no signal of thermal degradation after 32 days of maturation as shown in Figure 4-14. It was previously demonstrated that a long-chain linear toluene sulfonate exhibited an optimum temperature performance at temperatures as high as 275°C and performed better when compared to an alpha-olefin sulfonate [53]. Similarly, in another study, an alkylbenzene sulfonate outperformed a secondary alkane sulfonate at 300°C [54]. This might indicate that the difference in stability at temperatures higher than 250°C is due to the presence of the benzene ring (or toluene in Surfactant B) in the molecule making a stronger bond with the Sulphur atom. It can be seen in

Table 4-2 how the bond dissociation energy, which is the energy required to break a bond, increases when a benzene group is present in the molecule, compared to the same non-metal

element attached to an alkyl group. The greater the dissociation energy, the more stable a bond is.

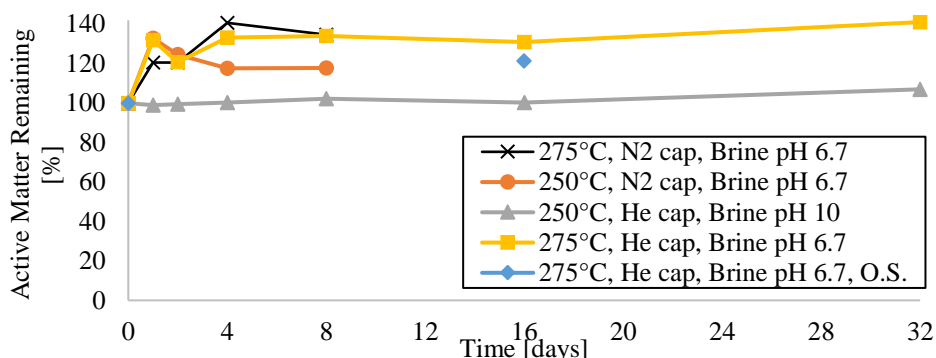


Figure 4-14. Surfactant B, thermal stability at 100 bar

Table 4-2. Dissociation Energy of non-metal and carbon (ethyl and aryl group) bonds at 25°C.

| Bond | Dissociation Energy [kJ/mol] | Bond | Dissociation Energy [kJ/mol] |
|------------------|------------------------------|-------------------------|------------------------------|
| <chem>CCl</chem> | 338 | <chem>c1ccccc1Cl</chem> | 405 |
| <chem>CBr</chem> | 285 | <chem>c1ccccc1Br</chem> | 337 |

The substitution of nitrogen by helium for the gas cap, driven by the lower solubility of the helium, reduced foaming after cooling and depressurization. However it didn't stop the loss of mixture by evaporation that could have led to fluctuations of the surfactant active matter concentration.

Finally, the pH of the 5-salt brine, from almost neutral to basic, didn't seem to affect the stability of the surfactant under anaerobic conditions. In previous studies, a similar linear toluene sulfonate performed better at an initial pH of 11 than at a pH of 8.5, but this was under aerobic conditions [53].

4.2.2.3 Surfactant C and D

As mentioned in Chapter 3, these surfactants are classified as alkyl ether carboxylic acids. Their properties, such as solubility and foamability, depend on the molecule structure and these types of surfactants can be very sensitive to pH and temperature [38]. The absence of the sulfonate group predicts the low stability to high temperatures, and it is verified with results shown in

Figure 4-15, and where a steep decrease in the surfactant active matter is observed after just 1 day of maturation.

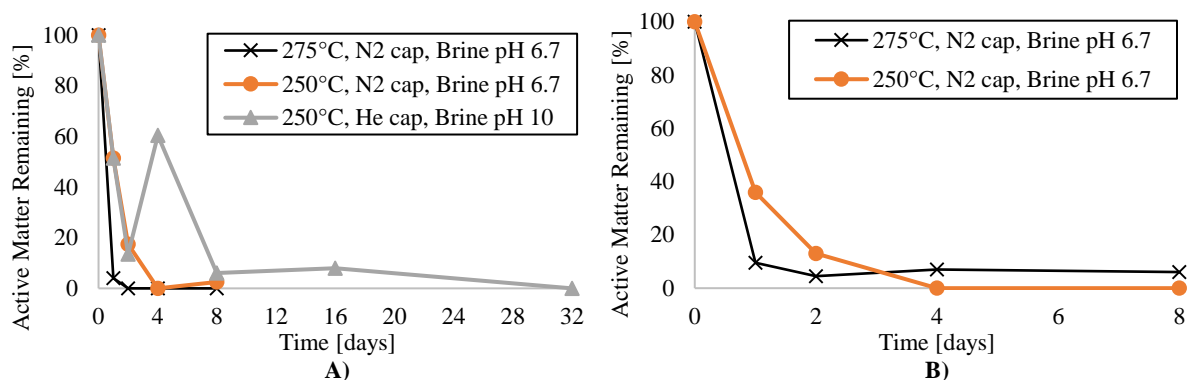


Figure 4-15. A) Surfactant C and B) Surfactant D thermal stability at 100 bar

4.2.2.4 Surfactant E and F

Surfactant E and F showed good thermal stability up to 4 days, after which it decreased severely as shown in Figure 4-16. These molecules include a sulfonate group attached to a benzene ring and it was previously discussed that these were the two conditions probably responsible for the high thermal stability of Surfactant B (Section 4.2.2.2). However, in the same studies in which a linear toluene sulfonate outperformed other surfactants [53], it was also concluded that the longer the alkyl chain length, the better the performance at higher temperatures, which suggests it is a third condition for thermal stability. In Section 4.1 it was concluded that the good solubility of these surfactants might indicated they have a short alkyl chain.

Other experiments carried out by the manufacturer [55] showed that the long-term thermal stability improved with the lack of divalent cations for up to 13 days with a brine with 1 g/l of NaCl. However, the surfactant active matter declined to less than 4% at the 30-day sample. On the other hand, by using demi water instead of brine, the surfactant active matter remained stable and close to 100% even for 30 days.

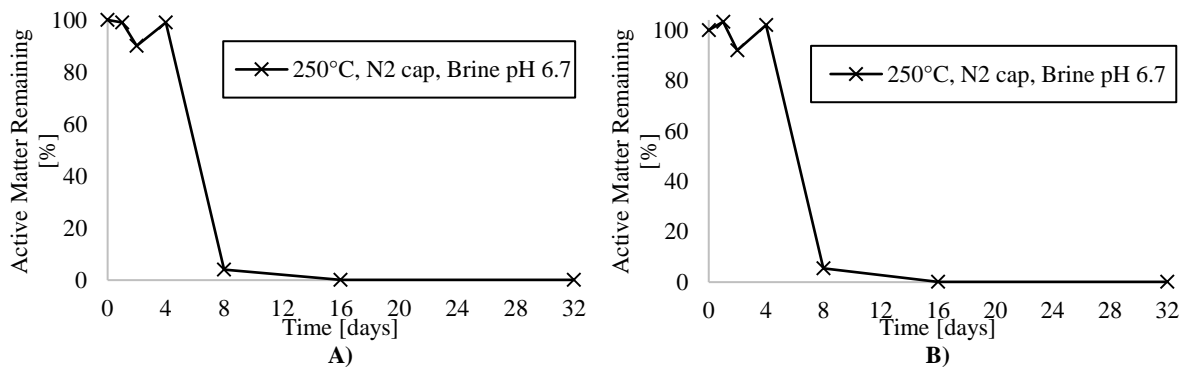


Figure 4-16. A) Surfactant E and B) Surfactant F thermal stability at 100 bar

4.3 Foam Behaviour in Porous Media

As described in the previous chapter, the performance of the surfactants was evaluated based on their ability to produce foam and therefore reduce the gas mobility in porous media. This performance was estimated by measuring the steady state pressure drop across the core while co-injecting 0.5wt.% surfactant solution in 0.685 wt.% NaCl brine and N₂ at a fixed total flow rate of 0.1 ml/min. Core floods were carried out at 60°C, 120°C and 180°C. Foam apparent viscosity (μ_{app}) and MRF and were then calculated according to formulas 3.3 and 3.4.

4.3.1 Surfactant B: Foam Quality Scan

For the first core flood at 120°C, when an initial mixture of Surfactant B with 5-salt brine was injected, the core became blocked, with the pressure gradient increased abruptly and no flow being detected at the outlet of the setup. This was due to precipitate being formed between the surfactant and the cations in the brine, and these solid particles then blocking the pores in the rock. To address this issue, it was decided to use demineralized water instead of brine and preheat the solution at 90°C for 24 as explained in Section 4.1.1. For the other surfactants, it was decided to use only NaCl brine, eliminating the cations to minimize the risk of any precipitation during test.

For Surfactant B, two effects were observed while increasing the temperature as illustrated in Figure 4-17. First, there was a reduction in the apparent viscosity by a factor of almost 34% as the temperature increased from 60°C to 120°C, and by a factor of around 15% as the temperature increased from 120°C to 180°C. This reduction in viscosity is caused by the reduction of the surface tension and liquid viscosity at higher temperatures[56]. Secondly, there was an increase in the transition foam quality, fg^* , as the temperature increased as well. In contrast, the MRF at 180°C was higher for all foam quality values than MRF at 60°C and 120°C, reaching a maximum MRF of 2818 at fg^* , 260% higher than the maximum MRF 60°C and 53% higher than the maximum MRF at 120°C.

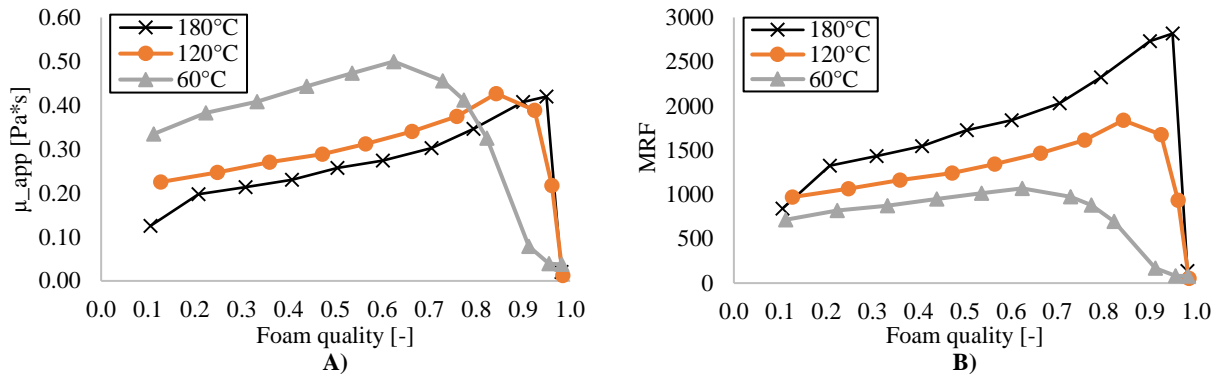


Figure 4-17. A) Apparent viscosity and B) MRF vs. foam quality at 60°C, 120°C and 180°C for Surfactant B

4.3.2 Surfactant C: Foam Quality Scan

In contrast, it can be seen Figure 4-18 that Surfactant C behaved in a completely different manner as the temperature increased. The curvature of both apparent viscosity and MRF is shifted from high to low foam quality regime dominated, until the typical shape for anionic surfactants was reached at 180°C. In previous experiments [57], bulk foam stability was tested for surfactants with the same hydrophilic head, and similar hydrophobic tails. In these experiments, the surfactant with lowest bulk foam stability had an unsaturated hydrophobic tail (i.e. double bonds present). Surfactant C has an unsaturated hydrophobic tail, whose double bonds might break as the temperature increases, generating a more stable foam.

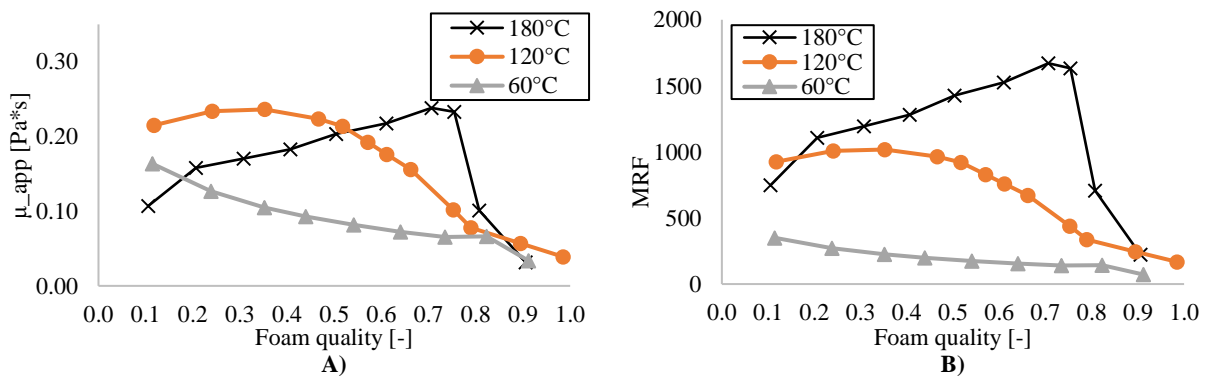


Figure 4-18. A) Apparent viscosity and B) MRF vs. foam quality at 60°C, 120°C and 180°C for Surfactant C

4.3.3 Surfactant E and F: Foam Quality Scan

Surfactants D and E behaved in a similar manner to each other at all temperatures as seen in Figure 4-19 and Figure 4-20. For both surfactants, even though the apparent viscosity declined with temperature, there was not any real change in the transition foam quality. The value of fg^* remained above 0.85 for all cases but did not show any consistent increasing or decreasing

trend. It can be said that their performance, with respect to the max. μ_{app} , declined with temperature; matching with the general rule where a hydrophobic chain of 12 to 16 carbons yields the best foaming properties at room temperature [22] as compared to other temperatures. On the other hand, MRF curves collapsed together to closer values, showing a max. MRF at 180°C. N.B. Similar to Surfactant B, viscosity and surface tension changes are also important.

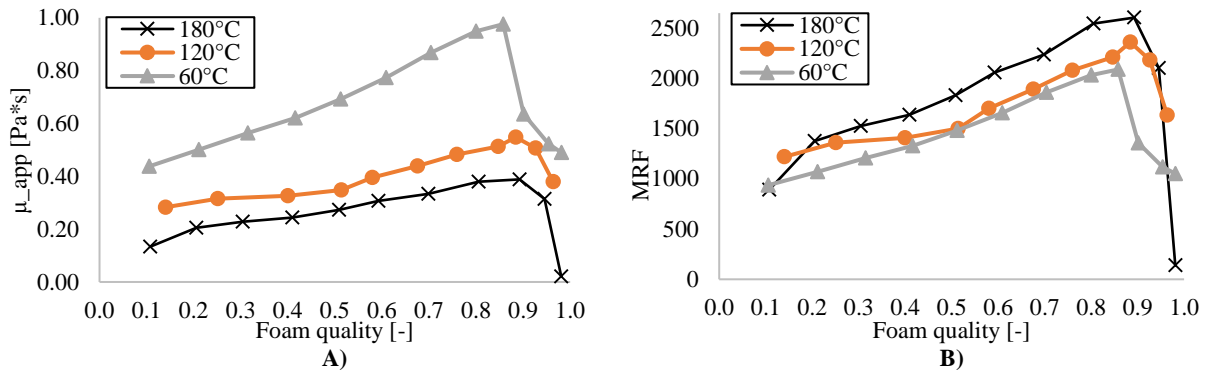


Figure 4-19. A) Apparent viscosity and B) MRF vs. foam quality at 60°C, 120°C and 180°C for Surfactant E

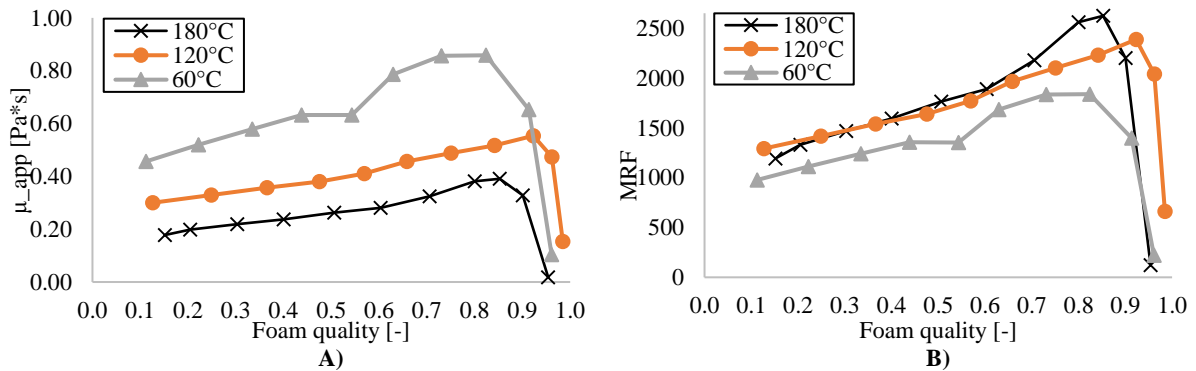


Figure 4-20. A) Apparent viscosity and B) MRF vs. foam quality at 60°C, 120°C and 180°C for Surfactant F

4.3.4 Comparison of surfactants at 60°C, 120°C & 180°C

At 60°C and 120°C, Surfactants E and F showed the strongest behavior in terms of the highest apparent viscosity values, and highest MRF values, as seen in as shown in Figure 4-21 and Figure 4-22. Also, Surfactant E and F had a value of f^* that was more shifted towards the right than Surfactant B and C, meaning a wider zone of low foam quality regime (with less coalescence).

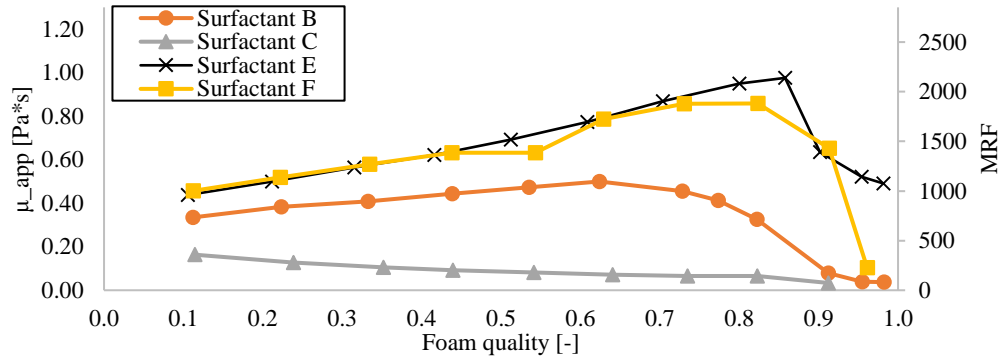


Figure 4-21. Apparent viscosity and MRF of surfactants at 60°C

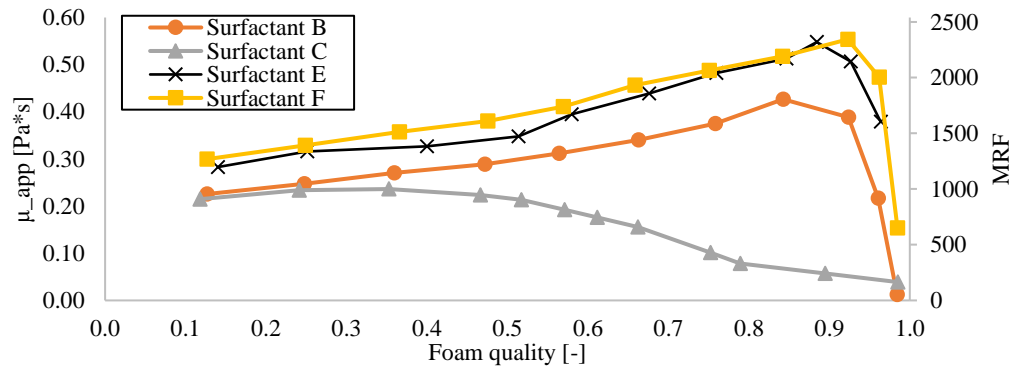


Figure 4-22. Apparent viscosity and MRF of surfactants at 120°C

At 180°C, the foam quality scan curves converged to a similar shape for all surfactants, where the low foam quality regime dominates as seen in Figure 4-23. The exception is Surfactant C, which showed slightly lower values of apparent viscosity and MRF. At this temperature, Surfactant B showed the highest apparent viscosity and MRF values.

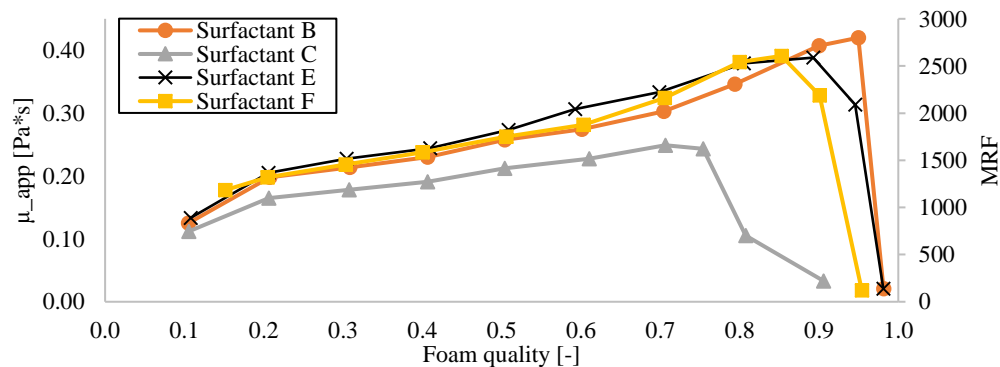


Figure 4-23. Apparent viscosity and MRF of surfactants at 180°C

4.3.5 Static Adsorption

The static adsorption tests were carried out to determine the effect of temperature on surfactant adsorption. It is clearly seen in Figure 4-24 that adsorption decreases with temperature. However, both Surfactant B and Surfactant C showed increases in adsorption at 90°C. This is

unexpected and is possibly due to readsorption of the surfactant onto clay particles during the cooling of the sample. Also, it is possible to notice that Surfactant B adsorption was the highest at both room temperature and 90°C.

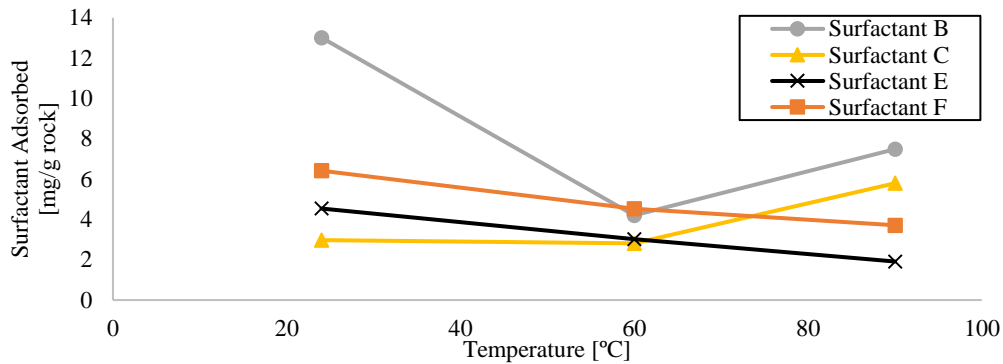


Figure 4-24. Surfactant adsorbed on core crushed stone with respect to temperature

Having fixed concentration, pH and salinity, the adsorption of surfactant decreases at higher temperatures as the force of interaction between the surfactant and the rock surface becomes weaker [58]. The consistent perturbations of the surfactant monolayers, caused by a higher kinetic energy, avoid the formation of any organized layer of surfactant molecules leading to a lower adsorption [58].

4.4 Dynamic Adsorption

As Surfactant B showed good foamability properties and excellent thermal stability, a dynamic adsorption test was carried out for this surfactant. Considering that the vertical dotted lines in Figure 4-25 represent the breakthrough of surfactant and tracer, a delay of 0.105 PV in the Surfactant B breakthrough can be measured. This corresponds to 0.059 mg/g rock of Surfactant B adsorbed to the Bentheimer sandstone.

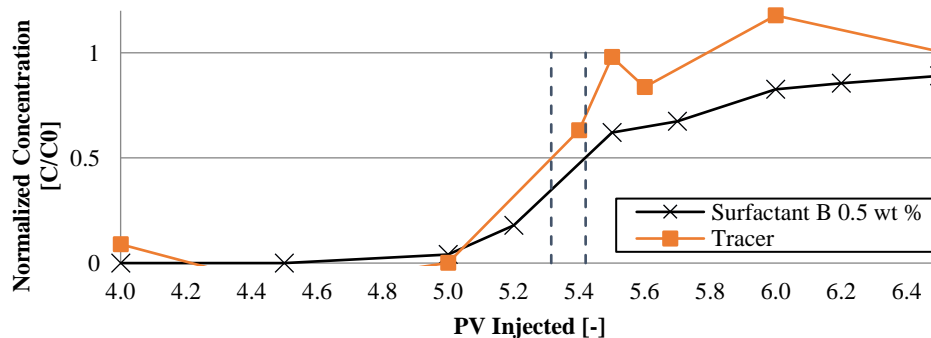


Figure 4-25. Dynamic adsorption of surfactant B in Bentheimer sandstone core at 120°C

4.5 Critical Micelle Concentration

As mentioned in Chapter 3, the CMC could only be measured for Surfactant A and B. At higher concentrations, above the CMC, the measured surface tension quickly stabilized to a value close to 30 mN/m, as measured using the Du Noüy-Padday method (i.e. static surface tension). In contrast, at lower concentrations below the CMC, it took up to 4 hours for the reading to stabilize to a constant value. For these concentrations, where the uncertainty was higher, the Wilhelmy method (i.e. dynamic surface tension) was also used, as shown in Figure 4-26 and Figure 4-27.

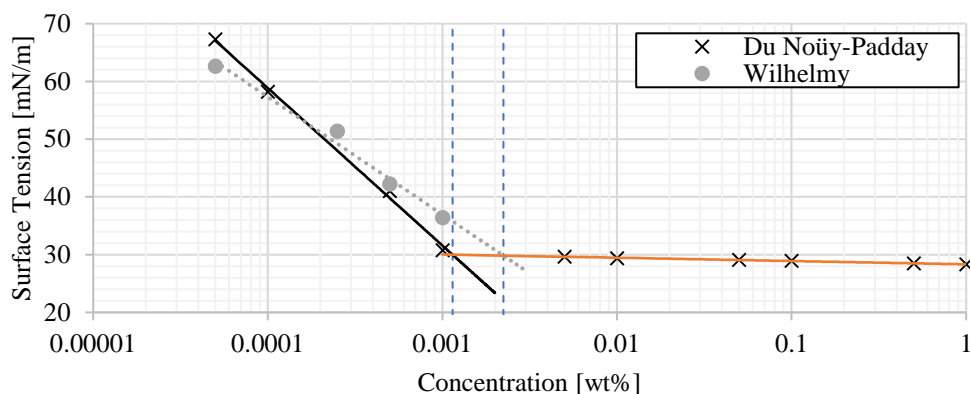


Figure 4-26. Surfactant A surface tension variation with concentration at 23°C

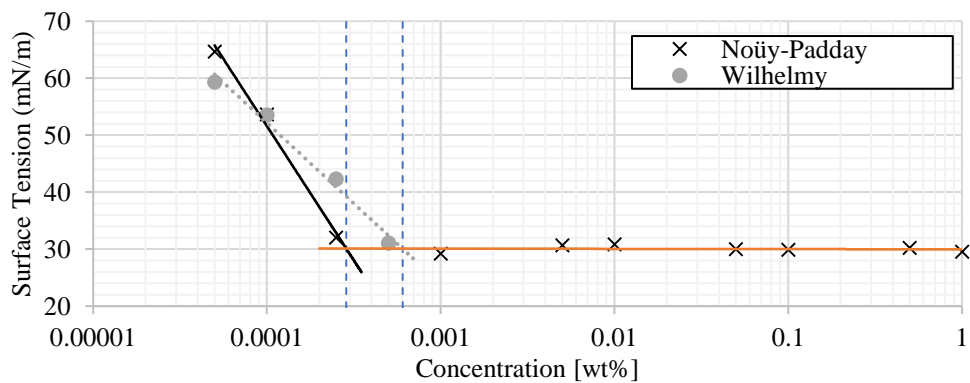


Figure 4-27. Surfactant B surface tension variation with concentration at 23°C

For concentrations of 5 ppm (0.0005 wt%) and higher, the surface tension stabilized to a constant value as seen in Figure 4-28 A. In contrast, for concentrations lower than 5 ppm, the surface tension did not stabilize to a constant value, instead, it decreased steadily. It is suggested that this linear decrease is due to evaporation from the small sample causing an increase in the surfactant concentration with a resultant reduction in the surface tension. For these concentrations, the surface tension was chosen at the point where the curve starts declining linearly as indicated in Figure 4-28 B.

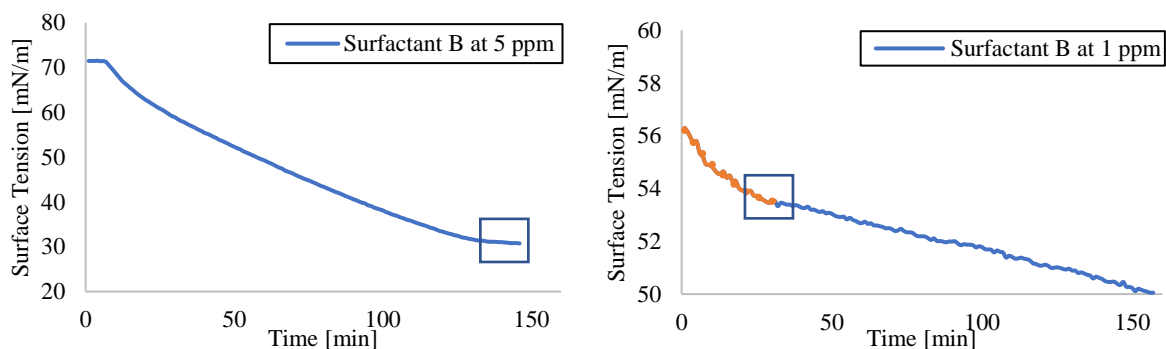


Figure 4-28. Dynamic surface tension (Wilhelmy method) for Surfactant B A) at 5 ppm tending to a constant value (squared) and B) at 1 ppm not tending to a constant value after 155 min. The transition to the linear decrease and recorded surface tension is indicated.

Even though the value of the CMC differed from one method to another by almost a factor of two, the CMC values remained within the same order or magnitude as seen in Table 4-3. It should be noted that the samples were in this case only 3 ml; therefore, they were more sensitive to external factors such as dust pollution or evaporation of some of the water (as discussed previously). The lower solubility of both surfactants at room temperature could also have influenced the results.

Table 4-3. CMC of Surfactants A and B by Du Noüy-Padday and Wilhelmy methods

| | CMC [ppm] | |
|--------------|----------------|----------|
| | Du Noüy-Padday | Wilhelmy |
| Surfactant A | 11.44 | 22.37 |
| Surfactant B | 2.86 | 6.04 |

It has previously been found that the CMC of a surfactant decreases with the length of the hydrophobic tail [59]. However, Surfactant A, which has a longer tail than Surfactant B (Table 3.1), had a lower measured CMC. Another factor related to the CMC is the position of the surfactant hydrophilic head. In previous experiments [60], the CMC increased when the sulfonate head move toward a more central position of the surfactant molecule. As it was shown in Table 3.1, the head of Surfactant A is not located in the outermost of the molecule.

5 Exergy Analysis Methodology

5.1 Overview

An exergy analysis will be carried out to assess the overall performance of the EOR methods of Water Alternating Gas (WAG) and Surfactant Alternating Gas (SAG). For the exergy analysis the Exergy Recovery Factor (ExRF) defined in Chapter 2, Equation (11), will be calculated over time. For this purpose, the system and boundaries must be defined first. Then, the exergy invested, and exergy gained will be calculated according to the methodology below.

5.1. System definition and boundaries

The system proposed for WAG and SAG is illustrated in Figure 5-1. It includes both the main facilities and the equipment required to obtain the injection gas, transport it to the field, inject it into the reservoir, separate the produced fluids and recirculate gas to reinject it into the reservoir. It also includes and treating and injection of water.

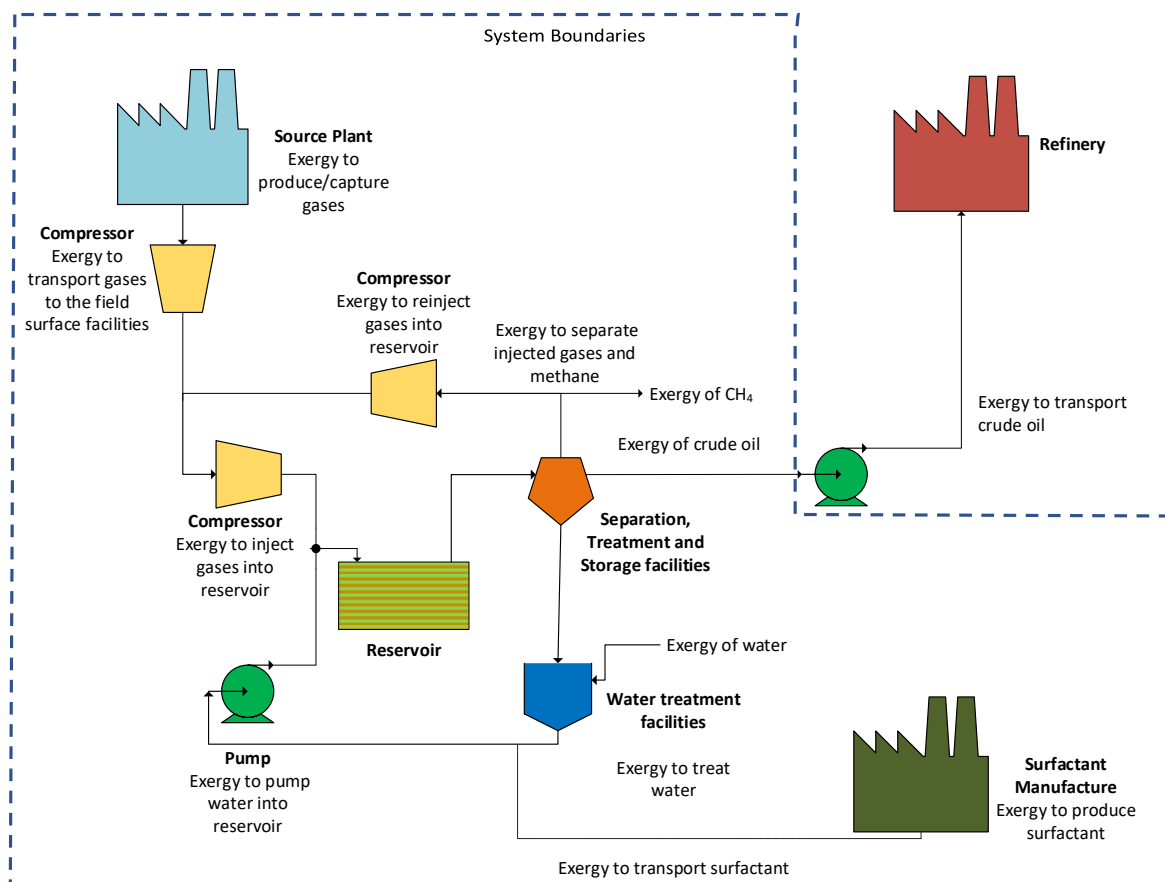


Figure 5-1. Schematic Diagram of gas and water injection system for WAG and SAG

5.1. Exergy Invested

The exergy invested; in this case, is the exergy required to produce a certain amount of hydrocarbons. According to the system defined in Figure 5-1, the exergy invested is composed by the following elements:

5.1.1 Exergy of Gas Capture

The exergy of gas capture is the exergy necessary to obtain the gases required for injection. The gases chosen for this study are listed below:

A. Flue gas

It is the product of the combustion of hydrocarbons or coal in a power plant. The composition of flue gas contains mainly N_2 , CO_2 and H_2O , and with traces of Ar, CO, O_2 , SO_2 , NO_3 and NO_2 . However, for this study, the composition of dried flue gas is assumed to be 88% of N_2 and 12% CO_2 [61]. A value of $Ex_{capture} = 0$ is used since it does not require any purification.

B. Carbon Dioxide (CO_2)

It is commonly obtained from flue gas. It is separated from N_2 and other traces by chemical absorption in an aqueous solution of mono-ethanol-amine (MEA); today's predominant carbon capture technology. For this process, an average value of $Ex_{capture} = 4000 \text{ kJ/kg } CO_2$ is used [3].

C. Nitrogen (N_2)

A cryogenic plant, which distills air at very low temperatures, is currently the most used technique to produce and N_2 with a very high degree of purity on an industrial scale [63]. A cryogenic air separation unit first compresses feed air and removes moisture, CO_2 , and other hydrocarbon pollutants. Then, the cleaned air is cooled to very low temperatures in heat exchangers. Finally, the cooled air is fed to distillation units where O_2 and N_2 are separated. For this process, a practical value of $Ex_{capture} = 1525 \text{ kJ/kg } N_2$ [63] is considered.

D. Methane (CH₄)

The methane source is the hydrocarbon gas produced from the reservoir. However, it is frequently not enough to fulfill the flow rate required for injection as the reservoir is being depleted. Therefore, additional CH₄ must be brought from other places near the field. However, in this analysis is assumed that the hydrocarbon gas produced is 100% CH₄, and, as there is any separation process involved, a value of $Ex_{capture} = 0$ is taken. However, methane is valuable fuel with a chemical exergy value of 54.1 MJ/kg

The exergy values for capture are shown in in Table 5-1. These values were found in literature.

Table 5-1. Exergy values for gas capture

| Gas | CO ₂ | Flue Gas | N ₂ | CH ₄ |
|-------------------------------|-----------------|----------|----------------|-----------------|
| Exergy of capture [kJ/kg gas] | 4000 | 0 | 1525 | 0 |

5.1.2 Exergy of Compression and Recompression

The exergy of compression includes two steps. The first step is the exergy required to transport the gas from its source to the oil field by means of an initial compression. The second step is the exergy required to compress the gas from the surface to the required pressure of injection to the reservoir. On the other hand, the exergy of recompression is the exergy required to compress the separated gases for reinjection.

The values of the exergy of compression and recompression need to be calculated. For this reason, the following assumptions are made:

- DWSIM, a chemical process simulator [64], was used to simulate the compression of the different gases described in Section 5.1.1. Within DWSIM, the Peng Robinson equations of state were selected to calculate the properties of the gases.
- The compression is isentropic, i.e. $S_1=S_2$, which means that there is no transfer of energy or matter with the surroundings.

- The compression is carried out in multiple stages. This allows for cooling to occur between the stages, which saves work in the compression process. To save on equipment costs, it is desirable to use as few stages of compression as possible [65].
- As a practical rule, the compression ratio (P_2/P_1) is limited by a preference to keep the outlet temperature below 149°C. This minimizes the possibility of ignition of lubricants, as well as limiting the power requirement, which goes up as outlet temperature goes up [65].
- To calculate the theoretical exergy of compression, the following equation is used by DWSIM, for each stage of compression:

$$\widehat{Ex}_{comp} = \widehat{W} = \widehat{H}_2 - \widehat{H}_1 = \left(\frac{k}{k-1}\right) \left(\frac{z_1+z_2}{2}\right) RT_1 \left[\left(\frac{P_2}{P_1}\right)^{\frac{k-1}{k}} - 1 \right] \quad (16)$$

Where:

\widehat{W} = specific work [J/kg]

\widehat{H}_1 = specific inlet enthalpy [kJ/kg]

\widehat{H}_2 = specific outlet enthalpy [kJ/kg]

P_1 = inlet pressure [bar]

P_2 = outlet pressure [bar]

T_1 = Inlet temperature [K]

R = gas constant [J /K mol]

$k = C_p/C_v$ = ratio of heat capacities at constant pressure and constant volume.

z = compressibilities at the inlet and outlet

5.1.2.1 First Step of Compression

The cryogenic plants required to produce N₂ are usually placed in situ. The sources required to provide CH₄ are assumed to be available near the field too. Hence, the exergy of compression to transport of N₂ and CH₄ is negligible.

On the other hand, the CO₂ and flue gas are produced in a power plant and it is assumed that this is located 300 km away from the oil field. Both gases are compressed before being sent to the oil field through a pipeline, as illustrated in the schematic diagram in Figure 5-2.

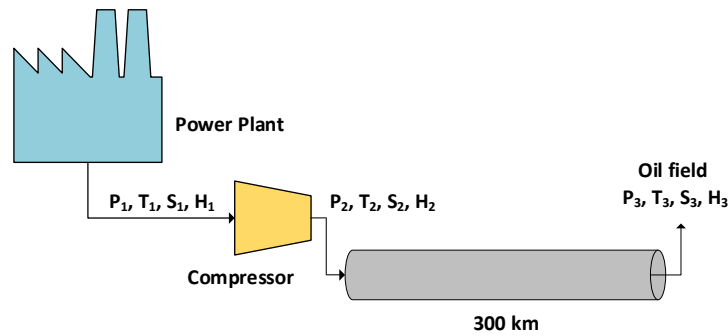


Figure 5-2. First step of compression - CO₂ and flue gas transport through a pipeline. P=pressure, T=temperature, S= entropy, H= enthalpy

For transport through a pipeline, the following recommendations are followed:

- For efficiency, CO₂ is typically compressed above 74 bar, because it is easier to transport a dense liquid than a gas [66]. The industry preference is to operate the pipeline at higher than 103 bar at the inlet to maintain CO₂ in the supercritical phase as shown in Figure 5-3.

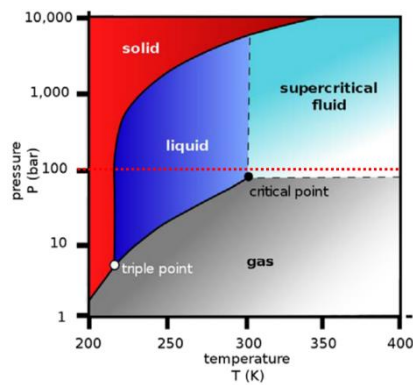


Figure 5-3. Thermodynamic phase diagram of CO₂

- DWSIM calculates the pressure drop across the pipeline with the Fanning correlation, which considers the friction loss effect on hydrostatic pressure difference ΔP . The formula is as follows:

$$\Delta P = \frac{2f_{tp}v_m^2\rho_{NS}L}{144g_cD}$$

(17)

where:

- f_{tp} = friction factor
- v_m = mixture velocity
- ρ_{NS} = fluid density
- L = pipeline length
- g_c = gravity constant
- D = pipeline diameter

- The pipeline diameter, D , is assumed to be 57 cm to be consistent with other CO₂ transport projects where the designed capacity is between 10 and 28 million ton per year [66].

In Table 5-2, the parameters of the first step of compression and the corresponding exergy values are shown. Efficiencies of the compressor, power plant and electrical driver are applied [62] to both steps of compression, and recompression.

Table 5-2. Exergy values for gas compression. First stage

| | CO ₂ | Flue Gas |
|--|-----------------|----------|
| P_1 (bar) | 1 | 1 |
| P_2 (bar) | 105.5 | 107 |
| Theoretical Exergy of Compression 1 st step [kJ/kg gas] | 295.7 | 865.8 |
| η_{comp} | 0.7 | 0.7 |
| $\eta_{\text{powerplant}}$ | 0.4 | 0.4 |
| η_{driver} | 0.9 | 0.9 |
| Practical Exergy of Compression 1 st step [kJ/kg gas] | 1173.4 | 3435.7 |

5.1.2.2 Second Step of Compression

The second stage of compression is illustrated in Figure 5-4. All immiscible gases are injected at 200 bar. Additionally, CO₂ is also injected at 400 bar to allow miscibility with oil. It is assumed that N₂ and CH₄ are delivered to the oil field at 20 bar. In

Table 5-3, the parameters of the second step of compression and the corresponding exergy values are shown.

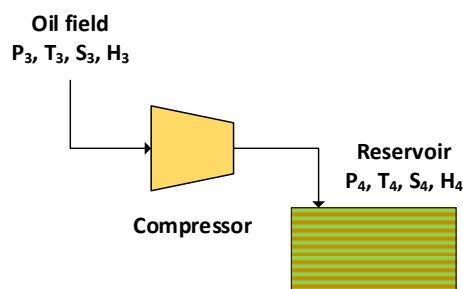


Figure 5-4. Second step of compression – Injection into the reservoir

Table 5-3. Exergy values for compression. Second stage

| | CO ₂ (miscible) | CO ₂ (immisc.) | Flue Gas | N ₂ | CH ₄ |
|--|----------------------------|---------------------------|----------|----------------|-----------------|
| P ₂ (bar) | 105 | 105 | 105 | 20 | 20 |
| P ₃ (bar) | 400 | 200 | 400 | 200 | 200 |
| Theoretical Exergy of Compression 2 nd step [kJ/kg gas] | 68.3 | 30.8 | 268.4 | 247.1 | 389.2 |
| η _{comp} | 0.7 | 0.7 | 0.7 | 0.7 | 0.7 |
| η _{powerplant} | 0.4 | 0.4 | 0.4 | 0.4 | 0.4 |
| η _{driver} | 0.9 | 0.9 | 0.9 | 0.9 | - |
| Practical Exergy of Compression 2 nd step [kJ/kg gas] | 271 | 122.2 | 1065.1 | 980.6 | 1544.4 |

5.1.2.3 Recompression of recirculating gases

For recompression, it is assumed that the separation of the gases is carried out at atmospheric pressure. Therefore, the gases are recompressed from atmospheric pressure, P₅, to the pressure of the gases at the surface of the oil field before injection, P₃, as shown in Figure 5-5. In Table 5-4, the parameters of recompression and the corresponding exergy values are shown.

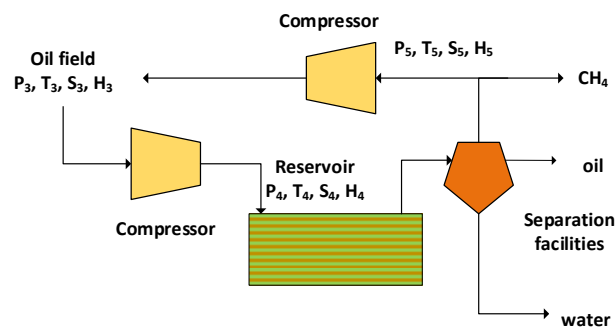


Figure 5-5. Recompression of gases to be reinjected into the reservoir
 Table 5-4. Exergy values for gas recompression

| | CO ₂ | Flue Gas | N ₂ | CH ₄ |
|---|-----------------|----------|----------------|-----------------|
| P ₅ (bar) | 1 | 1 | 1 | 1 |
| P ₃ (bar) | 105 | 105 | 20 | 20 |
| Theoretical Exergy of recompression [kJ/kg gas] | 295 | 865 | 378.9 | 539.9 |

| | | | | |
|---|------|------|--------|--------|
| η_{comp} | 0.7 | 0.7 | 0.7 | 0.7 |
| $\eta_{\text{powerplant}}$ | 0.4 | 0.4 | 0.4 | 0.4 |
| η_{driver} | 0.9 | 0.9 | 0.9 | 0.9 |
| Practical Exergy of recompression [kJ/kg gas] | 1170 | 3432 | 1503.6 | 2142.4 |

5.1.3 Exergy of Separation

The separation of the produced fluids is assumed to be carried out in a horizontal three-phase separator as shown in Figure 5-6, where adequate residence time is provided to allow the fluids to separate by gravity. Thus, there is no exergy consumed in this step.

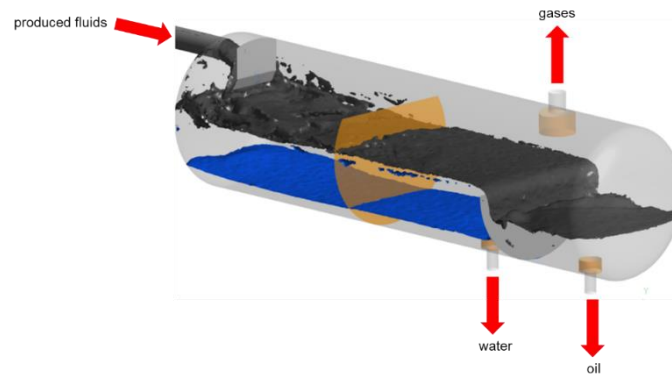


Figure 5-6. Gravity fluid separator [68]

The exergy to separate the injected gases from CH_4 are listed in Table 5-5. It is assumed that separating CO_2 from CH_4 would require the same exergy as separating CO_2 from flue gas. Also, it is assumed that separation of flue gas and CH_4 , would require 88% of the exergy of separation of N_2 from CH_4 , through cryogenic distillation, and 12% of the exergy of CO_2 separation by through chemical absorption.

Table 5-5. Exergy values for injected gas – CH_4 separation

| | CO_2 | Flue Gas | N_2 | CH_4 |
|----------------------------------|---------------------------------|-----------------|--------------------------------|---------------------------------|
| Exergy of separation [kJ/kg gas] | 4000 | 2460 | 2250 | - |

5.1.4 Exergy of Water Treatment and Injection

The water treatment facilities are schematically illustrated in Figure 5-7. The water injected is either produced water or water from other sources that comes from the surroundings. Thus, the exergy required to transport water is negligible. The water then requires treatment to meet

certain specifications for injection. Physically, removal of suspended solids or precipitates to avoid the plugging of the reservoir rock.

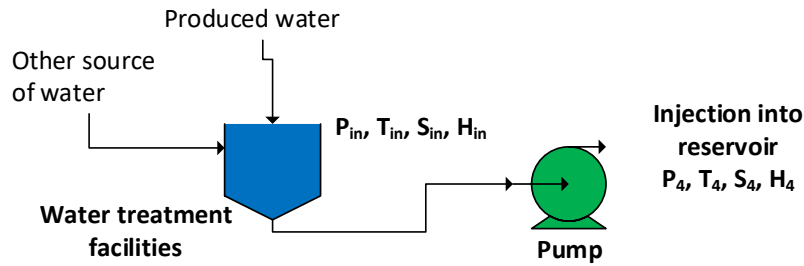


Figure 5-7. Schematic diagram of water treatment and injection facilities

The chemical treatment of water is normally more complex. However, as the composition of produced water varies widely and can include dissolved and dispersed oil components, dissolved minerals, production chemicals and dissolved gases. Consequently, the technology and exergy associated for treatment varies widely as well. For the current analysis, the Nanofiltration, which is specifically efficient for feed water containing TDS ranging from 500 to 25000 mg/l. The corresponding exergy average value for this technology is $Ex_{water\ treatment} = 20\text{ kJ/kg } H_2O$ [69]. This value does not vary with the gas being injected.

A centrifugal pump is then used to inject water into the reservoir. The theoretical exergy of pumping can be calculated using the next equation:

$$Ex_{pump} = \dot{W}_s = q\Delta P \tag{18}$$

where:

\dot{W}_s = shaft work [kJ/s]

q = volumetric flow rate of water [m³/s]

ΔP = Difference pressure between the bottom hole pressure (BHP) and the reservoir pressure [Pa]. For this study it is assumed to be $\Delta P = 50\text{ bar}$.

The parameters for the injection of water are listed in Table 5-6.

Table 5-6. Exergy of water injection

| | CO₂, Flue gas, N₂ and CH₄ |
|--|---|
| ΔP (bar) | 50 |
| Theoretical Exergy of Water Injection [kJ/kg water] | 4.9 |
| η_{comp} | 0.7 |
| $\eta_{\text{powerplant}}$ | 0.4 |
| η_{driver} | 0.9 |
| Practical Exergy of Water Injection [kJ/kg gas] | 19.4 |

5.1.5 Exergy of Surfactant

To calculate the exergy of the surfactant required to produce the foam for SAG, the manufacturing and transport (to the oil field) of the surfactant are considered in this study. The exergy to manufacture the surfactant is 60.9 MJ/kg_{surfactant} [70]. This value belongs to the manufacturing of a linear alkylbenzene sulfonate in Germany. This surfactant is similar to the surfactant that best performed in the experiments mentioned in Chapter 4.

The exergy to transport the surfactant from the manufacturing place to the oil field is 453 kJ/kg_{surfactant}. To calculate this value, it is assumed that the surfactant was transported 12960 km on a chemical tanker at a velocity of 37 km/hr. The exergy of a chemical tanker with a capacity of 47000 ton is 212.7 TJ/year [71].

Therefore, the $Ex_{\text{surfactant}} = 61.4 \text{ MJ/kg}$ for all cases.

5.2. Exergy Gained

The exergy gained refers to the total chemical exergy of the hydrocarbons extracted from the reservoir. For this study, the chemical exergy of gas is 51.98 MJ/kg and for oil is 45.60 MJ/kg. To calculate the quantity of hydrocarbons recovered for each different gas, a 2-D, 3-phase (water, gas, and oil) compositional model previously developed in Shell's Modular Reservoir Simulator (MoReS) was used [72]. This model simulates the transport of surfactant and foam,

and the mobility of the gas phase is modified by a series of parameters such as the maximum foam strength, surfactant concentration, water saturation and the effect of oil on foam.

Also, this model uses the Corey correlations to calculate the relative permeabilities of water and gas; the relative permeability of oil is calculated by linear isomers. The 3-phase relative permeability parameters for water, oil, and gas are listed in Table 5-7.

Table 5-7. Three-phase relative permeability parameters to water, oil, and gas (no foam).

| Water-Oil Relative Permeability Parameters | | |
|---|-------------|-------------|
| Parameter | Symbol | Value |
| Connate water saturation | S_{wc} | 0.10 |
| Residual oil saturation to water | S_{orw} | 0.40 |
| End-point relative permeability to water | k_{rw}^o | 0.22 |
| End-point relative permeability to oil | k_{row}^o | 0.20 |
| Corey exponent for water | n_w | 4.00 |
| Corey exponent for oil with respect to water | n_{ow} | 2.00 |
| Oil-Gas Relative Permeability Parameters | | |
| Parameter | Symbol | Value |
| Residual gas saturation | S_{gr} | 0.05 |
| Residual oil saturation to gas | S_{org} | 0.01 |
| End-point relative permeability to gas | k_{rg}^o | 1.00 |
| End-point relative permeability to oil | k_{rog}^o | k_{row}^o |
| Corey exponent for gas | n_g | 1.70 |
| Corey exponent for oil with respect to gas | n_{og} | 1.30 |

The model reservoir for this study is a section of 2000 ft in length, 200 ft in height and 100 ft in thickness with one injector well and one producer well as shown in Figure 5-8. 2D reservoir model representation. The initial reservoir condition is set at 100°C, with 400 bar for CO₂ miscible; and 200 bar for N₂, CH₄, flue gas, and immiscible CO₂.

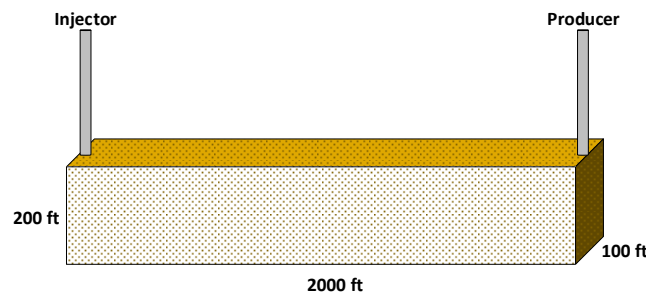


Figure 5-8. 2D reservoir model representation.

The reservoir is initially at an oil saturation $S_{oil} = 0.90$ and water saturation of $S_w = 0.10$ with a hypothetical black oil with an API gravity of 45° and a viscosity of 0.4 cP at 100°C and 100 bar. The reservoir is homogeneous with a porosity of $\phi = 0.25$ and a permeability of $k = 500$

mD. To calculate the mass of the produced fluids from the volumes obtained in the simulations, the oil density at standard conditions was assumed to be $\rho_{oil} = 800 \text{ kg/m}^3$ and the density of water $\rho_{water} = 1000 \text{ kg/m}^3$. The density of the different gases was calculated using DWSIM. Finally, the reservoir is flooded with 1 PV of water before WAG and SAG enhanced oil recovery techniques are applied. The injection flow rate calculated for this study was $141.6 \text{ m}^3/\text{day}$, this in order to keep an interstitial velocity $v_i = 1 \text{ ft/day}$. It is assumed that a 20% of the gas injected is lost. So, the total amount of gases injected is 20% higher.

5.3. Calculation of Exergy Recovery Factor

For each gas, the exergy recovery factor is calculated as follows:

$$Ex_{RF} = 1 - \frac{(Ex_{gas}^{capture} + Ex_{gas}^{comp} + Ex_{gas}^{recomp} + Ex_{gas}^{sep} + Ex_{water}^{treat} + Ex_{water}^{pump} + Ex_{surf})}{Ex_{oil}^{ch} + Ex_{CH_4}^{ch}} \quad (19)$$

where:

$Ex_{gas}^{capture}$ = Exergy of capture [MJ]

Ex_{gas}^{comp} = Exergy of transport [MJ]

Ex_{gas}^{sep} = Exergy of separation [MJ]

Ex_{gas}^{recomp} = Exergy of recompression [MJ]

Ex_{water}^{inj} = Exergy of water injection [MJ]

Ex_{water}^{treat} = Exergy of water treatment [MJ]

Ex_{surf} = Exergy of surfactant (manufacturing and transport) [MJ]

Ex_{oil}^{chem} = Chemical exergy of oil [MJ]

$Ex_{CH_4}^{chem}$ = Chemical exergy of CH_4 [MJ]

6 Exergy Analysis Results

6.1 Oil Recovery Factor

As mentioned in the previous chapter, 1 PV of water was injected into the reservoir before WAG or SAG injection continued for another PV, as shown in Figure 6-1.

| | Cycle | Slug ratio |
|------------------|-------|------------|
| Water (or Surf.) | 1 | 1:2 |
| Gas | | |
| Water (or Surf.) | 2 | 1:2 |
| Gas | | |
| Water (or Surf.) | 3 | 1:3 |
| Gas | | |

A)

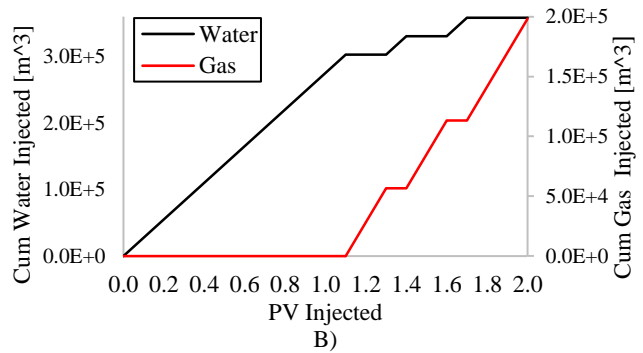


Figure 6-1. A) WAG and SAG slug ratio. B) Cumulative water and gas injected

The oil recovery factor for each gas is illustrated in Figure 6-. The recovery of oil, after 1 PV of water flooding, improved marginally with immiscible WAG injection of N₂/CH₄ and flue gas. However, there is a higher increment of the oil recovery with both miscible and immiscible injection of CO₂.

In contrast, with SAG, the oil recovery increased significantly for all gases. However, the ratio between the recovery of SAG and WAG is greater for N₂, CH₄ and flue gas than for CO₂, (immiscible and miscible) as shown in Table 6-1.

Table 6-1. Oil Recovery with WAG and SAG for all gases

| | Oil Recovery WAG | Oil Recovery SAG | Ratio [SAG/WAG] |
|---------------------------------|---------------------|---------------------|--------------------|
| N ₂ /CH ₄ | 0.35 | 0.64 | 1.83 |
| Flue gas | 0.35 | 0.64 | 1.83 |
| Misc. CO ₂ | 0.43 | 0.76 | 1.76 |
| Immisc. CO ₂ | 0.61 | 0.76 | 1.24 |

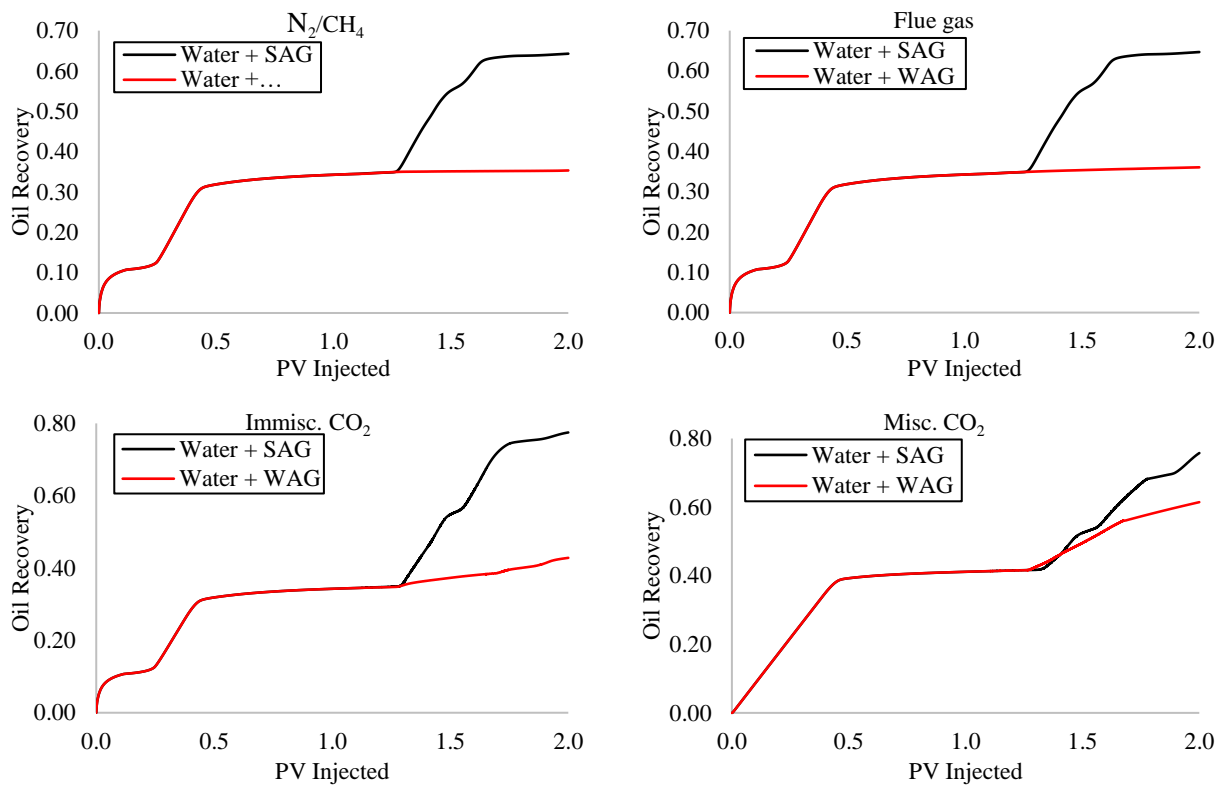


Figure 6-2. Oil Recovery Factor with waterflooding and SAG or WAG

Figure 6- and Figure 6- display 2-D saturation profiles of a lateral view of the reservoir, between the injector and the producer well. For WAG injection (Figure 6-), it is shown that N_2/CH_4 and flue gas swept a smaller portion of the reservoir than immiscible CO_2 . In contrast, miscible CO_2 covered a bigger portion of the reservoir than the other gases. The reason the reservoir was not completely swept is due to gravity override. It is shown that water being heavier than oil, slumped towards the bottom of the reservoir while the gas, being lighter, rose to the top.

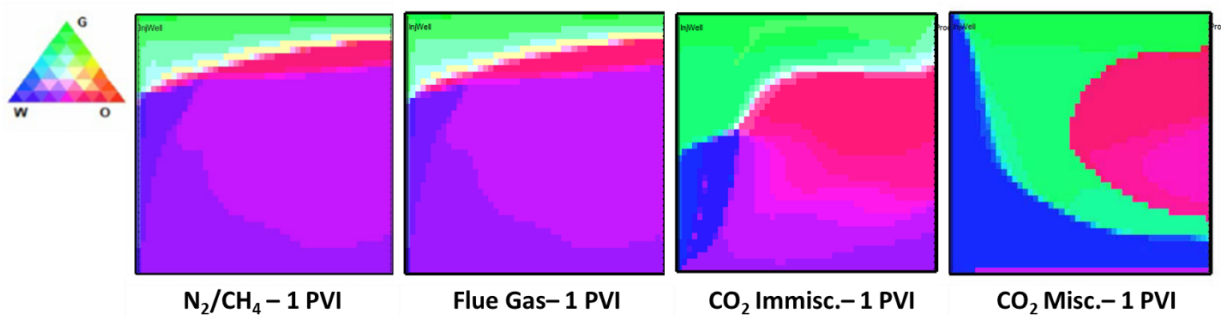


Figure 6-3. 2-D saturation profiles after 1 PVI of WAG slug

For SAG injection (Figure 6-), a piston-like displacement is observed for all cases. This effect is caused by a reduction of the gas mobility, which led to an improvement in the sweep efficiency.

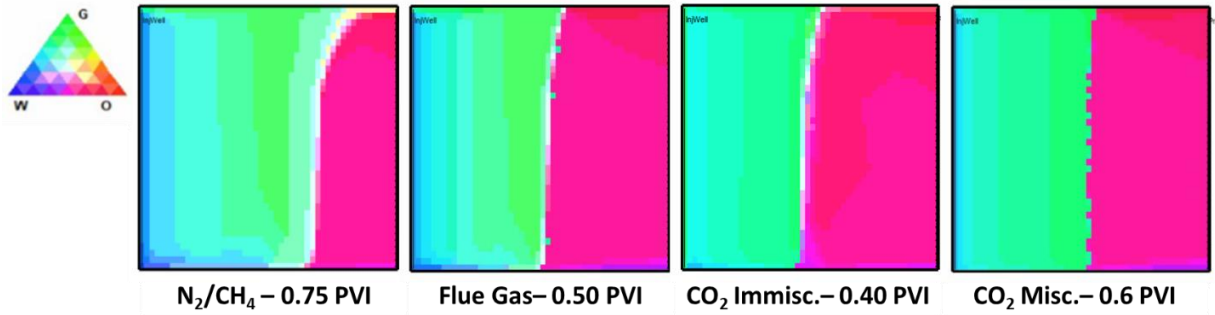
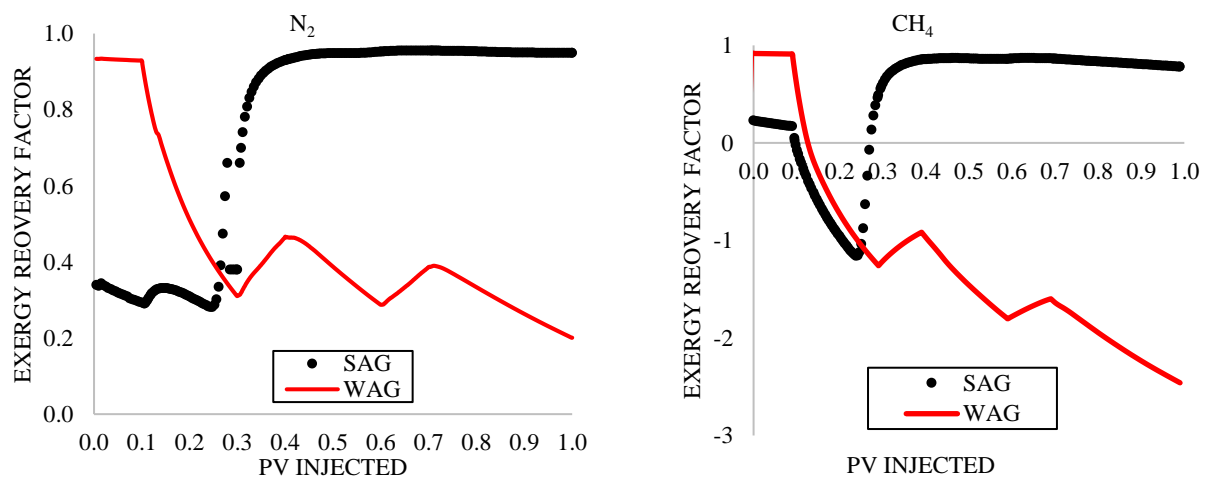


Figure 6-4. 2-D saturation profiles at different PVI of SAG slug

6.2 Exergy Recovery Factor – Base Scenario

The Exergy Recovery Factor (Ex_{RF}) was calculated only for WAG and SAG and not for waterflooding. A positive Ex_{RF} means that the energy gained is higher than the energy being invested. Therefore, a negative Ex_{RF} indicates that more input exergy is required than extracted. Also, the higher the Ex_{RF} (the maximum value is one), the more useful energy is available.

The Ex_{RF} of SAG and WAG with each gas is shown in Figure 6-1. At the beginning of the injection, the SAG Ex_{RF} is lower than the Ex_{RF} of WAG. This is because of the high ‘exergy cost’ of the surfactant that is being injected without having generated any foam. Then, the SAG Ex_{RF} increases and remains above the Ex_{RF} of WAG for the rest of the injection. This is because once the foam is generated and starts sweeping the oil, the oil recovery is boosted and so Ex_{RF} of SAG.



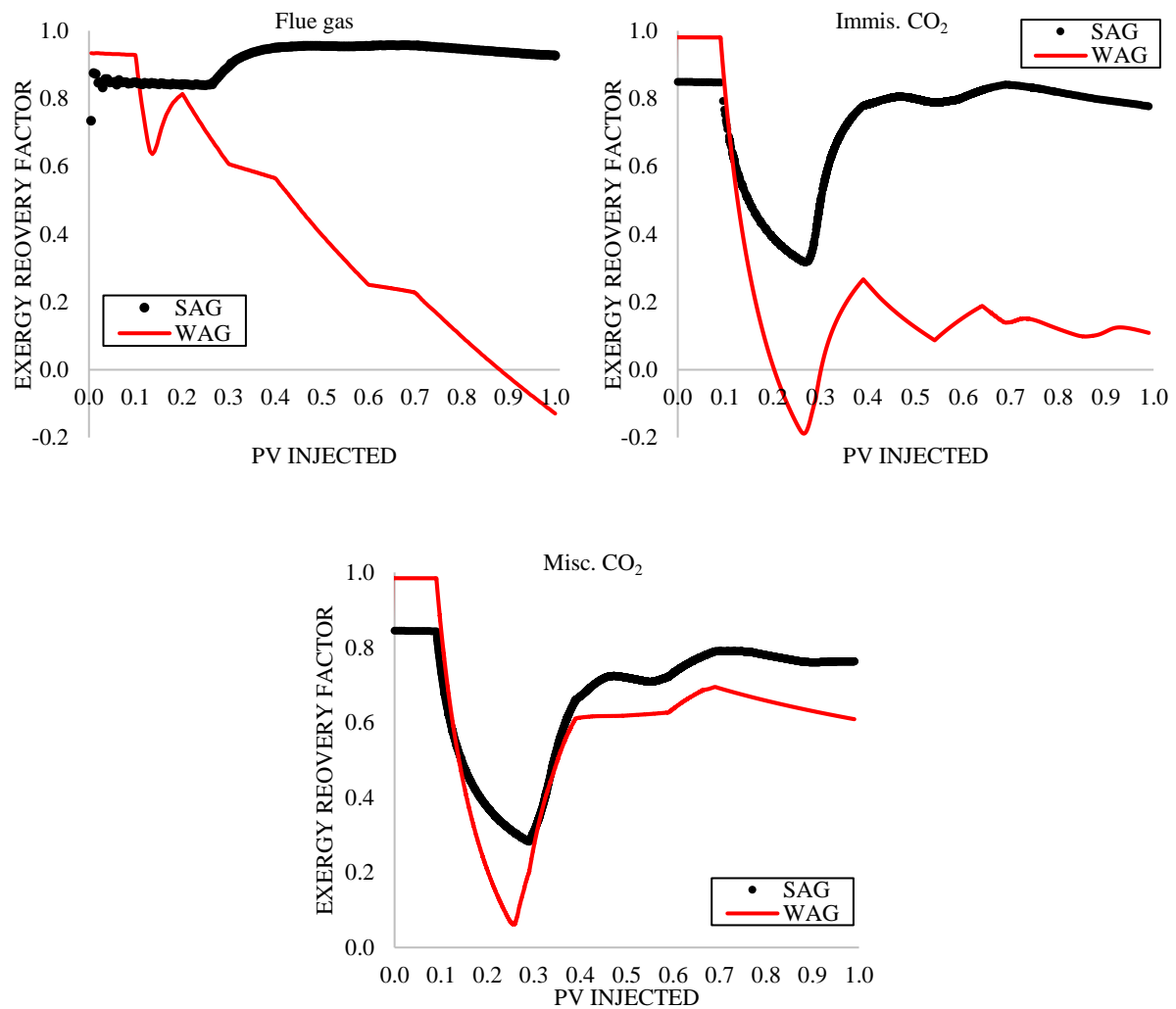


Figure 6-1. ExRF of SAG and WAG for all gases

6.3 Sensitivity Analysis

As mentioned in Chapter 2, one of the purposes of an exergy analysis is to determine the locations, types, and magnitude of losses of energy. For this reason, the sensitivity analysis is focused in finding alternatives to enhance the ExRF of WAG. In this regard, the variables to be changed are related to ‘operational decisions’ rather than the design of the process or the properties of the reservoir.

The low ExRF values of WAG with N₂, CH₄ and flue gas is because the exergy invested is comparable with the exergy gained. In contrast, the ExRF of WAG with CO₂ is higher because the exergy gained is higher than the exergy invested, as seen in Figure 6-2. Since the CH₄ injected has a higher chemical exergy than oil in the reservoir, the chemical exergy of the CH₄ is considered part of the exergy invested.

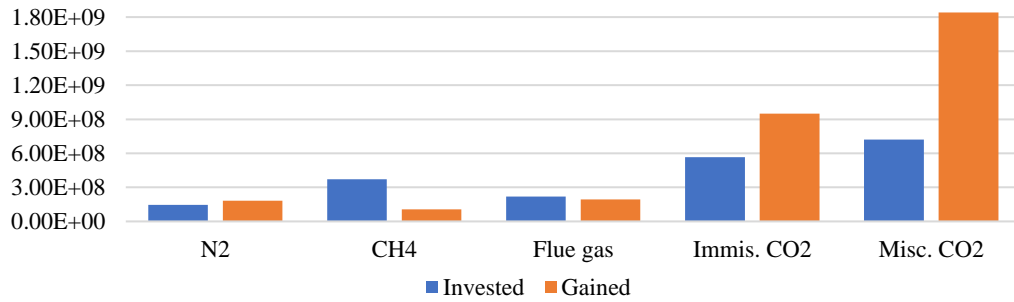


Figure 6-2. Exergy invested and gained for WAG – Base Scenario

The reason the exergy gained with WAG is lower for N₂, CH₄ and flue gas than CO₂ is because the oil recovery increased marginally, as shown in Section 6.1. On the other hand, a deeper analysis is required to know the reason the exergy invested is similar to the exergy gained. In Figure 6-3 (For CH₄, the chemical exergy of CH₄ is excluded from the pie charts), it is seen that the separation of the produced gases requires approximately 1/3 of exergy invested. It is one of the process that consumes most of the energy. Therefore, one option to reduce the amount of exergy invested is to reinject the produced gases without separating it.

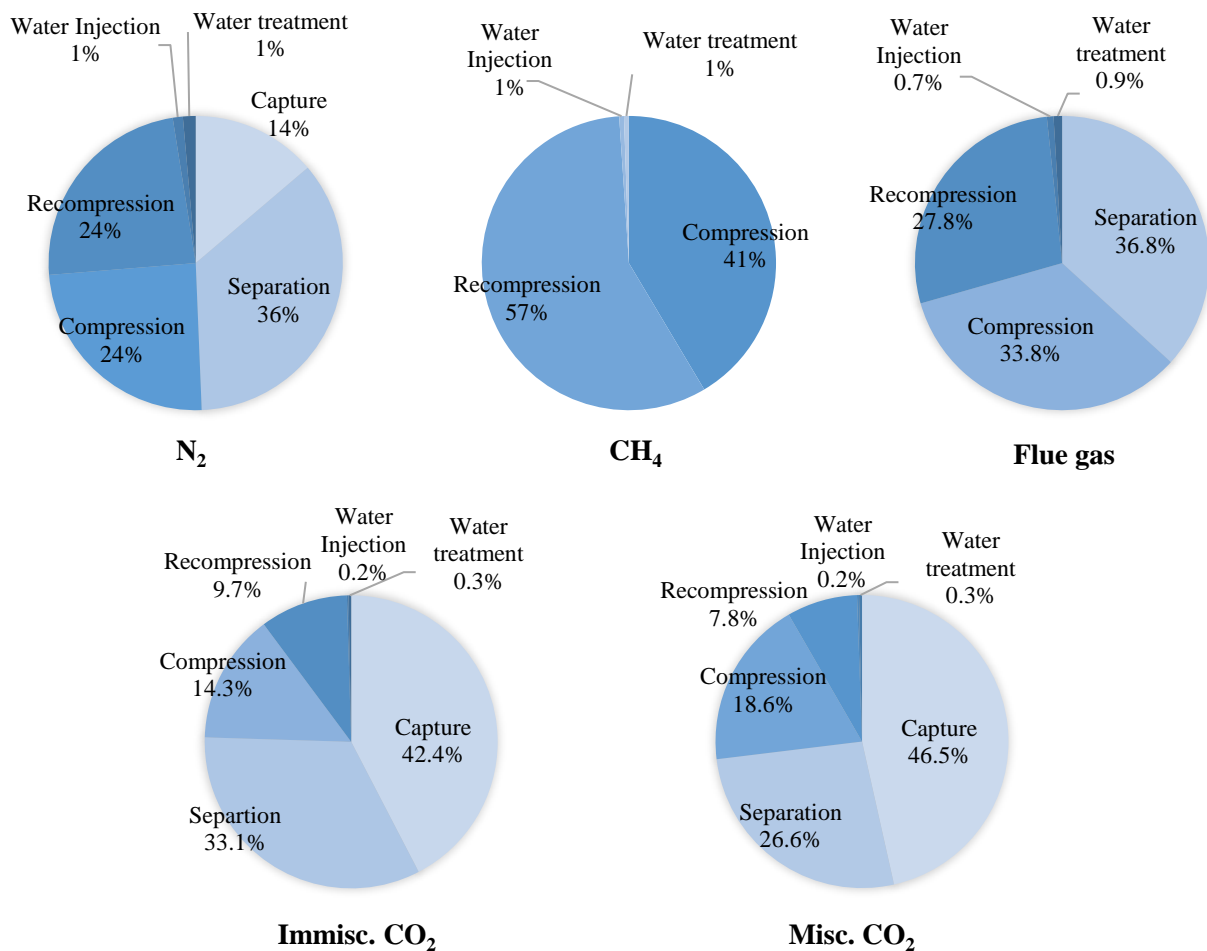
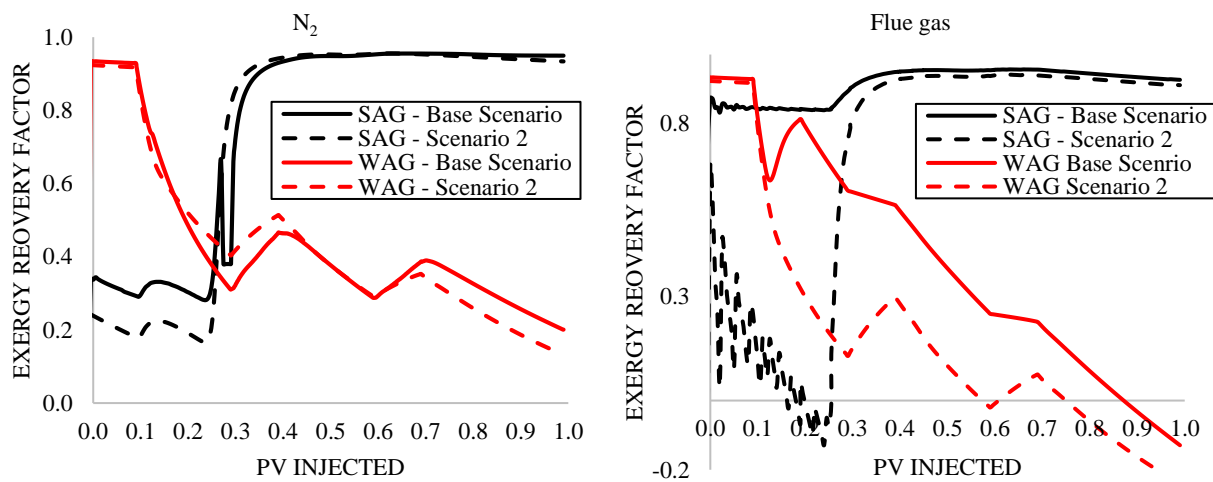


Figure 6-3. WAG energy invested

6.3.1 Scenario 2 – No Separation of Produced Gases

The separation of the produced gases serves to purify the natural gas and use it as a product with a high exergy content. Thus, shutting down the gas separation process, would cause the gas mixture to have a lower exergy content than pure CH_4 . This gas mixture might not be suitable to be used as fuel. Therefore, the produced gas mixture is recirculated to be reinjected into the reservoir. Recirculating the produced gas mixture would change the composition of the injection gas stream to N_2+CH_4 , flue gas+ CH_4 , or CO_2+CH_4 . It is assumed that despite having a different gas composition at the inlet, the oil recovery is not changed.

Removing the gas separation process was also done to SAG in order to compare the performance of WAG and SAG under the same conditions. In Figure 6-4, it is shown that the ExRF did not improve for any gas. Despite saving the exergy to separate the produced gases, the loss of the natural gas stream with high exergy content caused the ExRF to decrease. The decrease in the ExRF was higher for N_2 and flue gas than for CO_2 due to their lower oil recovery. The base scenario of WAG and SAG with CH_4 does not include any type of separation, and that all the produced gas is reinjected into the reservoir. Therefore, the ExRF of WAG and SAG with CH_4 does not change.



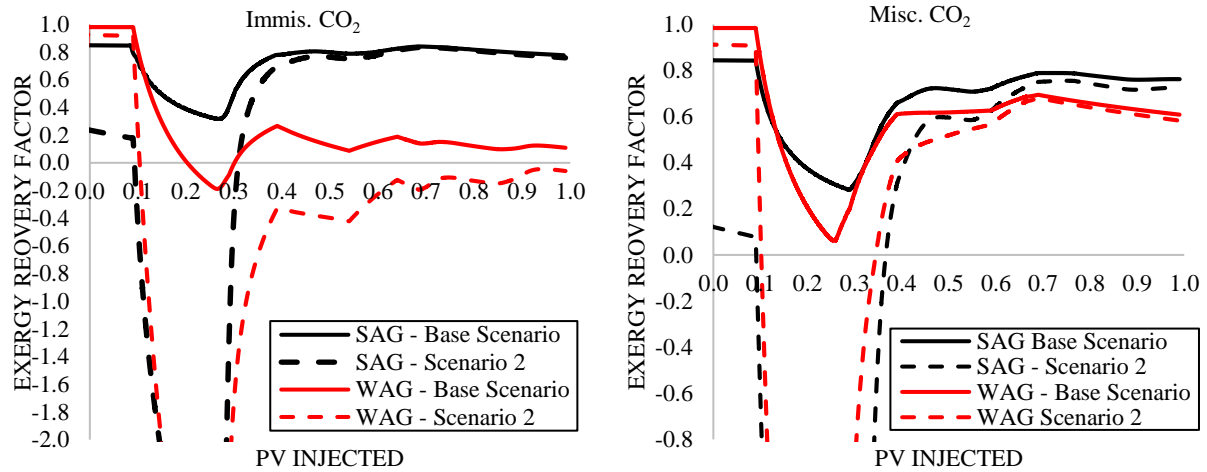


Figure 6-4.Scenario 2 - WAG and SAG ExRF without separation of produced gases

In Figure 6-4 it is seen how despite the exergy invested decreased, the exergy gained also decreased but in a higher proportion as compared with the base scenario (Figure 6-4)

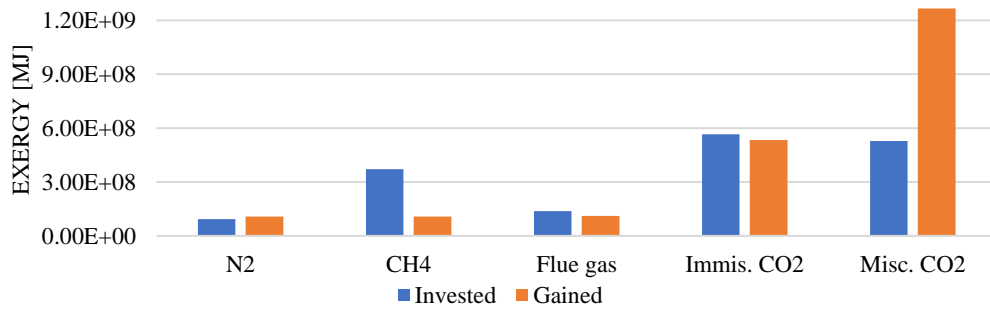
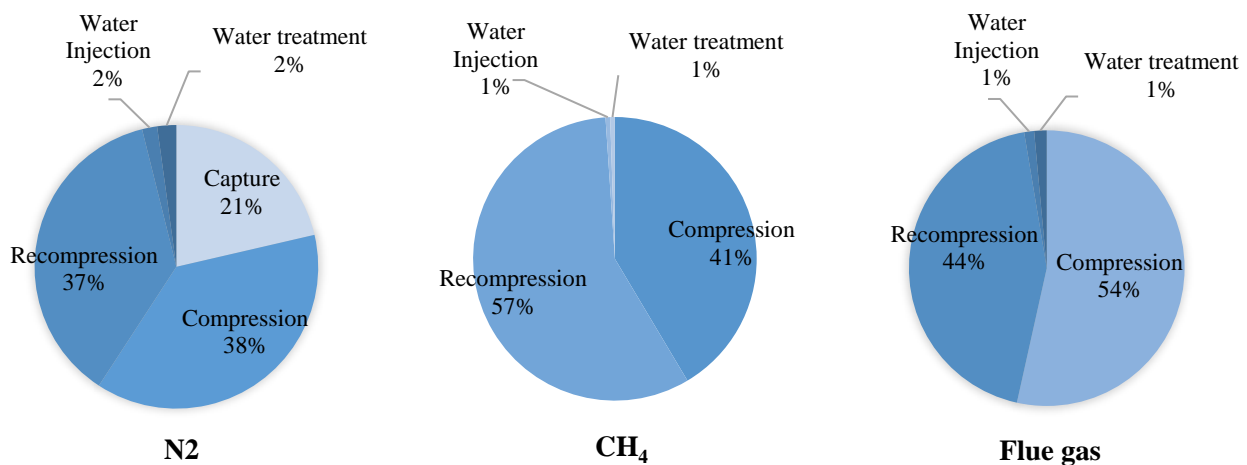


Figure 6-5. Exergy invested and gained for WAG – Scenario 2

In Figure 6-6, it is shown that capture of CO₂ are the processes that required most of the exergy investment; recompression also consumed a considerable amount of exergy. Although all the produced gases were recirculated, the same flow rate for injection was kept.



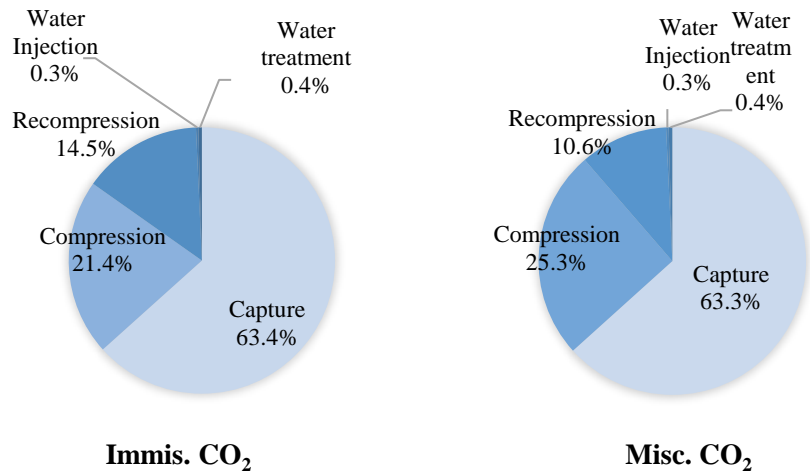
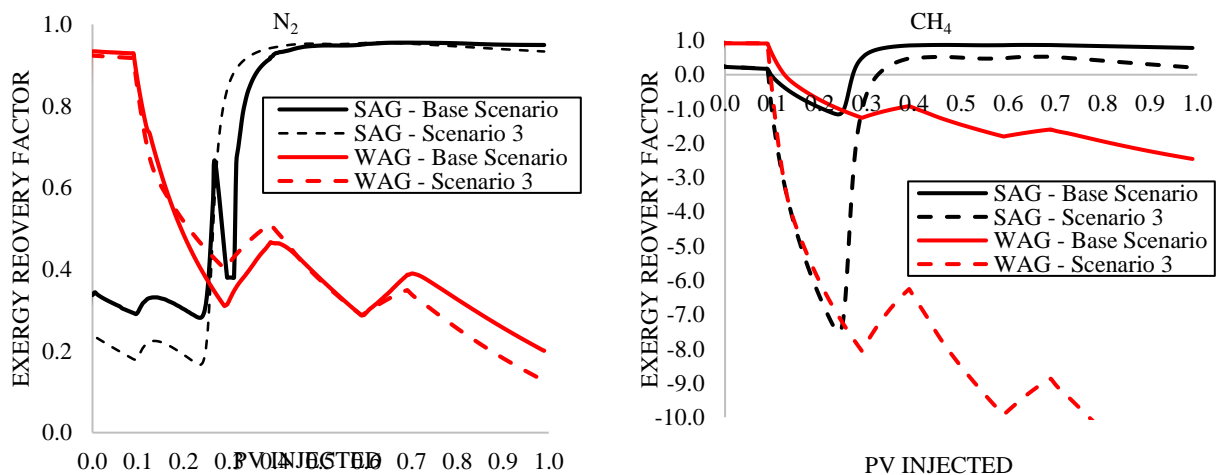


Figure 6-6. WAG energy invested – Scenario 2

6.3.2 Scenario 3– No Separation and no Recompression of Produced Gases

As removing the process of separation of the produced gases did not improve the ExRF for any gas for the reasons mentioned in Section 6.3.1, another option is to remove the process of recompression as it consumes a considerable amount of exergy for N₂, CH₄ and flue gas. This decision implies that all produced gases would be flared and vented to the atmosphere. Thus, less exergy is invested as the exergy of separation and the exergy of recompression are eliminated. Again, the natural gas stream with high exergy content would be lost and more exergy of capture would be required as there is not any recirculation stream.

As seen in Figure 6-7, the ExRF did not improved for any case. For CH₄, the negative impact was worse because of the chemical exergy contained in it, which was completely lost in this scenario because there was no recirculation of this gas.



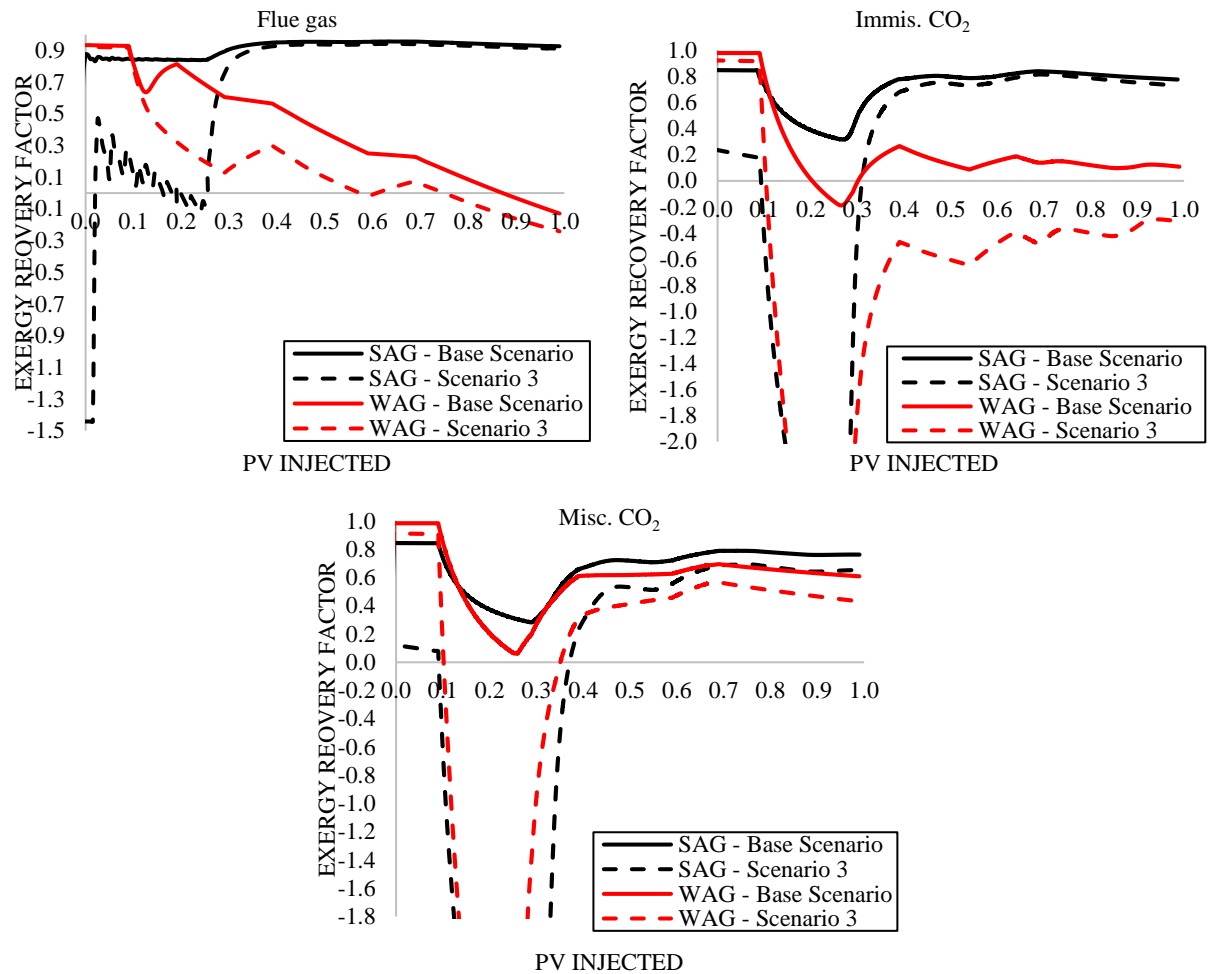


Figure 6-7. Scenario 3- WAG and SAG ExRF without separation and recirculation of produced gases

Despite removing two processes from the base scenario (separation and recompression). The ExRF did not increase because more exergy of capture was used to deliver the required gas flowrate to be injected, as there was not any recirculation stream that could provide some of this gas. For flue gas, although there is no exergy of capture, more exergy was required to transport the gas from the power plant, thus increasing the exergy of compression. Nonetheless, it has been shown in Scenario 2 that the ExRF is highly influenced by the exergy gained with CH₄.

In Figure 6-8 it is shown that the relationship between the exergy invested and gained of this scenario did not have a significant change with respect to Scenario 2, except for CH₄.

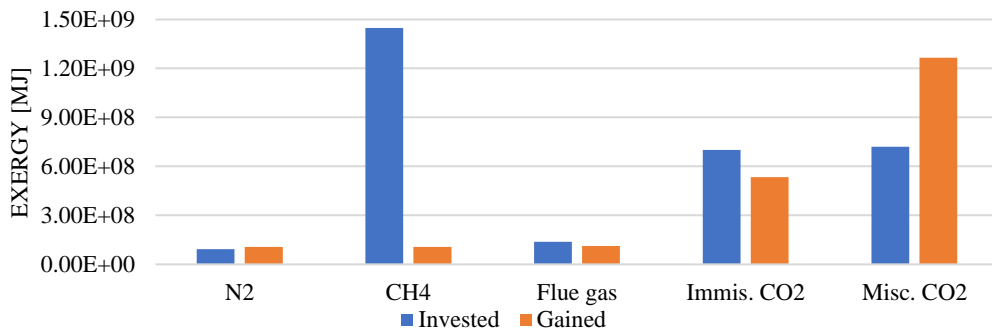


Figure 6-8. Exergy invested and gained for WAG – Scenario 3

In this scenario most of the exergy spent for N₂ and CO₂ is in capturing, as seen in Figure 6-9. On the other hand, for CH₄ and flue gas, most of exergy invested goes to compression. From an operational point of view, it is difficult to optimize furthermore any of the categories left in the exergy invested, unless changes are done to the design of the process.

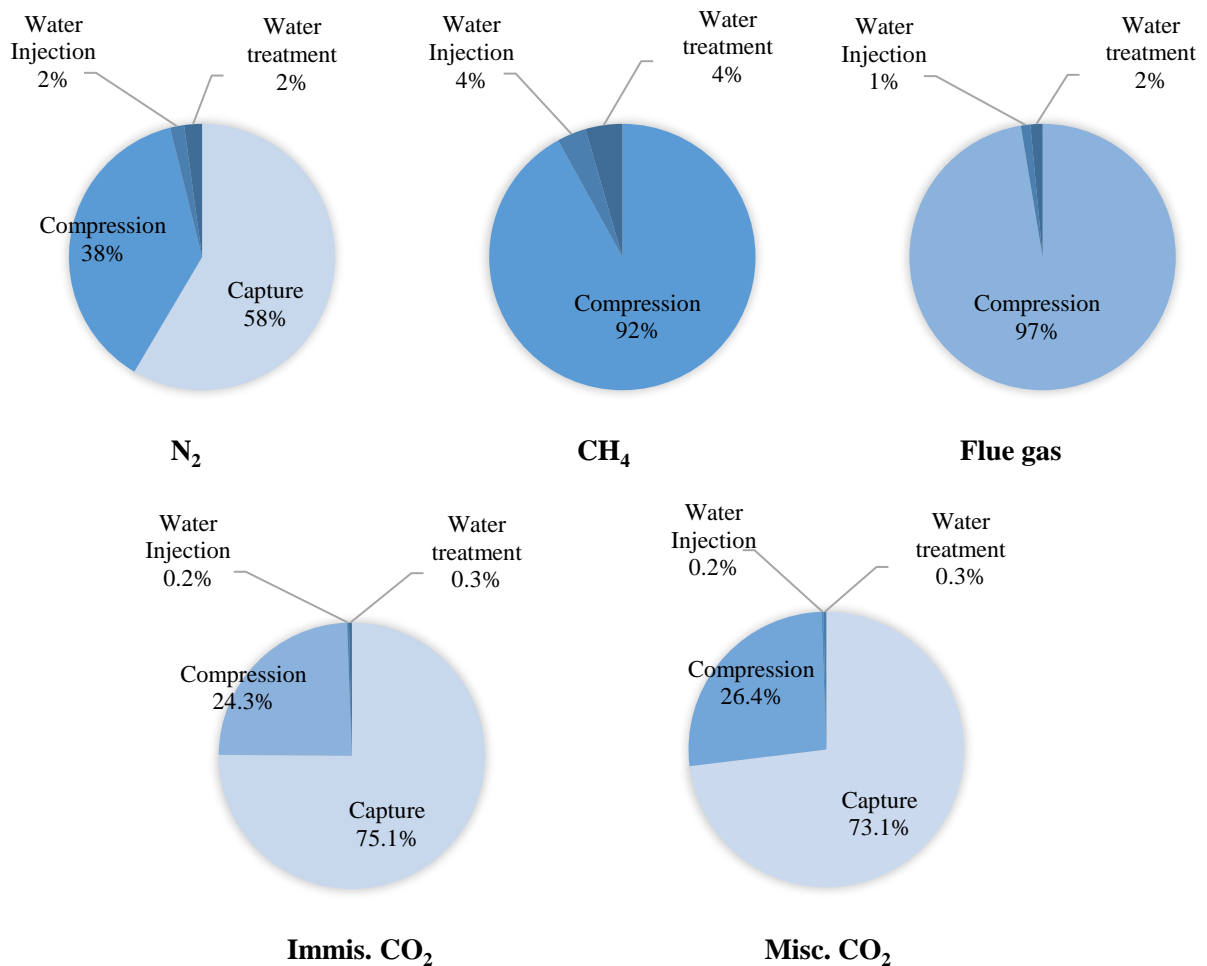
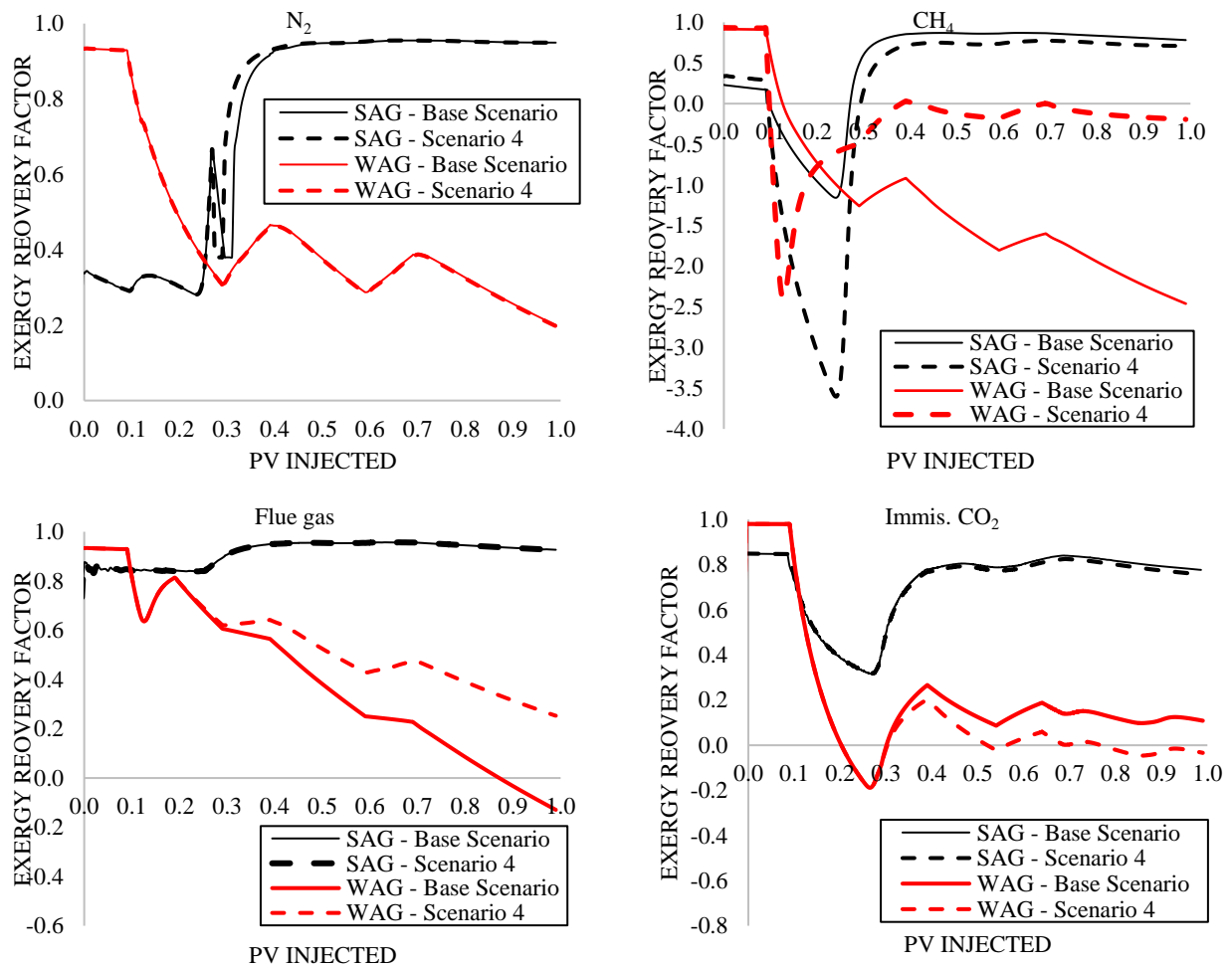


Figure 6-9. WAG energy invested – Scenario 3

6.3.3 Scenario 4– No Recompression of Produced Gases

To keep the exergy gained of the natural produced it is also necessary to keep the separation process. However, it is not necessary to keep the recompression process. Therefore, the next scenario considers no recirculation of produced N_2 , flue gas and CO_2 . This means that these gases would be vented to the atmosphere after being separating from the natural gas produced. In Figure it is shown that when compared to the base scenario, the ExRF of WAG with CH_4 , and flue gas improved, it remained almost the same with N_2 , but it did not improve with CO_2 . On the other hand, the ExRF of SAG with N_2 , CH_4 , and flue gas remained almost the same and with CO_2 , it did not improve.



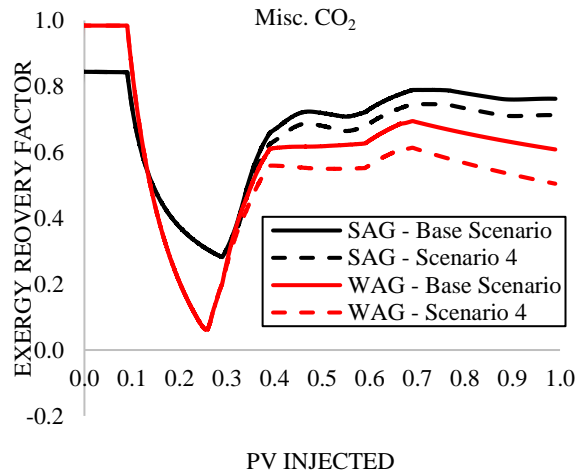


Figure 6-10. Scenario 4- WAG and SAG ExRF without separation and recirculation of produced gases

The ExRF of WAG with CH₄ improved because of the high amount of exergy gained with the natural gas stream, as shown in Figure 6-11. This stream was not recirculated in this scenario like in the previous ones.

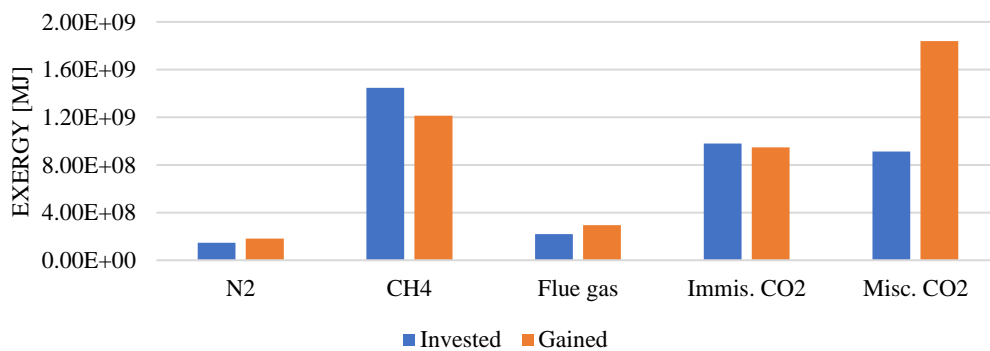


Figure 6-11. Exergy invested and gained for WAG – Scenario 4

The ExRF of WAG with CO₂ did not improve because of the higher specific exergy of capturing CO₂ compared to the specific exergy of recompressing CO₂, as shown Table 5-1 and Table 5-4. This means that capturing 1 kg CO₂ requires more exergy than recompressing 1 kg of CO₂. For this reason, recirculating part of the CO₂ produced is a better option than capturing new CO₂. In Figure 6-12, it is seen how the exergy of capturing N₂ and CO₂ keeps the highest share of the total exergy invested.

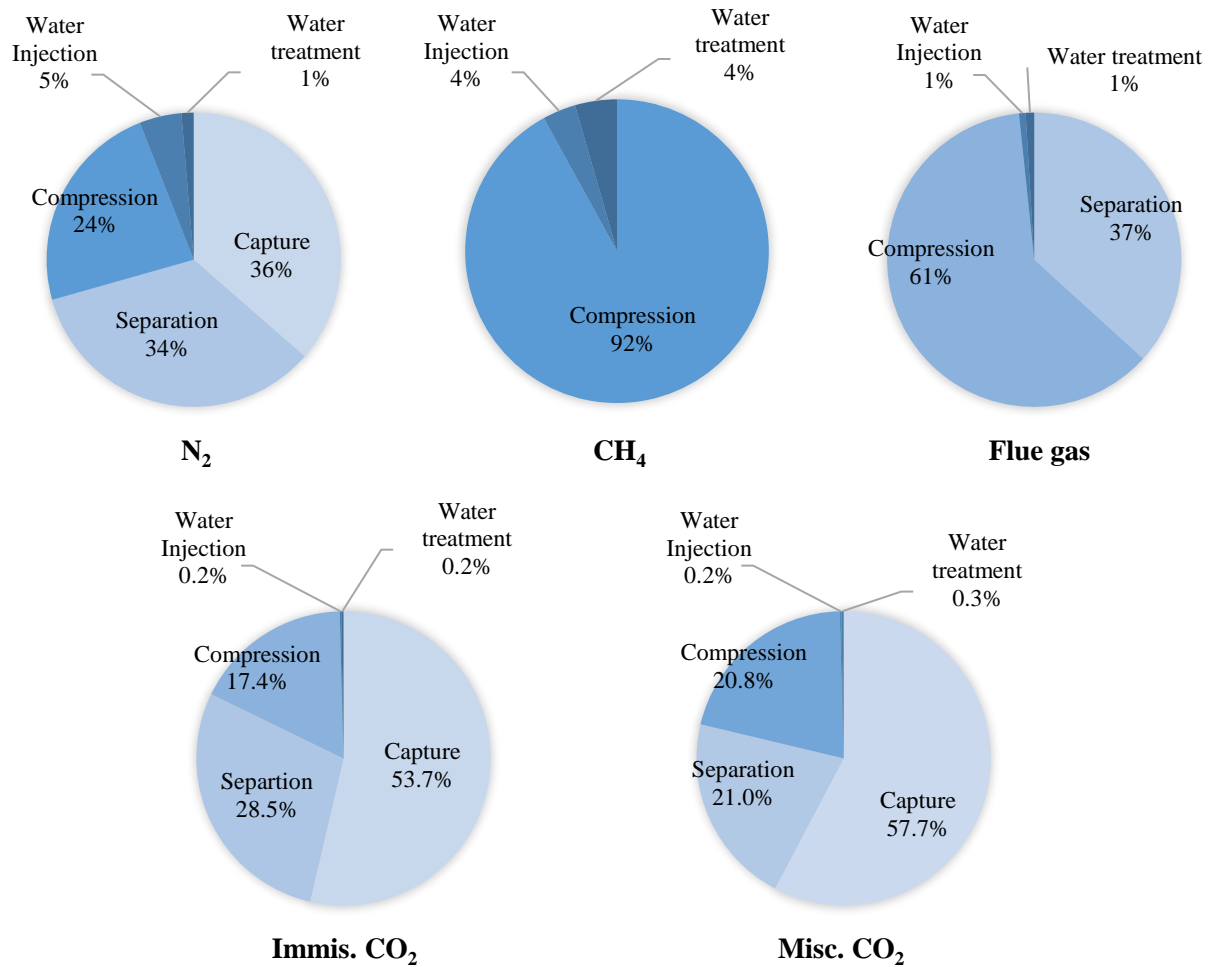


Figure 6-12. Share of energy invested for WAG – Scenario 4

6.3.4 Scenario 5– Changing the Surfactant Concentration

In the previous sections, it was shown that despite the changes applied to the system, the ExRF of SAG, for any gas, was not as affected as the ExRF of WAG. Specially, after 0.25 – 0.30 PV of injection, where the generated foam starts displacing enough oil causing the ExRF of SAG to increase at a high rate. As consequence, the exergy gained is much higher than the exergy invested as seen in Figure.

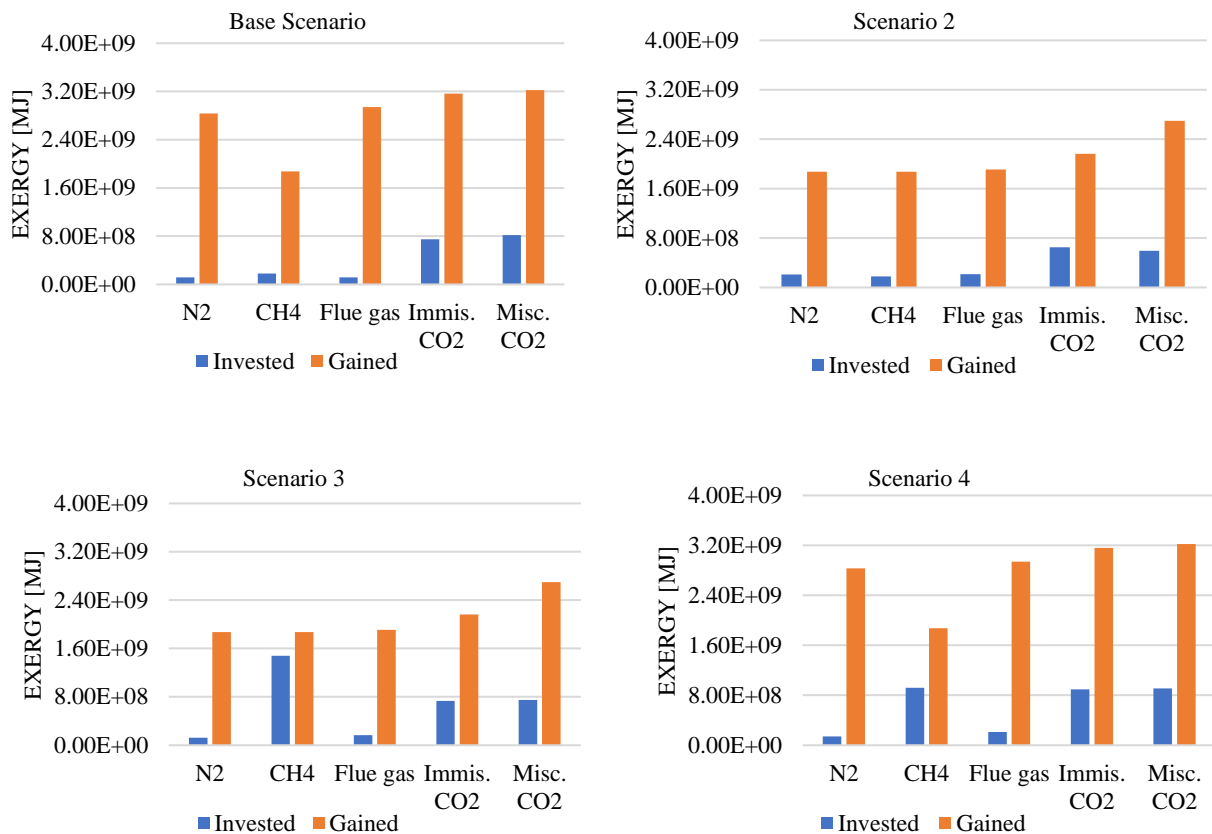
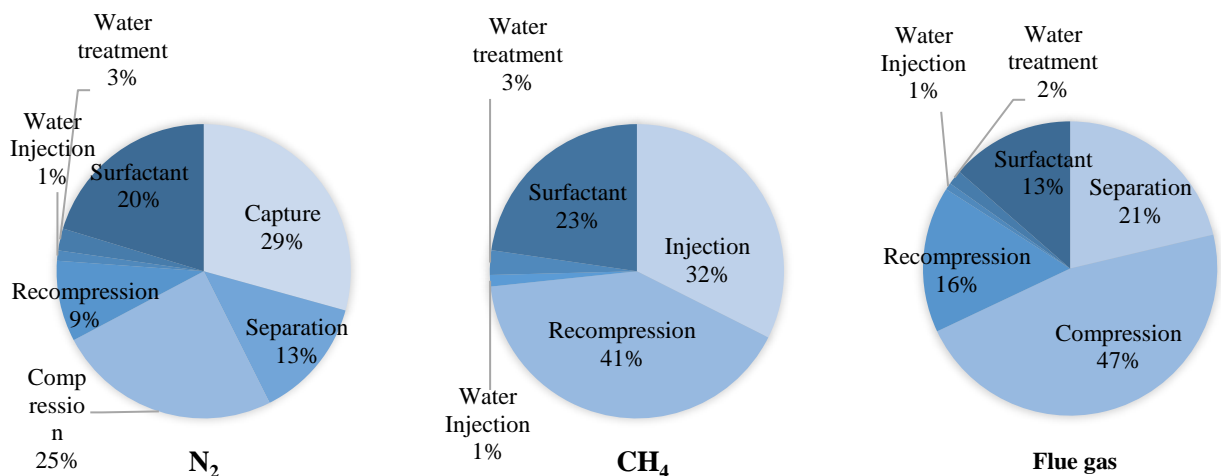


Figure 6-13. Exergy invested and gained for SAG – All scenarios

For the base case, the share of the exergy of the surfactant ranges from 3.6% to 23%, as seen in Figure 6-14. This range does not vary significantly in the other scenarios. Even though the exergy of surfactant is not as high as the exergy of capture or separation, the specific exergy of surfactant (61.4 MJ/kg) is the highest of all specific exergies considered in this study. Therefore, changing the concentration of surfactant by a small fraction would impact the ExRF of SAG.



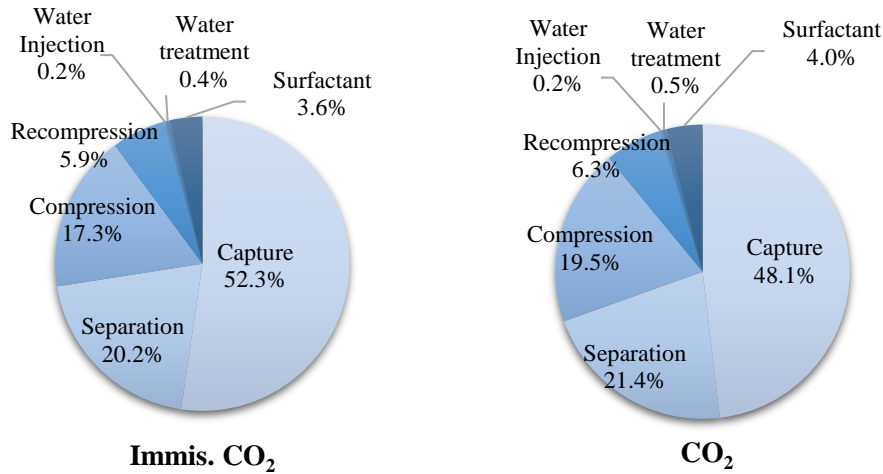
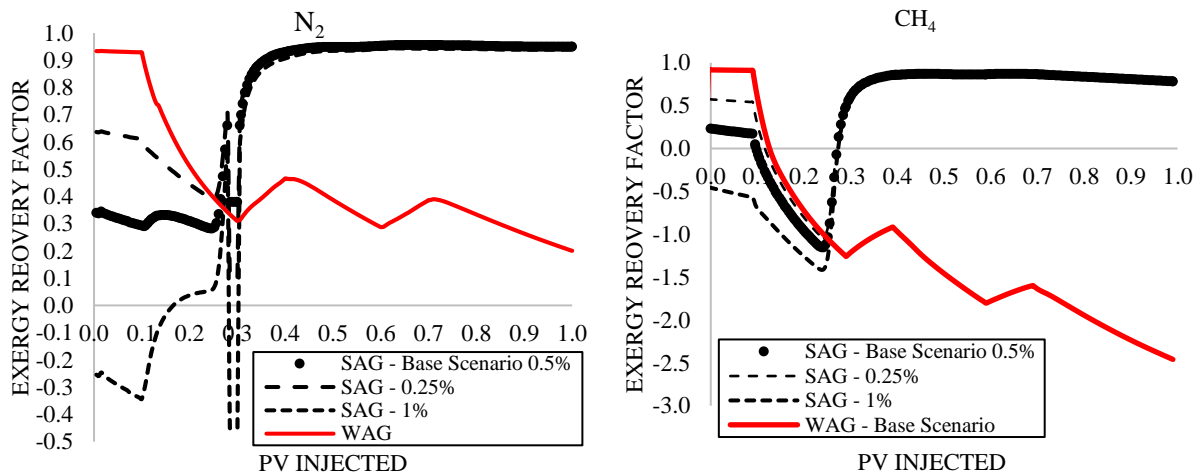


Figure 6-14. Share of energy invested for SAG – Scenario 1

The concentration of the surfactant in the base case is 0.5wt% The behaviour of the ExRF of SAG by changing the surfactant concentration to 0.25wt% and 1.0 wt% is shown in Figure Figure 6-15. It was assumed that the oil recovery did not changed with these surfactant concentrations. It is noticed that the ExRF of SAG decreased with a concentration of 1wt% before 0.25-0.30 PV injected. However, after this range, The ExRF reached values closer to the base scenario.



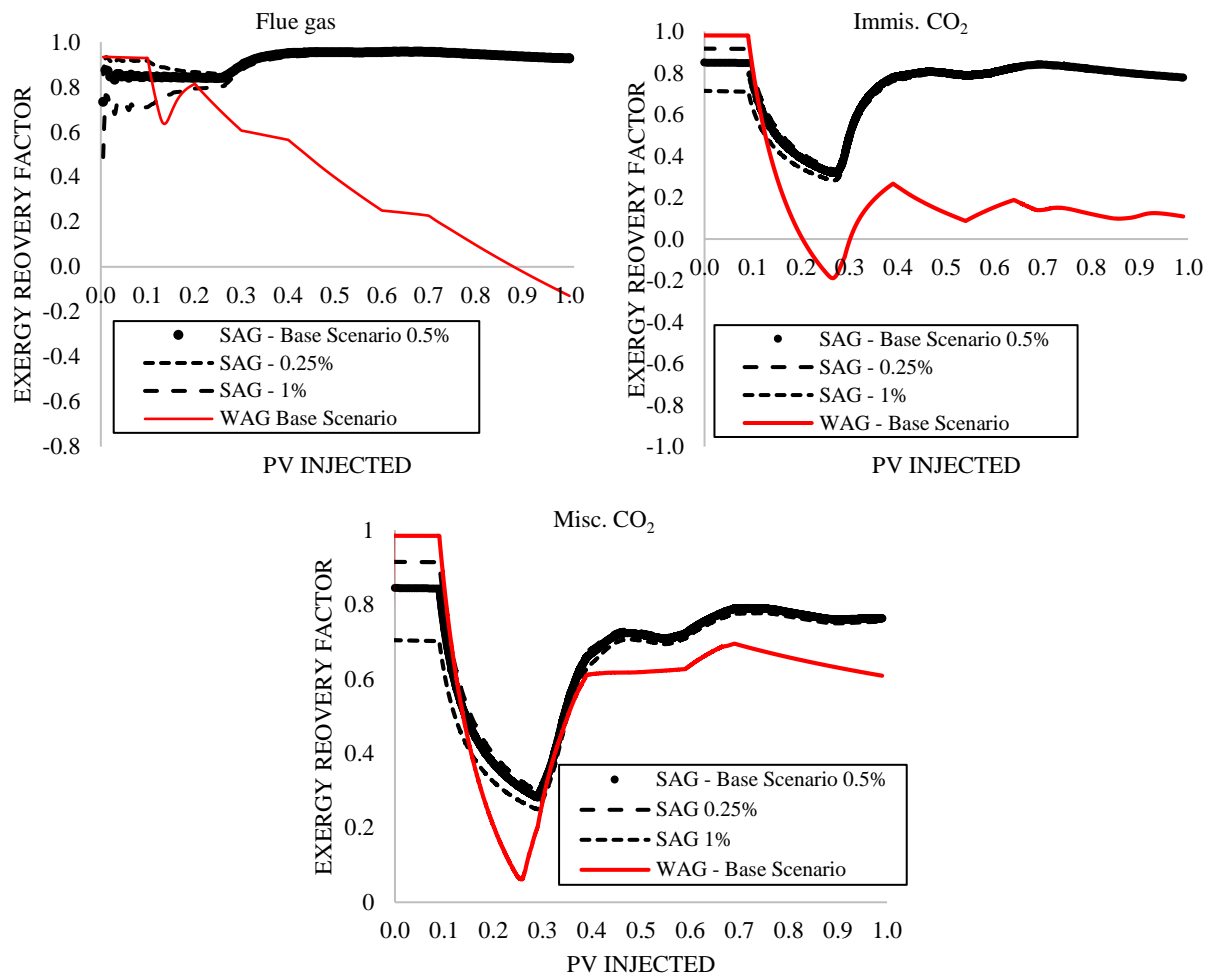


Figure 6-15. Scenario 5- SAG ExRF at surfactant concentration of 0.5%, 2% and 5%

6.4 Comparison of Performance Between N₂, CH₄, Flue gas and CO₂

The behavior of the ExRF WAG varied significantly with regard of the gas injected and the modifications to the system. For this reason, an exergy analysis is also helpful to compare between the same processes. The highest ExRF of WAG, for each gas, is shown in Figure 6-16. The best performance is with miscible CO₂. This is because the highest oil and gas recovery was achieved with miscible CO₂ despite the high cost of capture and separation.

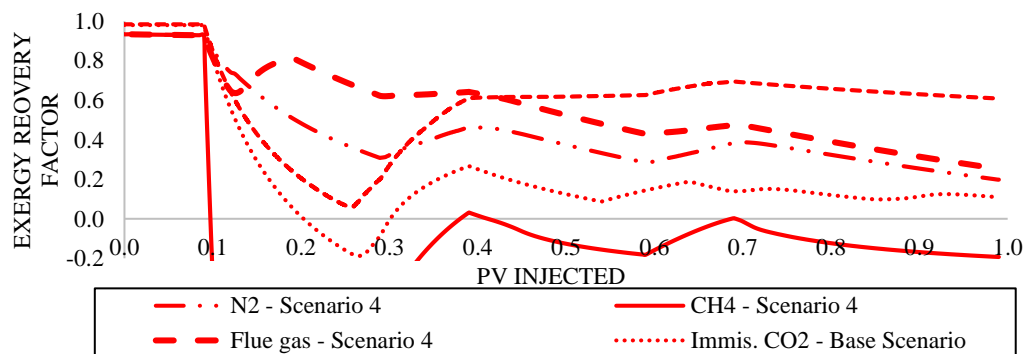


Figure 6-16. Best scenario for WAG, according to the highest ExRF

For SAG, the highest ExRF is with the base scenario of N₂, as seen in Figure 6-17. Despite the high oil recovery of both immiscible and miscible CO₂, the high exergy cost of capture, separation and surfactant combined make them the process with the less ExRF. However, since all cases reached an ExRF higher than 0.7 at the end of the injection, all options seem to be feasible.

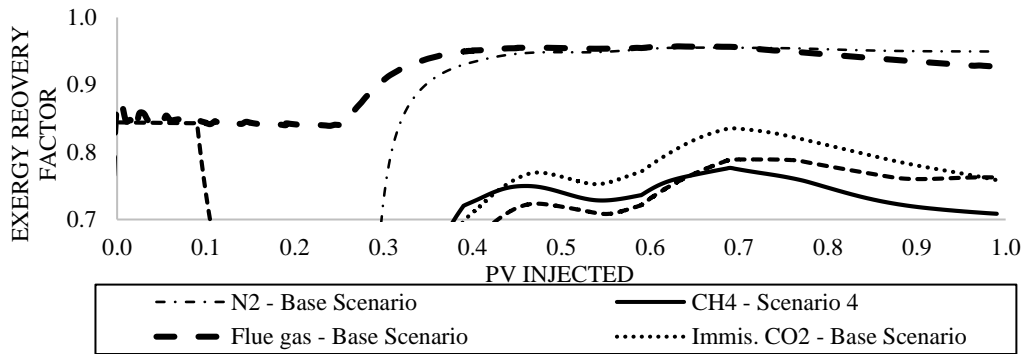


Figure 6-17. Best scenario for SAG, according to the highest ExRF

6.5 CO₂ Emissions to the Atmosphere

The exergy analysis is also useful to assess a process with respect to CO₂ emissions to the atmosphere and measure the impact to the environment. In the upstream oil and gas sector, the energy is traditionally obtained by the combustion of diesel or natural gas in power generators in situ [73]. Diesel produces approximately 74.1 kg of CO₂ per GJ generated and natural gas produces about 56.1 kg of CO₂ per GJ generated [74]. It is assumed that the energy is produced by in situ diesel power generators. On the other hand, it is assumed that the energy required for the CO₂ capture and transport comes from the gas power plant where it is produced. Additionally, the energy required to manufacture the surfactant that comes from fossil fuels is 19.92 GJ/ton of surfactant and it is divided in 43% from natural gas, 34% from oil and 23% from coal [70].

The total emissions of SAG and WAG are not too different as seen in Figure 6-18. Even though for SAG, the emissions for the manufacturing and transport of the surfactant are added, there is more exergy invested in separation and recompression in WAG. This is because there was more production of injection gases due to an earlier breakthrough.

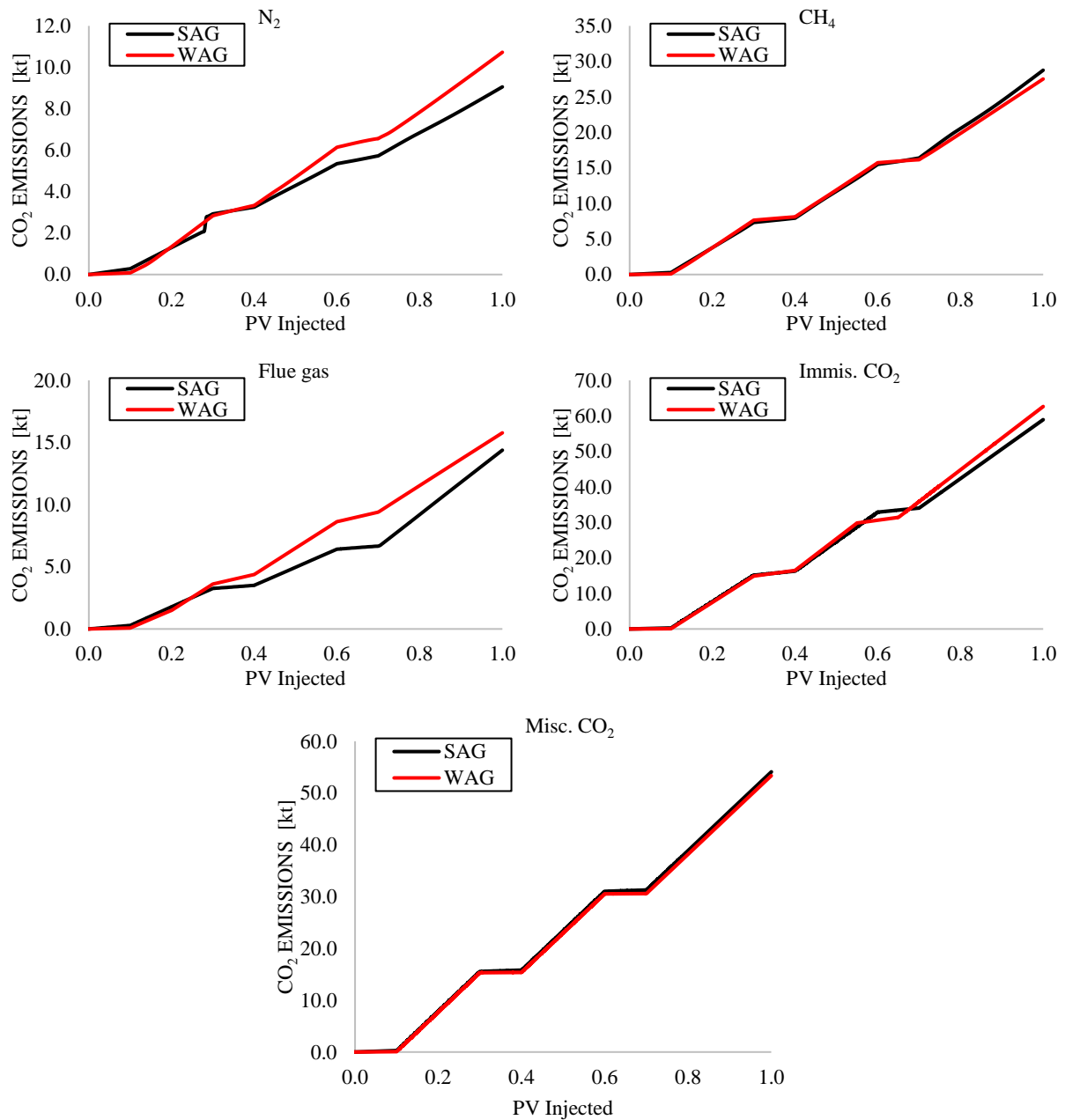


Figure 6-18. Cumulative CO₂ emissions of WAG and SAG

Finally, the CO₂ emissions can also be measured with respect to the incremental oil generated (kg CO₂/bbl), in order to assess efficiency. In Figure 6-19, it is shown that with SAG, less CO₂ is emitted per incremental barrel of oil extracted. This means that SAG can be considered a more efficient method than WAG and less harmful to the environment. On the other hand, although SAG and WAG with CO₂ got a positive ExRF at the end of the injection and high oil recovery, the emissions are between 135 CO₂/bbl and 710 CO₂/bbl, more than twice than any of the other SAG cases.

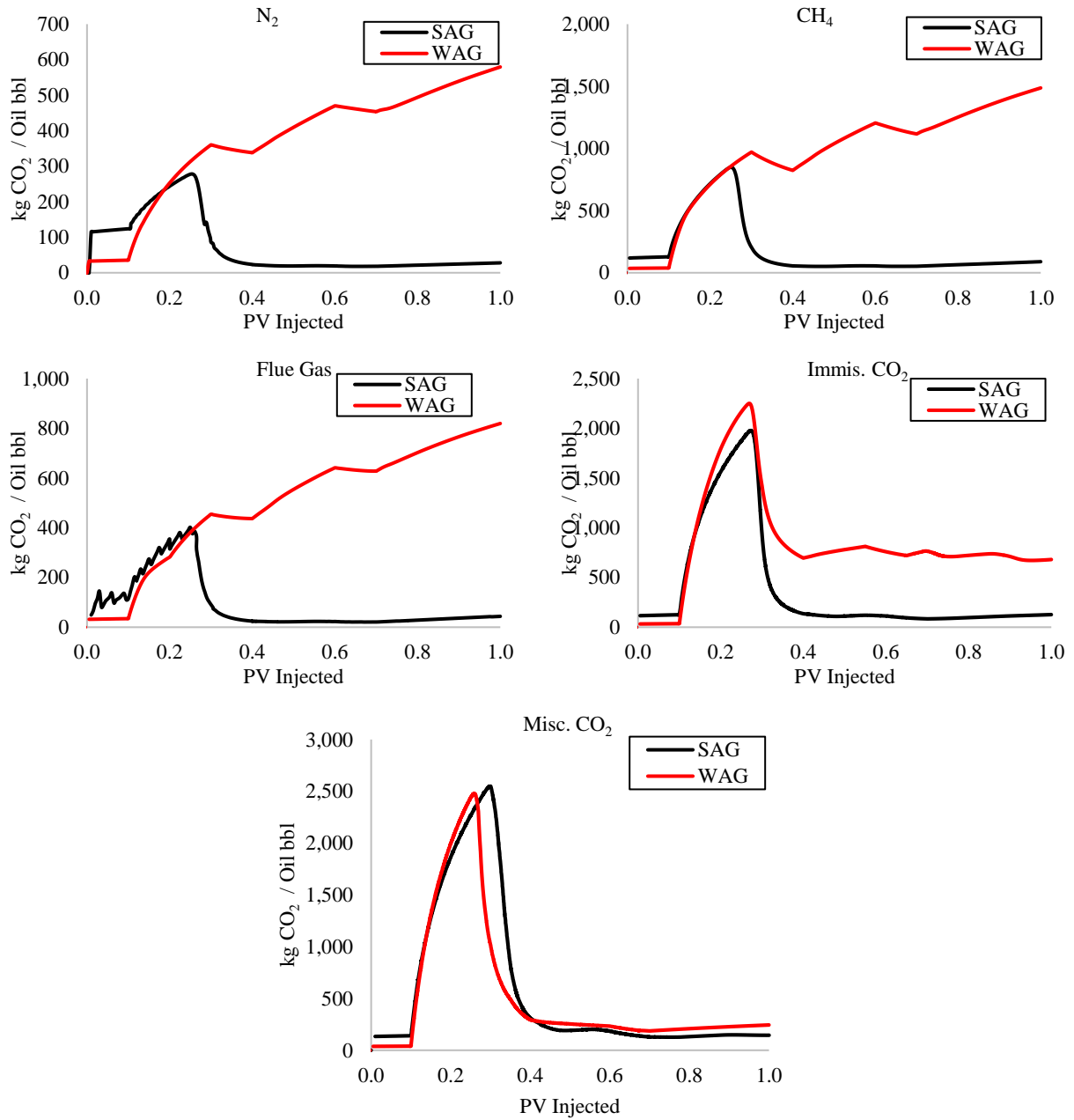


Figure 6-19. CO₂ emissions per barrel of incremental oil [kgCO₂/bbl]

7 Conclusions and Recommendations

7.1 Surfactant Screening for Steam Foam Applications

The solubility, thermal stability, static adsorption, dynamic adsorption, and foam behavior in porous media, of six anionic surfactants were evaluated to determine the best candidate to generate foam in steam EOR processes. A summary of these experiments and conclusions are provided below.

Solubility

- The solubility of the surfactants in brine, at room temperature, was good for surfactant E and F, regular for Surfactant A, C and D; and poor for Surfactant B.
- The solubility of Surfactant B was enhanced by heating the solution to 90°C for 24 hours.

Thermal Stability

- Surfactant B had the best thermal stability. It is a linear toluene sulfonate. It has three key characteristics associated with high thermal stability: 1) a sulfonate head, 2) an aromatic group in the sulfonate head (toluene) and, 3) a long linear tail (18 carbons).
- Surfactant E and F had regular thermal stability. These surfactants have a sulfonated head, an aromatic group in the sulfonate head, but they might not have a long tail.
- Surfactant A had a regular thermal stability at 250°C but a poor thermal stability at 275°C. This surfactant has a sulfonate head, a long tail but it does not have an aromatic ring in the sulfonate head.
- Surfactant C and D had a poor thermal stability. These surfactants do not have any of the three characteristics previously mentioned.
- The pH of the surfactant solutions was between 6.6 and 7. After maturation the pH dropped between 5.6 and 6.6. It was assumed that if the surfactants were stable at this pH, they would be more stable at higher pH values.

Foamability

- The ability of Surfactant B, C, E and F to generate foam in a Bentheimer sandstone core was evaluated at 60°C, 120°C and 180°C. Surfactant E and F had the strongest foam at

60°C and 120°C, with the highest max. μ_{app} . Variation with temperature was as expected with the MRF curves collapsing together.

- Surfactant B had lower μ_{app} at lower temperatures, but behavior changed less with temperature, so this surfactant had a stronger foam than Surfactant E and F at 180°C.
- Surfactant C had the weakest foam at all temperatures. However, it was unusual that it showed increasingly max. μ_{app} and fg^* with increasing temperature.

Adsorption

- Static adsorption was tested for Surfactant B, C, E and F at 24°C, 60°C and 90°C. These are not considered high temperatures. It was found possible to determine that adsorption in reservoir rock decreased with temperature.
- Dynamic adsorption was tested for Surfactant B (the surfactant of interest) at 120°C in Bentheimer sandstone. The surfactant adsorbed was 0.059 mg/g rock. However, demi water was used instead of brine to prevent the core from being blocked. It is expected that at higher salinities a higher adsorption would occur.

CMC

- The CMC of Surfactant B was found to be between 2.86 ppm and 6.04 ppm at room temperature.
- At concentrations below the CMC, it took a long time for the surface tension measurement to reach a stable value for up to 4 hours.

7.1.1 Recommendations for Future Research – Surfactant Screening

- A new brine recipe, with a lower divalent cation concentration, should be chosen to avoid precipitation of surfactants. However, a realistic one is recommended to be as close as possible to field conditions.
- For thermal stability, it is helpful to check the chemical classification of the surfactant, information that should be available in the material safety data sheet of the surfactant. If it has a sulfonate group in the head, an aromatic group attached to the head, and a long tail (more than 18 carbons) it is likely to be stable above 250°C. Otherwise, if it lacks one of these characteristics, it is more likely not to be stable above 250°C.

7.2 Exergy Analysis of SAG and WAG

An exergy analysis was performed to assess and compare the feasibility of WAG and SAG with N₂, CH₄, flue gas and CO₂. The system considered the capture of the gas, the initial compression of the gas at the capture site in order to be transported to the oil field, compression of the gas into the reservoir, water injection, separation of the gas stream, recompression of the gas recirculated stream and water treatment. The oil and gas production were calculated using a 2-D, 3-phase compositional model that includes the transport of surfactant and foam. From this study, the following conclusions were made:

- Using classic thermodynamic concepts, it is possible to assess the technical viability of any EOR method. In this case, WAG vs. SAG.
- The exergy recovery factor (ExRF), measured the net useful energy with respect to the initial energy associated to the hydrocarbon fuels extracted. A negative ExRF indicates that more input energy is required than extracted.
- For any gas, SAG had an initial lower ExRF than WAG. However, once the foam was generated and reduced the gas mobility, the oil and gas production were boosted. This increment in production caused the ExRF of SAG to raise higher than the ExRF of WAG.
- The incremental oil recovery of WAG was low for N₂, CH₄ and flue gas due to gravity segregation and higher for immiscible and miscible CO₂ was due to a better sweep of the reservoir.
- The best scenario for each gas, with the highest ExRF, were those on which the natural gas stream is used as a product, given that it possesses a chemical exergy of 51.98 MJ/kg.
- The sensitivity of the ExRF of SAG was analyzed by incrementing the surfactant concentration from 0.25wt% to 0.5wt% and 1.0wt% However, these ExRF values were still higher than the ExRF of WAG.
- The exergy analysis was also useful to assess the environmental impact in terms of CO₂ emissions to the atmosphere. Assuming the energy invested came from diesel or natural gas power plants or stations, was possible to determine the amount of CO₂ generated per GJ of exergy required. The total CO₂ generated is not that different between SAG and WAG.

- However, by measuring the CO₂ generated per incremental barrel of oil, SAG was more efficient than WAG. Extraction of 1 barrel of oil produced between 259 kg and 1028 kg of CO₂ with WAG. In contrast, with SAG the value was between 36 kg and 157 kg.

7.2.1 Recommendations for Future Research – Exergy Analysis

- An exergy analysis can be done on any EOR process. Therefore, it is recommended to analyze the ExRF of steam injection and steam foam applications that would include a calculation of the exergy to produce steam at the desired quality.
- Different scenarios on which reservoir properties vary can be also tested. This is with the aim to test foams with adverse reservoir conditions.
- Capital expenses can be included in the system, by assigning an exergy cost to infrastructure such as the pipeline between the power plant and the oil field, drilling equipment, completion equipment, etc.
- Finally, integrating an exergy analysis to any project in development in order to assess the impact to the environment.

References

- [1] United Nations, Department of Economic and Social Affairs, Population Division (2017). *World Population Prospects: The 2017 Revision, Volume II: Demographic Profiles (ST/ESA/SER.A/400)*.
- [2] International Energy Agency, “Chapter 1: Introduction and scope,” *World Energy Outlook 2017*, pp. 33–61, 2017.
- [3] R. G. Miller and S. R. Sorrell, H. Lane, “The future of oil supply” *Philos. Trans. R. Soc. A*, vol. 372, 20130179, 2014.
- [4] M. M. Almajid, “Microvisual Observation of Foam Generation and Coalescence using Micromodels in the Presence and Absence of Oil,” Doctoral dissertation, Sanford University, 2015.
- [5] G. Lake, L.W., Johns, R.T., Rossen, W.R. and Pope, *Fundamentals of enhanced oil recovery*. Society of Petroleum Engineers, 2014.
- [6] P. L. Bondor, “Applications of carbon dioxide in enhanced oil recovery,” *Energy Convers. Manag.*, vol. 33, pp. 579–586, 1992.
- [7] G. Zhang, and R. Seright, “Hydrodynamic Retention and Rheology of EOR Polymers in Porous Media,” *SPE*, no. April, pp. 13–15, 2015.
- [8] J. P. Kohar and S. Gogoi, “Radial Drilling Technique For Improving Recovery From Existing Oil Fields,” *Int. J. Sci. Technol. Res. Vol. 3*, pp. 159–161, 2014.
- [9] P. Chen, A. Sowaidi, H. Patel, K. Brantferger, K. A. B. Buang, F. I. Syed, and R. Al Shehhi “Assessment of Simultaneous Water and Gas Injection SWAG Pilot in a Giant Offshore Carbonate Reservoir,” *Abu Dhabi Int. Pet. Exhib. Conf.*, pp. 1–10, 2016.
- [10] R. J. Farn, *Chemistry and Technology of Surfactants*. Blackwell Publishing. 2007.
- [11] V. J. Van Der Bent, “Comparative study of foam stability in bulk and porous media,” Delft University of Technology, 2014.
- [12] A. Bhakta and E. Ruckenstein, “Drainage and coalescence in standing foams,” *J. Colloid Interface Sci.*, vol. 191, pp. 184–201, 1997.
- [13] J. J. Sheng, “Foams and Their Applications in Enhancing Oil Recovery,” in *Enhanced Oil Recovery Field Case Studies*, Gulf Professional Publishing. 2013, pp. 251–280.
- [14] J. R. Kanicky, S. Pandey, and D. O. Shah, “Surface Chemistry in the Petroleum Industry,” *Handb. Appl. Surf. Colloid Chem.*, pp. 252–267, 2002.
- [15] L. L. Schramm, *Emulsions, Foams, and Suspensions*. WILEY-VCH Verlag GmbH &

- Co. KGaA. 1995.
- [16] L. L. Schramm, “Surfactants: Fundamentals and Applications in the Petroleum Industry,” Cambridge University Press, 2000.
- [17] F. E. Suffridge, K. T. Raterman, and G. C. Russell, “Foam Performance Under Reservoir Conditions,” *SPE Annual Technical Conference and Exhibition*. Society of Petroleum Engineers, San Antonio, Texas, 1989.
- [18] D. Cohen, T. W. Patzek, and C. J. Radke, “Onset of Mobilization and the Fraction of Trapped Foam in Porous Media,” *Transp. Porous Media*, vol. 28, pp. 253–284, 1997.
- [19] T. C. Ransohoff and C. J. Radke, “Mechanisms of Foam Generation in Glass-Bead Packs,” *SPE Reserv. Eng.*, vol. 3, pp. 573–585, 1988.
- [20] A. R. Kovscek, T. W. Patzek, and C. J. Radke, “Mechanistic Prediction of Foam Displacement in Multidimensions: A Population Balance Approach,” *SPE/DOE Improv. Oil Recover. Symp.*, 1994.
- [21] G. J. Hirasaki and J. B. Lawson, “Mechanisms of Foam Flow in Porous Media: Apparent Viscosity in Smooth Capillaries,” *Soc. Pet. Eng. J.*, vol. 25, pp. 176–190, 1985.
- [22] E. Delamaide and A. Cuenca, “State of the Art Review of the Steam Foam Process,” *Soc. Pet. Eng.*, SPE-181160, pp. 19–20, 2016.
- [23] S. A. Jones, G. Laskaris, S. Vincent-Bonnieu, R. Farajzadeh, and W. R. Rossen, “Effect of surfactant concentration on foam: From coreflood experiments to implicit-texture foam-model parameters,” *J. Ind. Eng. Chem.*, vol. 37, pp. 268–276, 2016.
- [24] J. M. Alvarez, H. J. Rivas, and W. R. Rossen, “Unified Model for Steady-State Foam Behavior at High and Low Foam Qualities,” *SPE J.*, vol. 6, pp. 325–333, 2001.
- [25] M. T. Vafaei, R. Eslamloueyan, L. Enfeali, and S. Ayatollahi, “Analysis and simulation of steam distillation mechanism during the steam injection process,” *Energy and Fuels*, vol. 23, pp. 327–333, 2009.
- [26] D. Cuthiell, G. Kissel, C. Jackson, T. Frauenfeld, D. Fisher, and K. Rispler, “Viscous fingering effects in solvent displacement of heavy oil,” *J. Can. Pet. Technol.*, vol. 45, no. 7, pp. 29–38, 2006.
- [27] A. H. Falls, J. B. Lawson, and G. J. Hirasaki, “The Role of Noncondensable Gas in Steam Foams,” *J. Pet. Technol.*, vol. 40, pp. 95–104, 1988.
- [28] L. Co, Z. Zhang, Q. Ma, G. Watts, L. Zhao, P. J. Shuler, Y. Tang, “Evaluation of functionalized polymeric surfactants for EOR applications in the Illinois Basin” *J. Pet. Sci. Eng.*, vol. 134, pp. 167–175, 2015.
- [29] Swagelok Energy Advisors, Inc., “Steam Quality-Plant Operations Require a High

- Steam Quality,” no. 23, pp. 2–3, 2009.[Online]. Available: www.swagelokenergy.com
- [30] C. H. Mora and S. J. de Oliviera, “Environmental exergy analysis of wastewater treatment plants,” *Tecnologia/Technology*, vol. 5, no. December, pp. 24–29, 2006.
- [31] Rgy, “Exergy analysis book chapter,” [Online]. Available: http://www.iitg.ac.in/scifac/qip/public_html/cd_cell/chapters/p_mahanta_adv_engg_thermo/Chapter-3.pdf
- [32] J.P. Buroudier, "Thermodynamics" Elsevier Science, 2016. <https://www-sciencedirect-com.tudelft.idm.oclc.org/book/9781785481765/thermodynamics>. Accessed 2018.
- [33] G. Tsatsaronis, “Definitions and nomenclature in exergy analysis and exergoeconomics,” *Energy*, vol. 32, pp. 249–253, 2007.
- [34] M. Tabatabaian and R. K. Rajput, *Advanced Thermodynamics*. Bloomfield. Mercury Learning & Information, 2017.
- [35] I. Glassman, R. A. Yetter, and N. G. Glumac, *Chemical thermodynamics and flame temperatures in Combustion*. Academic Press. 2014.
- [36] M. Voldsund, I. S. Ertesvåg, W. He, and S. Kjelstrup, “Exergy analysis of the oil and gas processing on a north sea oil platform a real production day,” *Energy*, vol. 55, pp. 716–727, 2013.
- [37] Shell Chemicals, “ENORDET: DETERGENTS FOR ENHANCED OIL RECOVERY Producing more from your current operations.”[Online]. Available: <https://www.shell.com/business-customers/chemicals/our-products/higher-olefins-and-derivatives/enordet-surfactants.html>.
- [38] L. Chiappisi, “Polyoxyethylene alkyl ether carboxylic acids: An overview of a neglected class of surfactants with multiresponsive properties,” *Adv. Colloid Interface Sci.*, vol. 250, pp. 79–94, 2017.
- [39] E. I. Franses, L. E. Scriven, W. G. Miller, and H. T. Davis, “Interpreting the appearance of dispersed systems: II. A guide for surfactant systems,” *J. Am. Oil Chem. Soc.*, vol. 60, pp. 1043–1049, 1983.
- [40] Kibron, “Tensiometer for the analytical laboratory”. [Online]. Available: <http://www.kibron.com/products/tensiometers/ez-pi-plus>
- [41] S. Shah, J. Gong, A. Hussain, and M. Slob, “Foam-Flooding Experiment Instructions,” Internal CiTG document. 2017.
- [42] A. E. Peksa, K. H. A. A. Wolf, and P. L. J. Zitha, “Bentheimer sandstone revisited for experimental purposes,” *Mar. Pet. Geol.*, vol. 67, pp. 701–719, 2015.
- [43] L. Kapetas, S. V. Bonnieu, S. Danelis, W.R. Rossen, R. Farajzadeh, A.A. Eftekhari, S.

- R. Mohd Shafian, R. Z. Kamarul Bahrim, "Effect of permeability on foam-model parameters: An integrated approach from core-flood experiments through to foam diversion calculations," *Colloids Surfaces A Physicochem. Eng. Asp.*, vol. 530, pp. 172–180, 2017.
- [44] S. A. Jones, Personal communication, Diameter of a Bentheimer Lilliput core." 2018.
- [45] G. Laskaris, "Effect of Surfactant Concentration, Water Treatment Chemicals, Fatty Acids and Alcohols on Foam Behavior in Porous Media and in Bulk," Delft University of Technology, 2015.
- [46] X. Wei, X. Wang, J. L., D. S., B. Y., X. W., "Adsorption kinetics of 3-alkoxy-2-hydroxypropyl trimethyl ammonium chloride at oil–water interface". *Applied Surface Science*. vol. 261. pp. 1-916, 2012.
- [47] C. Negin, S. Ali, and Q. Xie, "Most common surfactants employed in chemical enhanced oil recovery," *Petroleum*, vol. 3, pp. 197–211, 2017.
- [48] P. S. Abbott, *Surfactant Science : Principles and Practice*. Creative Common. 2015.
- [49] K. Tsujii, N. Saito, and T. Takeuchi, "Krafft points of anionic surfactants and their mixtures with special attention to their applicability in hard water," *J. Phys. Chem.*, vol. 84, pp. 2287–2291, 1980.
- [50] M. J. Scott and M. N. Jones, "The biodegradation of surfactants in the environment," *Biochim. Biophys. Acta - Biomembr.*, vol. 1508, pp. 235–251, 2000.
- [51] M. I. Nieto Jimenez, "Transformaciones De La Superficie Del Vidrio," *Bol.Soc.Esp.Ceram.Vidr*, vol. 26, pp. 83–92, 1987.
- [52] Senturk U., Vamer J.R., LaCourse W. C. "Structure-hardness relation for high-temperature S02-dealkalized float glass" *Journal of Non-Crystalline Solids*. vol. 222. pp. 160-166. 1997
- [53] H. M. Muijs, P. P. M. and R. J., "Surfactants for Mobility Control in High-Temperature Steam-Foam Applications," *SPE*, SPE-17361-MS, 1988.
- [54] R. D. Stoll, H. W. Gudenau, M. W. Lupik, and J. L. Smith, "Mobility Control for Steamflooding With High-Temperature-Resistant Additives," *SPE Reserv. Eng.*, vol. 8, pp. 281–284, 1993.
- [55] S. A. Jones, Personal communication, Surfactant F and E thermal stability results by Manufacturer." 2018.
- [56] L. Kapetas *et al.*, "Effect of temperature on foam flow in porous media," *J. Ind. Eng. Chem.*, vol. 36, no. April, pp. 229–237, 2016.
- [57] S. Samanta and P. Ghosh, "Coalescence of bubbles and stability of foams in aqueous

- solutions of Tween surfactants,” *Chem. Eng. Res. Des.*, vol. 89, pp. 2344–2355, 2011.
- [58] M. R. Azam, I. M. Tan, L. Ismail, M. Mushtaq, M. Nadeem, and M. Sagir, “Static adsorption of anionic surfactant onto crushed Berea sandstone,” *J. Pet. Explor. Prod. Technol.*, vol. 3, pp. 195–201, 2013.
- [59] M. S. Santos, F. W. Tavares, and E. C. Biscaia, “Molecular thermodynamics of micellization: Micelle size distributions and geometry transitions,” *Brazilian J. Chem. Eng.*, vol. 33, pp. 515–523, 2016.
- [60] Y. P. Zhu, M. J. Rosen, S. W. Morrall, and J. Tolls, “Surface properties of linear alkyl benzene sulfonates in hard river water,” *J. Surfactants Deterg.*, vol. 1, pp. 187–193, 1998.
- [61] J. P. Tranier, R. Dubettier, A. Darde, and N. Perrin, “Air Separation, flue gas compression and purification units for oxy-coal combustion systems,” *Energy Procedia*, vol. 4, pp. 966–971, 2011.
- [62] R. Farajzadeh, A. A. Eftekhari, G. Dafnomilis, L. W. Lake, and J. Bruining, “On the Sustainability of CO₂ Storage through CO₂ Enhanced Oil Recovery”. Manuscript in preparation. 2017.
- [63] L. V. van der Ham and S. Kjelstrup, “Exergy analysis of two cryogenic air separation processes,” *Energy*, vol. 35, pp. 4731–4739, 2010.
- [64] D. W. Olivera de Medeiros, “DWSIM - Open Source Process Simulation, Modeling and Optimization.” 2018.[Online]. Available: <http://dwsim.inforside.com.br>
- [65] J. R. Couper, W. R. Penney, J. R. Fair, and S. M. Walas, “Fluid Transport Equipment,” *Chem. Process Equip.*, pp. 121–160, 2012.
- [66] IEAGHG Supported by Global CCS Institute, “CO₂ Pipeline Infrastructure - Report: 2013/18,” 2013.
- [67] Pre Technologies Ltd., “Simulation-based analysis for gravity separators,” 2018. [Online]. Available: <http://www.pretechnologies.com/experience/gravity-separation-white-paper>.
- [68] E.T. Igunnu and G.Z. Chen. "Produced water treatment technologies". *Int. J. Low Carbon Technol.*, vol. 9., pp. 157-177, 2014.
- [69] J. Drewes, Je., Cath, Ty., Xu, P., Graydon, “An integrated framework for treatment and management of produced water,” *Tech. Assess. Prod. Water Treat. Technol.*, RPSEA Project, 07122-2, 2009.
- [70] M. K. Patel, “Surfactant production and use in Germany: resource requirements and CO₂ emissions,” *Closing Carbon Cycles*, Doctoral dissertation, 1998.

- [71] F. Baldi, H. Johnson, C. Gabriellini, and K. Andersson, "Energy and exergy analysis of ship energy systems - The case study of a chemical tanker," *Int. J. Thermodyn.*, vol. 18, pp. 82–93, 2015.
- [72] G. J. H. Yongchao Zeng, Rouhi Farajzadeh, Sibani L. Biswal, "A 2-D Simulation Study on CO₂ Soluble Surfactant for Foam Enhanced Oil Recovery," Manuscript in preparation. 2018.
- [73] T. Van Nguyen, L. Pierobon, B. Elmegaard, F. Haglind, P. Breuhaus, and M. Voldsund, "Exergetic assessment of energy systems on North Sea oil and gas platforms," *Energy*, vol. 62, pp. 23–36, 2013.
- [74] Engineering ToolBox, "Combustion of Fuels - Carbon Dioxide Emission," 2009. [Online]. Available: https://www.engineeringtoolbox.com/co2-emission-fuels-d_1085.html. [Accessed: 04-Oct-2018].